Powder-mixed Electric Discharge Machining (PMEDM) of Inconel 625

Gangadharudu Talla

Department of Mechanical Engineering
National Institute of Technology Rourkela

Powder-mixed Electric Discharge Machining (PMEDM) of Inconel 625

Dissertation submitted to the

National Institute of Technology Rourkela

in partial fulfilment of the requirements

of the degree of

Doctor of Philosophy

in

Mechanical Engineering

by

Gangadharudu Talla

(Roll number: 512ME128)

under the supervision of

Prof. S. Gangopadhyay

and

Prof. C. K. Biswas

August, 2016

Department of Mechanical Engineering

National Institute of Technology Rourkela

Certificate of Examination

Roll Number: <u>512ME128</u>

Name: <u>Gangadharudu Talla</u>

Title of Dissertation: <u>Powder-mixed Electric Discharge Machining (PMEDM) of Inconel 625</u>

We the below signed, after checking the dissertation mentioned above and the official record book (s) of the student, hereby state our approval of the dissertation submitted in partial fulfillment of the requirements of the degree of Doctor of Philosophy in Mechanical Engineering at National Institute of Technology Rourkela. We are satisfied with the volume, quality, correctness, and originality of the work.

C. K. Biswas
Co-Supervisor

S. Gangopadhyay
Principal Supervisor

S. K. Sahoo
Member (DSC)

S. Datta
Member (DSC)

M. K. Mishra
Member (DSC)

G. L. Datta
Examiner

K. P. Maity
Chairman (DSC)

Mechanical Engineering
National Institute of Technology Rourkela

August 29, 2016

Supervisors' Certificate

This is to certify that the work presented in this dissertation entitled "*Powder-mixed Electric Discharge Machining (PMEDM) of Inconel 625*" by "*Gangadharudu Talla*", Roll Number 512ME128, is a record of original research carried out by him under our supervision and guidance in partial fulfillment of the requirements of the degree of *Doctor of Philosophy* in *Mechanical Engineering*. Neither this dissertation nor any part of it has been submitted for any degree or diploma to any institute or university in India or abroad.

C. K. Biswas
Co-Supervisor

S. Gangopadhyay
Principal Supervisor

Dedicated to my parents, wife and teachers

Declaration of Originality

I, Gangadharudu Talla, Roll Number 512ME128 hereby declare that this dissertation entitled "Powder-mixed Electric Discharge Machining (PMEDM) of Inconel 625" represents my original work carried out as a doctoral student of NIT Rourkela and, to the best of my knowledge, it contains no material previously published or written by another person, nor any material presented for the award of any other degree or diploma of NIT Rourkela or any other institution. Any contribution made to this research by others, with whom I have worked at NIT Rourkela or elsewhere, is explicitly acknowledged in the dissertation. Works of other authors cited in this dissertation have been duly acknowledged under the section "References". I have also submitted my original research records to the scrutiny committee for evaluation of my dissertation.

I am fully aware that in case of any non-compliance detected in future, the Senate of NIT Rourkela may withdraw the degree awarded to me on the basis of the present dissertation.

August 29, 2016   *Gangadharudu Talla*
NIT Rourkela

Acknowledgement

August 29, 2016   *Gangadharudu Talla*
NIT Rourkela   Roll Number: 512ME128

Abstract

In recent times, nickel-based super alloys are widely used in aerospace, chemical and marine industries owing to their supreme ability to retain the mechanical properties at elevated temperature in combination with remarkable resistance to corrosion. Some of the properties of these alloys such as low thermal conductivity, strain hardening tendency, chemical affinity and presence of hard and abrasives phases in the microstructure render these materials very difficult-to-cut using conventional machining processes.

Therefore, the aim of the current research is set to improve the productivity and surface integrity of machined surface of Inconel 625 (a nickel-based super alloy) by impregnating powder particles such as graphite, aluminum and silicon to kerosene dielectric during electric discharge machining (EDM). Initially, temperature distribution, material removal rate (MRR) and residual stress were predicted through numerical modelling of powder-mixed EDM (PMEDM) process. In the experimental investigation, particle size analysis of the as-received powder particles was carried out to identify the distribution of particles. X-ray diffraction (XRD) analysis of particles indicated the presence of various phases including small amount of impurities. An experimental setup was developed and integrated with the existing EDM system for carrying out PMEDM process. The experiments were planned and conducted by varying five different parameters such as powder concentration, peak current, pulse-on time, duty cycle and gap voltage according to the central composite deign (CCD) of response surface methodology (RSM). Effects of these parameters along with powder concentration were investigated on various EDM characteristics such as material removal rate (MRR), radial overcut (ROC) and surface integrity aspects including surface crack density (SCD), surface roughness (SR), altered layer thickness (ALT), microhardness of surface and sub-surface regions, chemical and metallurgical alterations of the machined surface and residual stress. Results clearly indicated that addition of powder to dielectric has significantly improved MRR and surface integrity compared to pure dielectric. Among the powders used, graphite has resulted in highest MRR, lowest SCD, least ALT, least microhardness of surface and sub-surface regions. Least ROC, lowest surface roughness and least residual stress were obtained using silicon powder. Aluminum performed well in terms of MRR at low concentration range (upto 6 g/l).Therefore, optimal process performance under a given operating condition depends on judicious selection of powder materials, their size, concentration and process parameters.

Keywords: Powder-mixed EDM; Inconel 625; Numerical modeling; Material removal rate; Radial overcut; Surface Integrity.

Contents

List of Figures

List of Tables

List of Symbols

C_p	powder concentration, g/l
I_p	peak current, A
T_{on}	pulse-on time, μs
T_{off}	pulse-off time, μs
T_{mach}	machining time, s
T_{up}	tool lift time, μs
T_w	working time, μs
τ	duty cycle, %
V_g	gap voltage, V
E_i	initial voltatage for concentration N_i
E_{br}	breakdown voltage for final concentration N_i
σ	Boltzmann constant
ε_1	permittivity of dielectric
ε_p	permittivity of powder particle
α	field enhancement factor for small protrusion
g_d	distance between bottom of the particle and micro-peak
h_p	height of the protrusion
d_1	spark gap without powder suspension
d_2	spark gap during PMEDM
ρ	density, g/cm^3
C	specific heat, J/kg-K
θ	Bragg angle in X-ray diffraction
β	integral breadth of the peak, rad
κ	constant (0.9)
λ	wave length of the X-ray radiation (0.15418 nm)
W_b	weight of workpiece before machining, g
W_a	weight of workpiece after machining, g
t	time, s
R_a	center line average surface roughness, μm

l	sampling length, mm
D_h	diameter of machined hole, mm
D_t	diameter of tool, mm
L	average crystallite size, Å
e	strain
C	specific heat, J/kg-K
T	temperature, K
T_0	initial or room temperature, K
R_w	fraction of heat transferred to workpiece, %
R	radius of crater, μm
h	convective heat transfer coefficient, W/m^2-K
C_v	crater volume, mm^3
d	crater depth, μm

Chapter 1
Introduction

The growing trend to use slim, light and compact mechanical components in automobile, aerospace, medical, missile, and nuclear reactor industries has led to the development of high strength, temperature resistant, and hard materials during last few decades. It is almost impossible to find sufficiently strong and hard tools to machine aforesaid materials at economic cutting speeds [1]. Moreover, machining of complex shapes in these materials with low tolerances and high surface finish by conventional methods is even more troublesome. Hence, there is great demand for new machining technologies to cut these 'difficult-to-machine' materials with ease and precision. Among modern machining processes, electric discharge machining (EDM) has become highly popular in manufacturing industries due to its capability to machine any electrically conductive material into desired shape with required dimensional accuracy irrespective of its mechanical strength.

Joseph Priestley, The English physicist, first noted the erosion of metals by electric sparks in 1770. However, Russian scientists B. R. Lazarenko and N. I. Lazarenko, first introduced controlled machining by electric discharges in 1943. Intermittent arcing in air between tool electrode and workpiece material, connected to a DC electric supply, caused the erosion of material. The process was not very accurate due to overheating of the machining region and may be defined as 'arc machining' rather than 'spark machining' [2]. During 1980s, the efficiency of EDM raised extraordinarily with the introduction of computer numerical control (CNC). Self- regulated and unattended machining from loading the electrodes into the tool changer to a finished smooth cut was possible with CNC control system. Since then, these emergent virtues of EDM have been vigorously sought after by the manufacturing industries producing tremendous economic advantage and creating keen research interest.

1.1 Principle of EDM

Despite the fact that the material removal mechanism of EDM is not absolutely identified and is still contentious, the most widely established principle is the transformation of electrical energy into thermal energy through a sequence of distinct electric discharges. Fig. 1.1 shows a representative diagram of a typical EDM setup. Build-up of suitable voltage across tool and work-piece (cathode and anode respectively) that are submerged in an insulating dielectric, causes cold emission of electrons from the cathode. These liberated electrons accelerate towards the anode and collide with the dielectric fluid, breaking them into electrons and positive ions. A narrow column of ionized dielectric fluid molecules is established connecting the two electrodes. A spark generates due to the avalanche of electrons. This results in a compression shock wave. Very high temperature (8,000 to 12,000 ºC) is developed which induces melting and evaporation of both the electrodes. The molten metal is evacuated by the mechanical blast (of the bubble), leaving tiny cavities on both tool and workpiece.
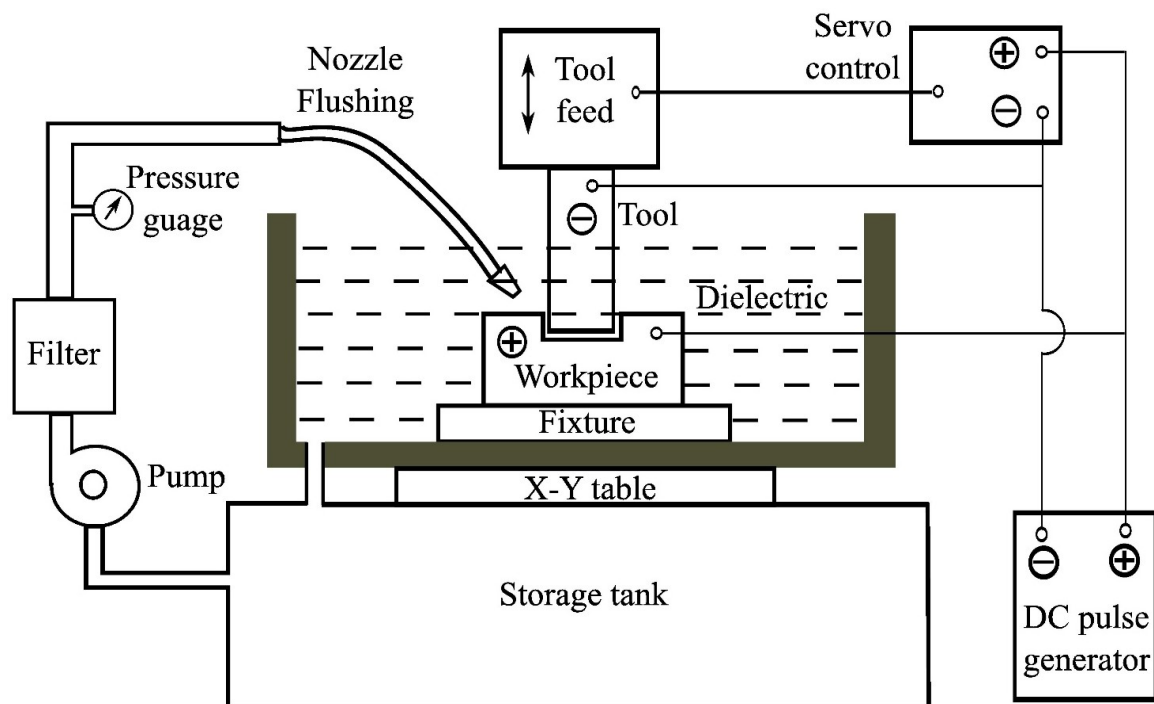
Fig. 1.1 A typical EDM setup

A step by step description of the material removal process due to sparking is presented in Fig. 1.2. There is no direct contact between the two electrodes (held at a small distance) and a high potential is applied between them (Fig. 1.2(b)). The electrode moves towards the workpiece and enhances the electric field in the inter electrode gap, until the breakdown

voltage of dielectric is reached. The spot of discharge is normally between the nearest points of the tool and the workpiece. However, the spot location may change depending on the impurities or debris present in the inter electrode gap. Voltage drops and current flows from workpiece to electrode due to ionization of dielectric and formation of plasma channel (Fig. 1.2(c)). The flow of discharge current continues and there is a constant attack of ions and electrons on the electrodes which ultimately lead to intense heating of the workpiece. The temperature rises between 8,000 °C and 12,000 ºC [3], resulting in the formation of a small molten metal pool at both the electrode surfaces and some of the molten metal directly vaporizes. During this period, plasma channel widens and radius of the molten metal pool increases (Fig. 1.2(d)).
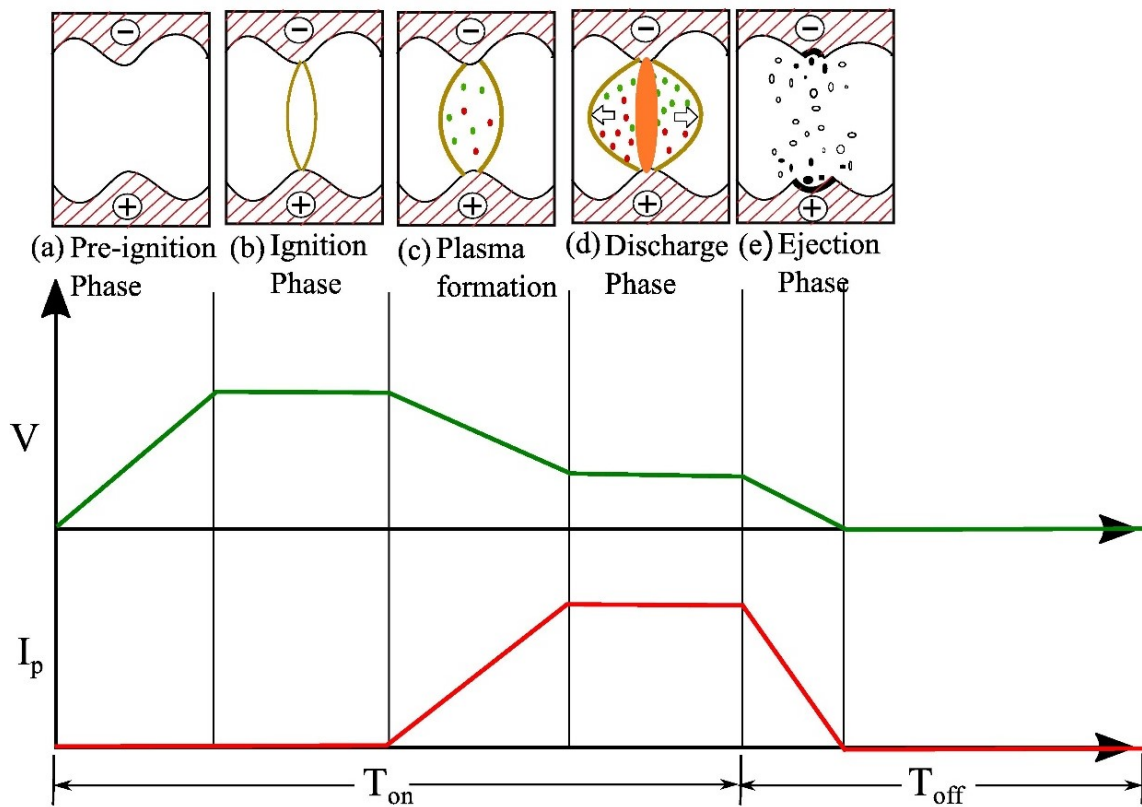
Fig. 1.2 Material removal mechanism in EDM

Towards the end of the discharge, voltage is shut and plasma channel collapses inwards due to the pressure exerted by the neighboring dielectric. As a result, the molten metal pool is powerfully drawn into the dielectric, producing a tiny cavity at the surface of workpiece (Fig. 1.2(e)). The machining process successively removes minute quantities of workpiece material, in the form of molten metal, during discharges. The removed material solidifies to form debris. The flow of dielectric washes away the debris from the discharge zone. The gap increases after material removal at the point of spark, and the position of the next spark

shifts to a different place, where inter electrode gap is the smallest. In this manner, thousands of electric discharges take place at different localities of the workpiece surface corresponding to tool-workpiece gap. As a consequence, a negative replica of the tool surface shape is produced in the workpiece.

1.2 Process variables

As per the discharge phenomena explained earlier, some of the key process parameters which influence the EDM process are,

Discharge current or peak current (I_p): During each pulse-on time, current rises until it attains a certain predetermined level that is termed as discharge current or peak current. It is governed by the surface area of cut. Higher currents produce high MRR, but at the cost of surface finish and tool wear. Accuracy of the machining also depends on peak current, as it directly influences the tool wear.

Discharge voltage (V): Open circuit voltage between the two electrodes builds up before any current starts flowing between them. Once the current flow starts through plasma channel, open circuit voltage drops and stabilizes the electrode gap. A preset voltage determines the working gap between the two electrodes. It is a vital factor that influences the spark energy, which is responsible for the higher MRR, higher tool wear rate and rough surfaces.

Pulse-on time or pulse duration (T_{on}): It is the duration of time (μs), the current is allowed to flow per cycle. Dielectric ionizes and sparking takes place during this period. It is the productive regime of the spark cycle during which current flows and machining is performed. The amount of material removal is directly proportional to the amount of energy applied during this on-time. Though MRR increases with T_{on}, rough surfaces are produced due to high spark energy.

Pulse-off time or pulse interval (T_{off}): It is the duration of time between two consecutive pulse-on times. The supply voltage is cut off during pulse-off time. Dielectric de-ionizes and regains its strength in this period. This time allows the molten material to solidify and to be washed out of the arc gap. Pulse-off time should be minimized as no machining takes place during this period. However, too short T_{off} leads to process instability.

Duty cycle (τ): It is a percentage of the on-time relative to the total cycle time. This parameter is calculated by dividing the on-time by the total cycle time (on-time and off-time), which is shown in Equation 1.1. At higher τ, the spark energy is supplied for longer duration of the pulse period resulting in higher machining efficiency.

$$\tau = \frac{T_{on}}{T_{on} + T_{off}} \times 100 \tag{1.1}$$

Polarity: Polarity refers to the potential of the workpiece with respect to the tool. In straight or positive polarity the workpiece is positive, whereas in reverse polarity workpiece is negative. In straight polarity, quick reaction of electrons produces more energy at anode (workpiece) resulting in significant material removal. However, high tool wear takes place with long pulse durations and positive polarity, due to higher mass of ions. In general, selection of polarity is experimentally determined depending on the combination of workpiece material, tool material, current density and pulse duration.

Dielectric Fluid: Dielectric fluid carries out three important tasks in EDM. The first function of the dielectric fluid is to insulate the inter electrode gap and after breaking down at the appropriate applied voltage, conducting the flow of current. The second function is to flush away the debris from the machined area, and lastly, the dielectric acts as a coolant to assist in heat transfer from the electrodes. Most commonly used dielectric fluids are hydrocarbon compounds, like light transformer oil and kerosene.

Inter electrode gap (IEG): The inter electrode gap is a vital factor for spark stability and proper flushing. The most important requirements for good performance are gap stability and the reaction speed of the system; the presence of backlash is particularly undesirable. The reaction speed must be high in order to respond to short circuits or open gap conditions. Gap width is not measurable directly, but can be inferred from the average gap voltage. The tool servo mechanism is responsible for maintaining working gap at a set value. Mostly electro mechanical (DC or stepper motors) and electro hydraulic systems are used, and are normally designed to respond to average gap voltage.

Tool work time (T_w) and tool lift time (T_{up}): During the working time T_w, multiple sparks occur with a pulse on duration T_{on} and pulse off time T_{off}. Then, the quill lifts up for T_{up} duration when impulse flushing is done. The impulse flushing is an intermittent flushing through side jet and is done through a solenoid valve is synchronized with the lifting of tool. The dielectric is directed towards the IEG to accomplish removal of the debris. The sparking cycle consists of T_w and T_{up} which are shown in Fig. 1.3.
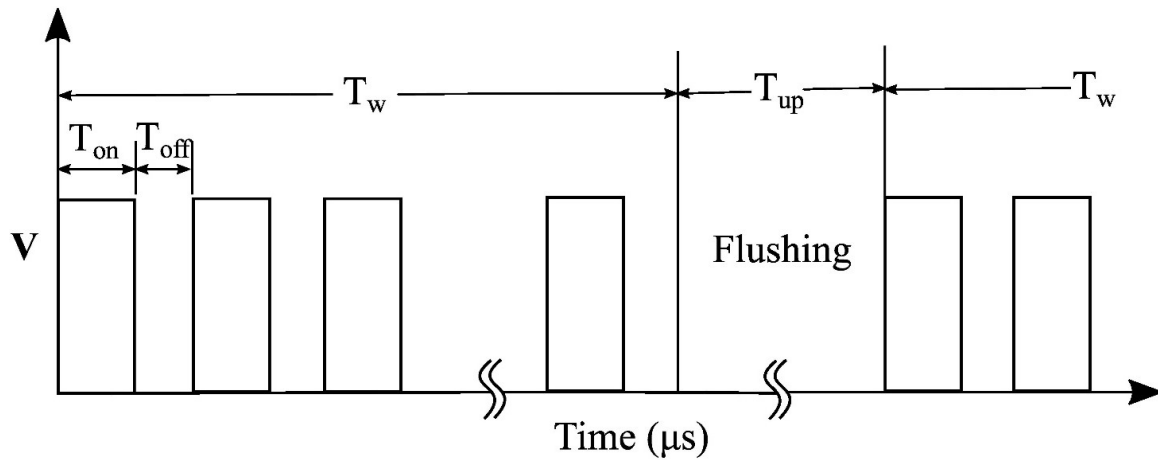
Fig. 1.3 EDM sparking cycle

Flushing Pressure and Type of flushing: Flushing is an important factor in EDM because debris must be removed for efficient cutting. Moreover, it brings fresh dielectric into the inter electrode gap. Flushing is difficult if the cavity is deeper and inefficient flushing may initiate arcing that may create unwanted cavities which are detrimental for surface quality and dimensional accuracy. There are several methods generally adopted to flush the EDM gap: jet or side flushing, pressure flushing, vacuum flushing and pulse flushing. In jet flushing, hoses or fixtures are used and directed at the inter electrode gap to wash away the debris. In pressure and vacuum flushing, dielectric flows through the drilled holes in the electrode, workpiece or fixtures. In pulse flushing, the movement of electrode in up and down, orbital or rotary motion creates a pumping action to draw the fresh dielectric. The usual range of pressure used is between 0.1 and 0.4 kgf/cm^2.

1.3 Performance measures in EDM

Material removal rate (MRR) determines the productivity of any machining process. It can be defined as the volume of the material removed in a unit time. MRR achieved during EDM is quite low (0.1 to 10 mm^3/min-A). Actual value of MRR depends on the machining conditions employed. Overcut determines the accuracy of EDM process. It is the difference between the size of the electrode and the size of the cavity created during machining. Overcut has to be minimized to achieve close tolerances on the machined components. Since the material removal in EDM is achieved through the formation of craters due to the sparks, it is obvious that larger crater size results in a rough surface. So, the crater size, which depends mainly on the energy per spark, controls the quality of the surface.
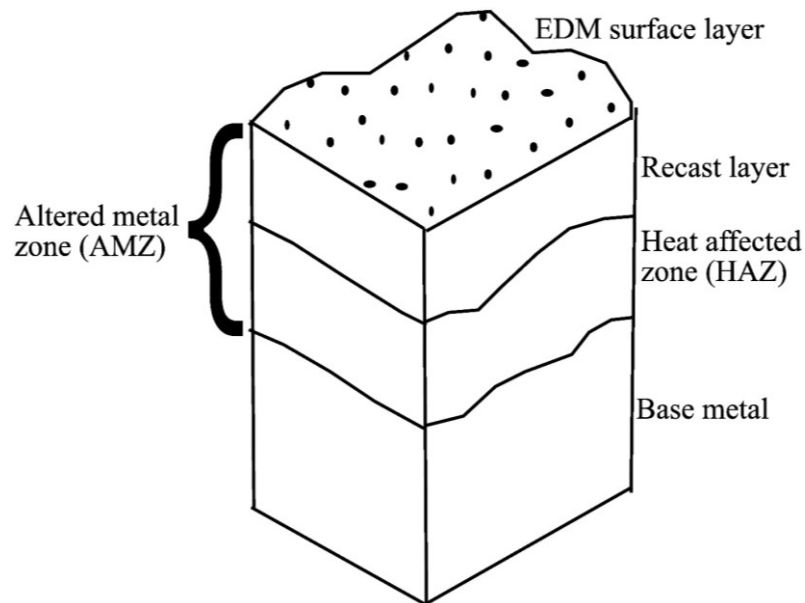
Fig. 1.4 Layers of an EDMed surface

Apart from productivity (MRR), surface integrity of the machined component plays a vital role in the selection of a machining process. Surface integrity deals basically with two issues, i.e., surface topography and surface metallurgy (possible alterations in the surface layers after machining). Surface integrity greatly affects the performance, life and reliability of the component. Typically EDM results in two kinds of surface or sub-surface layers, i.e., recast layer, heat affected zone (HAZ) as shown in Fig. 1.4. If molten material from the workpiece is not flushed out quickly, it will re-solidify and harden due to cooling effect of the dielectric, and gets adhered to the machined surface. This thin layer (about 2.5 to 50 μm) is known as 're-cast layer or white layer'. It is extremely hard and brittle and hence often causes microcracks to nucleate and proliferate. The layer next to recast layer is called 'heat affected zone'. Heating, cooling and diffused material are responsible for the presence of this zone. Thermal residual stresses, weakening of grain boundary, and consequent formation of cracks are some of the characteristics of this zone. The application of higher discharge energy results in deeper HAZ and subsequently deeper cracks. Excessive local thermal expansion and subsequent contraction may result in residual tensile stresses in the eroded layer [4]. The surface finish achieved during EDM is also influenced by the chosen machining conditions. Surface finish is primarily governed by the pulse frequency and energy per spark.

1.4 Categories of EDM

EDM facilitates the machining in a number of ways, a lot of these operations are similar to conventional machining operation, for instance milling and die sinking. A variety of classifications are possible and recent developments in its technology append new operations owing to increase in various requirements. A simple and general classification can be given in view of standard applications such as,

1. Die sinking EDM
2. Electric discharge milling (ED milling)
3. Electric discharge grinding (EDG)
4. Wire EDM (WEDM)
5. Micro-EDM (μ-EDM)

1.4.1 Die sinking EDM

Die sinking EDM, comprises a tool electrode and workpiece that are immersed in an insulating dielectric fluid. A pulsating power supply that produces a voltage potential, connects the tool and workpiece. A constant gap between the tool and the workpiece is maintained by a servo motor control of the tool holder. As tool moves towards the workpiece, dielectric breaks down into electrons and ions, creating a plasma column between two electrodes. A momentary flash jumps between the electrodes. Automatic movement of tool, towards workpiece takes place as the spark gap increases due to metal erosion. Thus the process continues without any interruption. As a result, the complementary shape of the tool electrode accurately sinks into the workpiece.

1.4.2 Electric discharge milling

Electric discharge (ED) milling is an evolution of CNC contouring EDM. A rotating cylindrical electrode follows a programmed path in order to obtain the desired shape of a part, like a cutter used in conventional computerized numerical controlled (CNC) milling. Compared to traditional sinking EDM, the use of simple electrodes in ED milling eliminates the need for customized electrodes. In the ED milling, the simple shape electrode does layer-by-layer milling to get a three-dimensional complex parts, at the same time, electrical discharges occur repeatedly to remove materials along the programmed path. According to the discharge status between the electrode and the workpiece, the control system determines the forward and withdrawal feed rate of the electrode [5].

1.4.3 Electric discharge grinding

Electric discharge grinding (EDG) is the process which works on the same principle as EDM. A rotating wheel made of electrically conductive material, is used as a tool. A part of the grinding wheel (cathode) and workpiece (anode) both are immersed in the dielectric, and are connected to DC power supply. The rotating motion of the wheel ensures effective flow of dielectric in the IEG, and hence flushing the gap with dielectric can be eliminated. Mechanism of material removal is exactly same as in EDM except that rotary motion of the tool helps in effective ejection of the molten material. Contrary to conventional grinding, there is no direct physical contact between the tool and workpiece, hence fragile and thin sectioned specimens can be easily machined. EDG is also considered to be economical compared to the conventional diamond grinding [1].

1.4.4 Wire EDM

Wire EDM uses a very thin wire of 0.02 to 0.03 mm diameter usually made of brass or stratified copper as electrode and machines the workpiece with electric discharges by moving either the wire or workpiece. Erosion of workpiece by utilizing spark discharges is very same as die sinking EDM. The predominant feature of a moving wire is that a complicated cut can be easily machined without using a forming tool. This process is frequently used to machine plates about 300 mm to manufacture dies, punches, and tools from hard materials which are difficult to machine using other processes.

1.4.5 Micro-EDM

The present trend of miniaturization of mechanical parts has given μ-EDM a considerable research attention. Using this process, it is possible to produce shafts and microholes diameter as less as 5 μm, and also intricate three-dimensional shapes [6]. It is extensively utilized for the fabrication of micro arrays, tool inserts for micro-injection molding, and hot embossing. In the beginning, μ-EDM was employed mostly for fabricating small holes in metal sheets. Owing to the versatility of the process, currently it is used in the manufacturing of micro molds and dies, tool inserts, micro filters, micro fluidic devices, housings for micro-engines, surgical equipment etc.

1.5 Variants of EDM

Notwithstanding the capability to machine virtually any electrically conductive material, the applications of electric discharge machining (EDM) are restricted to a few

industries, due to poor productivity and surface quality of the machined components. Over the years, researchers have developed new variants to EDM for enhancing its performance. Some of them include the rotation of tool, ultrasonic vibration of the tool/workpiece/dielectric, and utilization of powder-mixed dielectric.

1.5.1 Rotation of tool

Rotary motion is given to tool electrode, in the normal direction to the workpiece surface. Centrifugal force induced through rotary motion, drags the dielectric in to the inter electrode gap, enabling easier debris removal. Other advantages of the technique over stationary electrode include reduced tendency of arcing and improved sparking efficiency which finally lead to higher MRR, diminished too wear and surface roughness [7,8].

1.5.2 Ultrasonic vibration of tool/workpiece

The higher efficiency gained by the employment of ultrasonic vibration is mainly attributed to the improvement in dielectric circulation which facilitates the debris removal and the creation of a large pressure variation between the electrode and the work piece, as an enhancement of molten metal ejection from the surface of the workpiece [9]. Zhang et al. [10] proposed spark erosion with ultrasonic frequency using a DC power supply instead of the usual pulse power supply. The pulse discharge is produced by the relative motion between the tool and work piece simplifying the equipment and reducing its cost. They have indicated that it is easy to produce a combined technology which benefits from the virtues of ultrasonic machining and EDM.

Vibro-rotary motion (combination of vibration and rotation) of tool produces superior MRR compared to simple vibration or rotation alone [11]. Moreover, use of ultrasonic vibration under micro-EDM regime has also been found to be quite productive. When vibration is imparted in the workpiece there is an improvement in flushing efficiency. Additionally increase in amplitude and frequency during ultrasonic vibration assisted micro-EDM enhances MRR [12–14].

1.5.3 Near-dry or dry EDM

In dry EDM, tool electrode is formed to be thin walled pipe. High-pressure gas or air is supplied through the pipe. The role of the gas is to remove the debris from the gap and to cool the inter electrode gap. The technique was developed to decrease the pollution caused by the use of liquid dielectric which leads to production of vapor during machining and the cost to manage the waste. Gaseous environment generally involves helium, argon,

oxygen and air [15–17]. In near dry EDM, mixture of gas and fluid in mist environment is utilized as dielectric medium [18].

1.5.4 Powder-mixed EDM (PMEDM)
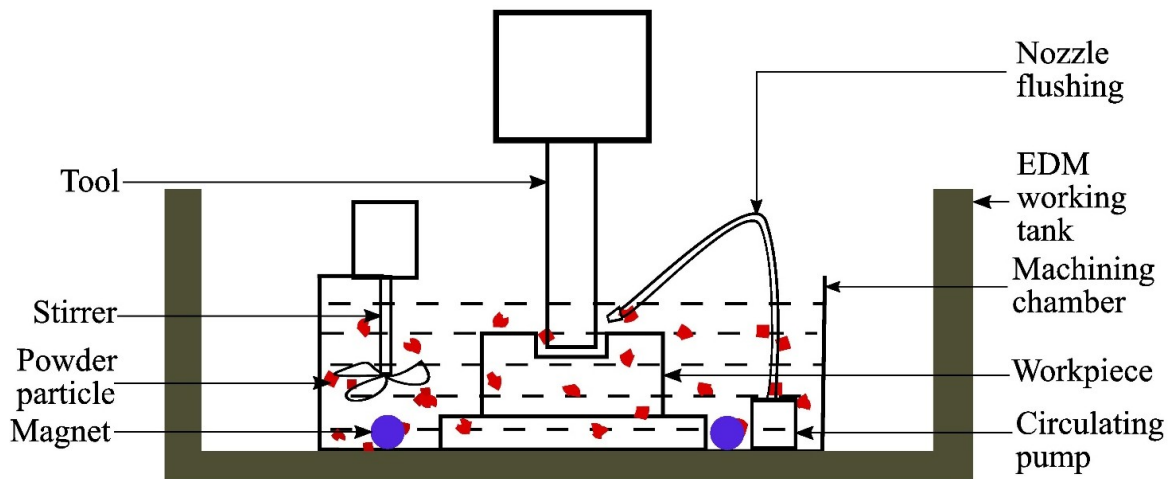
Fig. 1.5 PMEDM setup

In PMEDM, the addition of suitable powder particles to the dielectric leads to superior surface finish combined with better machining rates compared to those for conventional EDM (without powder). A typical dielectric circulation system used in PMEDM is shown in Fig. 1.5. This kind of specially designed system is mounted in the working tank of an EDM setup. A stirrer or a micro-pump is provided to avoid the settling of powder particles at the bottom of dielectric reservoir. It also helps to prevent the stagnation of the powder particles on the workpiece surface. A set of permanent magnets is provided to separate the debris from the powder particles through the filtering system. This separation is possible only when the workpiece is magnetic in nature and the powder material is not.

Current understanding of the PMEDM is presented here as the process is yet to be fully established. In PMEDM, fine powder particles are suspended in the dielectric oil. An electric field is created in the inter-electrode gap (IEG) when sufficient voltage (about 80 to 320V) is applied between them. Ionization of dielectric takes place as in the case of conventional EDM. Under the applied electric field, positive and negative charges accumulate at the top and bottom of the powder particles respectively (Workpiece positive and tool negative case). The capacitive effect of the electrodes leads to the formation of chains of powder particles. First discharge breakdown occurs where the electric field density is the highest (between 'a' and 'b' in Fig. 1.6). This breakdown may be between two powder particles or a powder particle and an electrode (Tool or workpiece).

Redistribution of electric charges takes place after the first discharge and electric charges gather at point 'c' and 'd'. Further discharge happens between these powder particles and the other particles where electric field density is highest [19,20].

Enlargement of discharge gap: Size of the discharge gap largely depends on the electrical and physical properties of the powder particles. Under high-temperature machining conditions, the free electrons present in electrically conductive powder particles reduce the overall resistance of the dielectric. The improved conductivity helps the spark to be generated from a longer distance and thus enlarges the discharge gap [21,22].

Widening of discharge passage: After the first discharge, powder particles in IEG get energized and move rapidly along with ions and electrons. These energized powder particles colloid with dielectric molecules and generate more ions and electrons [19]. Thus, more electric charges are produced in PMEDM compared to conventional EDM. Also increased discharge gap aids in the reduction of hydrostatic pressure acting on the plasma channel. These two phenomena ensure the widening of the discharge passage. The enlarged and wide discharge column decreases the intensity of discharge energy leading to the formation of large shallow cavities on the workpiece surface.
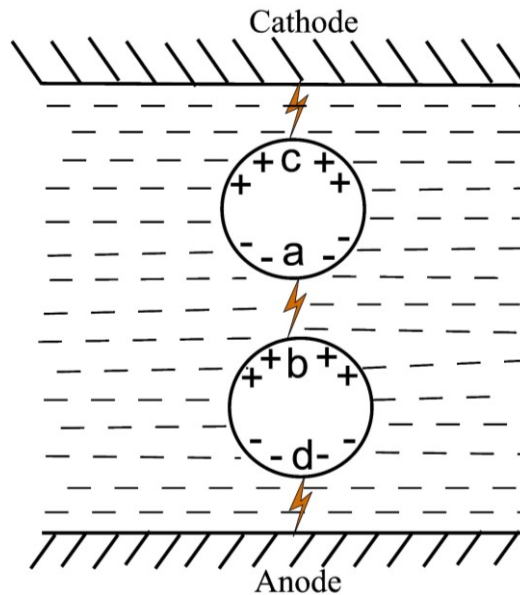
Fig. 1.6 Series discharging in PMEDM [18]

Multiple discharges: Multiple discharge paths are observed in PMEDM due to the rapid zigzag movement of the suspended powder particles ensuring uniform distribution of energy and formation of multiple craters in single pulse duration. Unlike conventional

EDM, the discharge waveform in the case of PMEDM is significantly different from the input pulse. Voltage fluctuates rapidly within single pulse duration due to multiple discharges [23,24].

1.6 Applications of PMEDM

EDM has been used in manufacturing of aerospace components such as fuel system, engine, impeller and landing gear components where high temperature and high-stress conditions prevail. However, the safety and life of the components were questionable due to poor surface integrity. Application of PMEDM process in place of conventional EDM adequately addressed the problem arising due to poor surface integrity. Some of the specific applications of PMEDM in automobile industry include the manufacturing of engine blocks, cylinder liners, piston heads and carburetors. With the increased precision, accuracy and the capability to be used under micro machining domain, PMEDM is also used to produce medical implants and surgical equipment. Some of the specific devices include surgical blades, dental instruments, orthopedic, spinal, ear, nose, and throat implants. Surface modification in the form of electro discharge coating is also realized by PMEDM technique. Therefore, light metallic alloys can be surface treated for wear resistance applications typically in automobile and aerospace industries.

Chapter 2
Literature review

The invention of powder-mixed EDM (PMEDM) process took place around late seventies and the first publication came in 1980 [25]. In PMEDM, the addition of suitable powder particles to the dielectric leads to a superior surface finish, and better machining rate compared to those for conventional EDM (without powder-mixed dielectric). A novel EDM two-tank system was first developed and marketed by Mitsubishi [26]. One of the tanks consisted of standard dielectric oil and the second one contained powder-mixed dielectric. After completion of initial machining operation in the first tank, the tool head moved to the second tank to perform the finish machining. However, the extensive application of PMEDM in the industry requires a thorough understanding of its mechanism and the influence of different powder characteristics on performance measures.

The emphasis in the current section is given on influence of powder characteristics and machining parameters on various responses. Some of the major application areas, variants of the basic PMEDM process and potential future direction of research are also discussed.

2.1 Influence of powder characteristics

Jahan et al. [27] presented a comprehensive analytical modelling of PMEDM process. Fig. 2.1 shows the schematic representation of different forces acting on a powder particle present in the inter-electrode gap. In Fig. 2.1, F_l, F_c, F_d, F_e and 'f' are lift, columbic, drag, electric, friction (direction only) forces respectively. W denotes the self-weight of the particle. The derived formula for breakdown energy of powder-mixed dialectic is provided in Eq. (2.1).

$$E_{br}^2 = E_i^2 - 2\sigma T \frac{1}{\varepsilon_1}\left(\frac{\varepsilon_p + 2\varepsilon_1}{\varepsilon_p - \varepsilon_1}\right)\left[\frac{1}{r^3}\left(\ln\frac{N_f}{N_i}\right)\right] \quad (2.1)$$

where E_i = Initial voltage for concentration N_i, E_{br} = Breakdown voltage for final concentration N_f, σ = Boltzmann constant, T = Temperature, ε_1 = Permittivity of dielectric, ε_p = Permittivity of powder particle and r = Radius of powder particle.

14
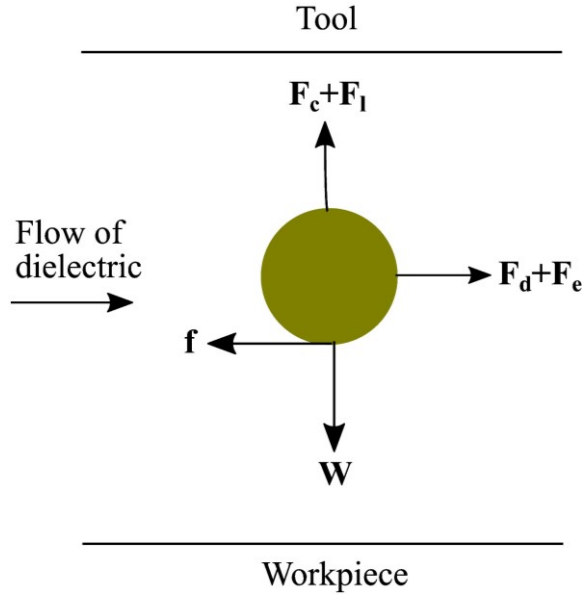
Fig. 2.1 Different forces acting on a powder particle

From Eq. (2.1) it is evident that E_{br} depends on particle radius and change in concentration 'N', permittivity of the particles and dielectric. For no addition of powder particles or unchanged concentration ($N_f = N_i$), the value of $E_{br} = E_i$, which means no change in breakdown strength.

The derived expression for spark gap during PMEDM is given in Eq. (2.2).

$$d_2 = \alpha d_1 \left(1 + \frac{r + h_p}{g_d} \right) \qquad (2.2)$$

where α = Field enhancement factor for small protrusion, g_d = Distance between bottom of the particle and micro-peak, h_p = Height of the protrusion. d_1= Spark gap without powder suspension. From Eq. (2.2), it is clear that spark gap during PMEDM (d_2) is higher than that of conventional EDM process (d_1).

Density, size, electrical and thermal conductivities are some of the critical characteristics of the powder particles that significantly affect PMEDM process.

Increase in electrical conductivity of the dielectric, and resulting extension of discharge gap in PMEDM, as discussed earlier, enhance spark frequency and facilitate easy removal of debris from the machining zone [27,28].

High thermal conductivity of powder particles removes a large amount of heat from the discharge gap leading to reduction in discharge density. Therefore, only shallow craters are formed on the workpiece surface [29,30]. Number of surface cracks developed on the

15

machined surface are also reduced along with their width and depth, as the intensity of discharge energy is less in PMEDM compared to conventional EDM process [31,32].

Table 2.1 Properties of various powder materials

Material	Density (g/cm^3)	Electrical resistivity (μΩ-cm)	Thermal conductivity (W/m-K)	Reference(s)
Aluminum (Al)	2.70	2.89	236	[24,27,29–31,33,35–52]
Alumina (Al$_2$O$_3$)	3.98	103	25.1	[27,44,53–57]
Boron Carbide (B$_4$C)	2.52	5.5 x 10^5	27.9	[58–61]
Carbon nanotubes (CNTs)	2.00	50	4000	[48,62–71]
Chromium (Cr)	7.16	2.60	95	[29,30,36,72–75]
Copper (Cu)	8.96	1.71	401	[29,36,45,46,76–78]
Graphite (C)	1.26	103	3000	[21,27,28,30,37,45–48,78–94]
Molybdenum disulfide (MoS$_2$)	5.06	106	138	[95–97]
Nickel (Ni)	8.91	9.5	94	[98–100]
Silicon (Si)	2.33	2325	168	[28,37,39,43,44,48,55,101–116]
Silicon Carbide (SiC)	3.22	1013	300	[23,30,34–36,38,117–126]
Titanium (Ti)	4.72	47	22	[127–130]
Tungsten (W)	19.25	5.3	182	[28,45,46,76,77,131–134]

The number of powder particles in the electrode gap at a given instant increases with the decrease in their size. As a consequence, overall discharge energy increases, but it is more evenly distributed in a larger area. Hence, energy density gets diminished [27]. Formation of multiple number of smaller craters during a single discharge also takes place. Use of smaller powder particles has, therefore, produced higher material removal rate (MRR) and superior surface quality compared to the larger size particles of the same material [33–36].

The powder particles with low density can balance themselves better against the surface forces, allowing even distribution of particles throughout the dielectric [48,68]. Low density also minimizes the amount of powder particles settling at the bottom of the tank, thereby bringing down the requirement of powder quantity. Lighter particles also cause small explosive impact on the molten metal [29]. Some of the frequently used powder materials in PMEDM along with their properties are presented in Table 2.1.

Yeo et al. [119] observed a circular growth within the crater during powder-mixed μ-EDM process due to the deposition of the powder material on the workpiece surface. However, no such growth could be found during conventional EDM process.

Along with physical, electrical and thermal properties, concentration of powder material in the dielectric also causes a significant change in the responses. Higher concentration is effective in multiplying the number of discharges which in turn augment MRR [113,114]. The accentuation of multi-sparking in a single pulse-on time due to increase in powder concentration reduces the energy per spark resulting in low surface roughness (SR) [38]. However, too many powder particles in the discharge gap hinder the discharge energy transfer to the workpiece. It also leads to arcing and short-circuiting that ultimately results in low MRR and poor surface quality [97,116].

On the contrary, Jabbaripour et al. [30] observed a fall in MRR, when powders like Al, Gr, SiC, Cr and Fe had been impregnated in the dielectric during the PMEDM of ϒ-TiAl intermetallic. Such reduction was attributed to the reduced energy density at the discharge spot due to enlarged IEG and widened discharge passage. Consequently, the reduced impulsive force of the plasma channel on the workpiece surface also resulted in the formation of small craters leading to the reduction in MRR. Powders like Fe and Cr that have low thermal conductivity and high density produced superior MRR. According to the authors, powders that have high thermal conductivity take away the heat from the discharge spot resulting in lower values of MRR. Low-density particles produced poor MRR as they mixed well with the dielectric and dissipated more heat to the dielectric. Hence, Al with highest thermal conductivity and the least density among the used powders produced the worst MRR.

Wu et al. [40] achieved excellent surface finish by mixing a surfactant (Polyoxythylene-20-sorbitan monooleate) along with Al powder in dielectric during the EDM of SKD 61 die steel. The added surfactant acted as a steric barrier to prevent the agglomeration of the powder particles. It was also found that usage of only surfactant as an additive could reduce the recast layer thickness as it increased the overall conductivity of the dielectric [135].

Radial pattern and a trace of the circular annulus at the edge of the machined surface were found by Wang et al. [111,112], at 4 g/l concentration of Si powder in the dielectric while machining NAK-80 mold steel. All the negatively charged electrons colloid with the positive charges present on the workpiece surface generating enormous amount of heat energy. A track with branches radially growing outward was formed due to rapid heat transfer to surroundings. The track disappeared at higher levels of powder concentration as powder congregation died down.

Among others, Tsai et al. [44,53,55] established the feasibility of polymer particles (starch, polyaniline) as additives during the PMEDM of stainless steel. Starch when added along with Al_2O_3 powder in silicone oil produced better surface quality than pure Al_2O_3 powder. Wong et al. [37] utilized crushed glass as an additive to machine AISI-01, SKH 54 tool steels and found no significant effect of it on both MRR and surface quality due to its very poor electrical and thermal conductivities. Sari et al. [68] and Prabhu et al. [62–65,67,69–71] concluded that carbon nanotubes (CNTs) mixed in the dielectric resulted in huge improvement of MRR compared to other powder materials which was attributed to the low density and high thermal conductivity of CNT. The low density allowed the particles to be better balanced against the surface forces of the dielectric. Hence, there was an even distribution of the particles in the dielectric. High thermal conductivity also helped in the uniform distribution of discharge energy over the large surface area. Mai et al. [48] used CNTs fabricated using floated catalytic chemical vapor deposition (CVD) method during the PMEDM of NAK-80 steel. The uniform diameter and straight pin shape of these CNTs allowed easier separation from each other compared to CNTs produced using conventional CVD technique. As high as 66 % increase in MRR and 70 % decrease in SR were reported with 0.4 g/l concentration of CNTs.

2.2 Influence of machining parameters

The combined and individual characteristics of dielectric, powder, tool and workpiece material along with other machining parameters affect the PMEDM process significantly [45–47]. The effect of important process parameters on the machining characteristics of PMEDM process is discussed below.

2.2.1 Dielectric

Apart from commercial EDM oils, kerosene, and deionized water are widely used in PMEDM. The higher thermal conductivity and specific heat of pure water take away the heat from the machining zone resulting in a better cooling effect [117]. Simultaneously, kerosene forms carbides and water forms oxides on the machined surface. Carbides require more thermal energy to melt compared to oxides [58]. Hence, higher MRR and less TWR were realized with deionized water than kerosene as dielectric. But kerosene produces better surface finish. Usage of emulsified water (water+emulsifier+machine oil) as the dielectric by Liu et al. [137] produced higher MRR and better surface quality than pure kerosene. This was attributed to the increase in overall electrical conductivity of the dielectric due to the ionization of water soluble anionic compound emulsifier present in the

emulsified oil. Some of the important properties of dielectrics used in PMEDM are provided in Table 2.2.

Table 2.2 Properties of typical dielectrics used in PMEDM [136]

Dielectric	Specific heat (J/kg-K)	Thermal conductivity (W/m-K)	Breakdown strength (kV/mm)	Flash point (ºC)
Deionized water	4200	0.62	65-70	Not applicable
Kerosene	2100	0.14	24	37-65
Mineral oil	1860	0.13	10-15	160
Silicon oil	1510	0.15	10-15	300

2.2.2 Polarity

Discharge current takes place due to flow of both electrons and ions. For short pulse-on time, the discharge current is mainly due to the electron current. When the pulse-on time is long, the discharge consists of a large amount of ion current. Hence for better MRR and lower TWR, positive polarity (workpiece +ve) with short pulse-on time should be preferred while negative polarity (workpiece -ve) can be used for long pulse-on time [23].

With positive polarity, some of the molten metal re-solidified at the center of craters, resulting in bulging effect during the EDM of titanium alloy using SiC additive in the dielectric [118]. It also led to a greater accretion of powder material on the machined surface [127]. Furthermore, deep cavities with predominant ridges were observed with negative polarity. This means that high MRR could be achievable with negative polarity but with coarser surface [111,138].

2.2.3 Peak current

MRR increases with peak current due to an increase in discharge energy [139–143]. The increase in peak current also increases the number of electrons and ions per unit volume, thereby increasing the pressure in the plasma channel. As a consequence, impulsive force per unit area (specific impulsive force) increases allowing an easier ejection of the molten material [115,116]. Tool wear increases with increasing pulse current as more particles strike the surface. However, pulse energy dominates striking effect at high pulse current leading to less tool wear [33,99].

Surface quality deteriorates with peak current as the quantity of material removed per discharge increases due to rise in discharge energy [144]. Large and deep craters were observed at high pulse currents [40]. The thickness of recast layer also increases as more

material melts and re-solidifies [132]. Apart from material transfer, rapid heating and quenching at high pulse currents elevate the microhardness of the machined surface [145].

2.2.4 Pulse-on time

MRR increases with pulse-on time due to an increase in pulse energy [33,57,115]. Too long pulse-on time causes an expansion of the plasma channel that in turn leads to the reduction of energy density and impact force. Thus, MRR is reduced at long pulse-on time [135]. SR also decreases with pulse-on time due to aforesaid reasons. Short-circuiting and incomplete removal of debris from the discharge area make the process unstable and degrade the surface quality at high pulse-on times [40,92,108]. More debris is formed and adheres to the machined surface as the pulse-on time increases the productive machining time. This also causes an increase in recast layer thickness [58,123]. There is an initial decrease in microhardness of the machined surface, followed by subsequent rise with further increase in pulse-on time due to material transfer [145]. TWR decreases with the pulse-on time due to the time available for heat transfer from the molten crater to the body of the electrode. High wear resistance of the electrode due to the deposited carbon on it increases the TWR [81]. More overcut (OC) was observed with high pulse-on time owing to the large amount of material removed per spark [138].

Yasar et al. [125] observed many small pits within the crater with a decrease in pulse-on time. At high pulse-on times, the initial discharge pushes the powder particles outwards and forms a clearer space at its center. Simultaneously, the particles around it form sub-discharges resulting in several pock marks.

2.2.5 Duty cycle

MRR increases with duty cycle due to an increase in spark energy. But, MRR starts declining when duty cycle becomes too long as the process becomes unstable, and arcing may take place due to unfavorable flushing conditions [33,57,135]. For the same reasons, minimum SR is obtained at moderate value of duty cycle [33]. Extended duty cycles do not allow the gasses and accumulated debris to escape resulting in reduced tool wear [99].

2.2.6 Gap voltage

When gap voltage becomes too large, the time required for bridging the discharge gap with ions and electrons increases due to an increased spark gap resulting in low MRR [135]. Less energy density and energy loss in the discharge gap also decrease the MRR [57]. There

is an initial hike in SR as MRR increases. However, too high gap voltage decreases the SR owing to increase in spark gap [33,133]. The deposited layer thickness increases with gap voltage as the expansion of spark gap allows more powder into it. However, further increase in gap voltage diverges and reduces the discharge column thereby reducing the recast layer thickness (WLT) [118].

Kumar et al. [87] observed a reduced TWR by employing a cryogenically treated copper electrode during EDM of Inconel 718 using dielectric suspended with graphite powder. This was attributed to improved electrical and thermal conductivity of the cryogenically treated tool due to its grain refinement.

Wong et al. [37] achieved mirror-finish for SKH-54 tool steel using Al suspended dielectric, but not for AISI-01, which emphasizes the significance of the workpiece composition in PMEDM process. Surface finish improved with machining time when AISI H13 mold steel was machined with Si impregnated dielectric by Pecas et al. [102]. Too much dielectric flow degraded the surface quality due to the instability in the machining zone [38]. The turbulent flow of the dielectric increases the tool wear as well [68].

2.3 Major research areas of PMEDM

The following methodologies have been adopted to analyze and expand the areas of application of PMEDM process.

2.3.1 Rough machining

PMEDM process was traditionally used in finish machining. The application of PMEDM in rough machining was first attempted by Zhao et al. [19]. Problems like high tool wear rate, improper flushing of debris at high machining parameters have to be addressed before applying PMEDM in rough machining. Mai et al. [48] investigated the rough machining parameters for PMEDM of NAK80 die steel using CNTs. High peak current and long pulse-on time resulted in high machining rate [47].

2.3.2 Finish machining

Finish machining is one of the major application areas of PMEDM. Good surface finish achieved through PMEDM reduces other finish machining operations and the cost associated with it. A mirror-like reflective surface can be obtained using PMEDM at low discharge energy parameters [101,102]. Roughness of the machined surface increases with the increase in tool size even at low energy settings [37,102].

Mohri et al. [101] used planetary tool motion for fine machining of H13 steel using Si powder. The machined surface showed good corrosion resistance. Wong et al. [37] observed mirror-like surface finish with Al suspended dielectric for SKH-54. Semi-conductive C and Si powders produced very fine finish but not mirror-like surface. Pecas et al. [102] achieved a mirror finish during EDM of H13 tool steel using Si powder-mixed dielectric. Further, a significant improvement in surface finish was realized with increasing machining time.

Wu et al. [40] used a surfactant along with Al powder in the dielectric. This combination produced lower SR owing to uniform dispersion of powder particles in the dielectric. Pecas et al. [109,110] analyzed the influence of powder concentration, electrode area and dielectric flow rate on the crater characteristics of the machined surface. Crater dimensions, i.e., diameter and depth, decrease with powder concentration due to the dispersed multi-sparking in a single discharge. However, crater depth increases at high powder concentration levels due to an increase in discharge energy.

2.3.3 Micromachining

Recent advancements in micro-electro-mechanical systems (MEMS) and micro-mechanical equipment like micro-pumps, micro-engines and micro-robots necessitate precise micromachining processes. Due to its capability to accomplish high surface finish, powder-mixed micro-EDM (μ-EDM) has resulted in better surface quality and precision compared to conventional μ-EDM [146,147]. Chow et al. [38] machined micro-slits on titanium alloy using Al and SiC suspended dielectrics. It was observed that Al powder produced a large slit expansion due to its high electrical and thermal conductivity. A gray zone was found under the actual recast layer during the μ-PMEDM of Inconel 718 using Si powder due to its high heat of fusion [39]. Nanopowders of graphite, Al and Al_2O_3 were used by Jahan et al. [27,83,85] during μ-PMEDM of WC10%Co alloy. No significant effect was found with Al_2O_3, while Al and graphite powders significantly improved the MRR and surface quality. Kibria et al. [58–60] used boron carbide (B_4C) powder in kerosene as well as deionized water during drilling of microholes on titanium alloy. Diameter variation at entry and exit of the hole was more for kerosene dielectric than deionized water. At low peak current, such variation was more for powder-mixed dielectrics than pure dielectric, but less for high peak current. Chow et al. [23] fabricated micro-slits on titanium alloy using silicon carbide suspended pure water as dielectric. It was observed that the expansion of micro-slits was more for positive polarity.

2.3.4 Surface modification

Electro discharge coating (EDC) using powder metallurgy tool has been used extensively for surface coating and modification. However, the surface becomes inaccurate due to high tool wear associated with the process. Surface coating and surface alloying using PMEDM has received much attention in recent years due to its improved accuracy.

Various researchers have added different powders to dielectric to achieve a desired quality of the machined surface for specific applications. Chen et al. [130] machined grade 4 pure Ti with Ti mixed-deionized water using a grade 4 Ti electrode. The machined component was biocompatible and could be used as a dental implant. Due to its excellent lubricity properties, usage of molybdenum sulfide (MoS_2) as an additive solved the problem of lubrication of sliding parts in space for EDMed stainless steel parts [148]. Zain et al. [139] used tantalum carbide (TaC) powder during the EDM of stainless steel (SUS 304) to achieve excellent surface microhardness. Bhattacharya et al. [28] studied the effect of various electrode and powder combinations on the microhardness of the machined surface. Results indicated that the combination of W-Cu electrode and W powder produced the hardest surface compared to the surfaces obtained by utilizing graphite and Si powder suspended dielectrics. The investigation of Fong and Chen [29] on the EDM of SKD 11 steel revealed that Cr powder which has low electrical resistivity and hardness has produced fine surface finish compared to SiC additive.

Furutani et al. [127] used different kinds of electrodes for the accretion of TiC on AISI 1049 carbon steel while adopting Ti mixed dielectric. While a thin powder metallurgy electrode produced a high concentration of accretion of TiC, rotating gear shape electrode during PMEDM resulted in the accumulation of TiC over a large area. Urea was suspended in pure water during EDM of titanium to form a TiN ceramic layer [144]. Microhardness of the machined surface also increased due to this layer. Further, surfaces machined using PMEDM process showed an improved resistance to corrosion due to effective surface modification [101].

2.3.5 Machining of nonconductive materials

Kucukturk and Cogun [84] produced holes on different nonconductive ceramics through EDM by suspending graphite powder in the dielectric. Before machining, all the workpieces were coated with a conductive layer to initiate the sparking. After the erosion of coated layer the discharge process still continues due to the formation of a thin layer consisting of decomposed carbon particles of the dielectric, graphite powder and particles of the coated layer adhering to the machined surface.

2.3.6 Optimization of PMEDM process

Quite a few single objective optimizations in PMEDM were performed in the past using the design of experiment (DOE) methods like Taguchi[34,61,80] or response surface methodology (RSM) [73,75,98].

Bhattacharya et al. [77] performed a multi-objective optimization of MRR, TWR and SR using analytic hierarchy process (AHP) during the PMEDM of various steels with different combinations of tool and powder materials. Singh et al. [34] and Talla et al. [52] analyzed the impact of process parameters on PMEDM characteristics of aluminum/alumina metal matrix composite using silicon carbide and aluminum powders respectively. Multi-objective optimization using gray relational analysis (GRA) was also proposed to find the optimal combination of process parameter settings. Assarzadeh and Ghoreishi[57] investigated the effect of various electrical and non-electrical process parameters on MRR and SR during the PMEDM of CK45 alloy using alumina, copper and silicon carbide additives in dielectric. The experiments were carried out using RSM design, and optimal parameter combination was determined using desirability approach. A hybrid multi-response optimization employing TOPSIS and GRA was performed by Tripathy and Tripathy [149] during the EDM of H-11 die steel using chromium powder-mixed dielectric. Padhee et al. [114] attempted simultaneous optimization of multiple objectives using a non-traditional technique called non-sorted genetic algorithm (NSGA). Empirical models for the optimization were generated using RSM.

2.3.7 Numerical modelling of PMEDM process

Substantial amount of research work has been reported in the numerical modelling of EDM process. However, very few research work has been attempted in the numerical modelling of PMEDM process. Kansal et al. [82] developed an axisymmetric 2D thermal model to predict temperature distribution with respect to various PMEDM process parameters. The model was further utilized to estimate crater size and subsequently the MRR. Along with temperature distribution and MRR, Bhattacharya et al. [86] accomplished a 3D finite element model to predict thermal residual stresses induced during PMEDM process. Further, mathematical models were developed to predict the radius and height of crater during PMEDM process [89]. Tan and Yeo [150] established 3D finite element models for surface integrity aspects such as maximum surface roughness (R_{max}) and recast layer thickness by considering multiple crater effect. Similarly, Vishwakarma et al. [151] and Singh et al. [94] have accomplished finite element models to predict MRR by considering single and multiple crater theories respectively.

2.4 Variants of PMEDM

PMEDM process is further improved by making small adjustments to the setup. Some of those variations are discussed below.

2.4.1 PMEDM with the rotary tool

Effect of the powder particles on the machined surface can be enhanced by using a rotary tool. Powder particles from the surroundings are dragged into the machining zone due to the centrifugal force of the rotating tool [150,152]. This increase in the concentration of particles in the machining zone enhances the overall effectiveness of the powder particles.

2.4.2 PMEDM with ultrasonic vibration

MRR and surface quality can be improved considerably when ultrasonic vibration is imparted to the tool. More molten material is removed by each discharge due to enhanced abrasive action of the powder particles caused by the vibrating tool. SR also decreases owing to the wear-out of the crater edges [138].

Instead of the tool, Prihandana et al. [88,90] employed ultrasonic vibration to the workpiece in the forward-backward direction during μ-EDM process using graphite powder suspended dielectric. Such vibration pumped out the debris from the IEG and allowed the fresh dielectric to flow into it, yielding better MRR compared to conventional EDM.

In another set of experiments, Prihandana et al. [21,95] used an ultrasonic bath to vibrate the dielectric. This ultrasonic vibration of the dielectric reduces the adhesion of debris to the workpiece besides preventing the settling of powder particles at the bottom of the tank. The combined effect has resulted in the improvement of MRR, as more powder particles enter the IEG.

2.4.3 Near dry PMEDM

Very little work has been reported in the area of near dry PMEDM. Debris removal is a primary concern in near dry EDM. The enlarged discharge gap in PMEDM makes the way for easier debris removal thereby enhancing the process stability in near dry PMEDM [153,154].

Some of the major developments in PMEDM, starting from its inception have been summarized in Table 2.3.

Table 2.3 Evolution of PMEDM process

Year	Author(s)	Area of research	Major findings
1980	Erden and Bilgin [25]	Usage of impurities (Cu, Al, Fe, and C) in the dielectric.	Time lag (ignition delay) reduced compared to conventional EDM. MRR and tool wear rate (TWR) increased and remained constant with impurity concentration.
1981	Jeswani [79]	Ultrasonic vibration of the tool in graphite powder-mixed dielectric.	More molten material is removed per each discharge due to enhanced abrasive action of the powder particles caused by the vibrating tool. SR also decreased owing to the wear out of the crater edges.
1991	Mohri et al. [101]	Planetary tool motion in Si powder-mixed dielectric.	Time required for removing the cusps reduced significantly due to the grinding action of powder particles provided by the planetary tool motion.
1995	Ming and He [32]	Usage of lipophilic surface agents (liquids) as additives.	Liquid additives also enhanced the MRR. Microhardness of the machined surface has improved. Recast layer thickness and number of micro-cracks got reduced.
2000	Chow et al. [38]	Employment of rotating Cu diskette as electrode.	Micro-slits were successfully fabricated. Slit expansion (overcut) depends on electrical conductivity of the powder material.
2001	Tzeng and Lee [36]	Influence of powder properties on PMEDM characteristics	High spark gap was observed for large particles. Small particles produced high MRR.
2001	Furutani et al. [127]	Electro discharge coating (EDC) using PMEDM process	Gear-shaped rotating electrode produced wider area of accretion compared to other electrodes as it drags more powder particles into the sparking zone.
2005	Wu et al. [40]	Usage of surfactant along with Al powder in dielectric	Agglomeration of powder particles was reduced. Machining rate and surface quality were improved.
2005	Yan et al. [144]	Urea with distilled water as dielectric	A ceramic TiN layer formed on the workpiece. Microhardness of the machined surface was improved. Better surface finish obtained compared to conventional EDM.

2006	Kansal et al. [106]	Multi-objective optimization of PMEDM process	Performed multi-objective optimization using Taguchi approach and utility concept.
2008	Kansal et al. [82]	Numerical simulation of PMEDM process	2D transient thermal models were developed to analyze temperature distribution and material transformation in PMEDM process. Prediction model for MRR was developed.
2008	Tsai et al. [53]	Electrorheological (ER) fluid (Silicone oil + starch) as dielectric	Al_2O_3 mixed ER fluid produced the polishing effect on the machined surface. The addition of starch along with Al_2O_3 decreased the surface roughness from 0.3 µm to 0.06 µm.
2009	Prihandana et al. [95]	Usage of ultrasonic bath inside the dielectric tank	Ultrasonic vibration of the dielectric significantly improved the MRR as it prevented the powder particles and debris at the bottom of the tank.
2009	Gao [153]	Near dry PMEDM	A gas-liquid-solid medium was used as a dielectric medium. The main intention was to reduce the amount of dielectric and improve the debris removal process.
2010	Kucukturk and Cogun [84]	Machining of nonconductive materials	Nonconductive materials were coated with a conductive layer and machined with graphite powder-mixed dielectric.
2010	Tsai et al. [55]	Polymer powder as additive	High molecular weight polyaniline (PANI-emer) produced a finer finish than Si powder.
2013	Tan et al. [150]	Simulation by considering multiple crater phenomenon in PMEDM	2D transient thermal models based on finite element method were developed for powder-mixed µ-EDM by considering multiple craters.
2014	Chen et al. [130]	Development of metal based biomedical implant	Machined Ti alloy with pure Ti suspended dielectric. Wettability of the machined surface was increased.

2.5 Motivation and objective of research work

From the review of past research work, it is evident that PMEDM has strong potential in enhancing MRR and surface finish. However, the criteria for powder material selection, based on specific requirements and application, are still unknown. Therefore, it is essential

to comparatively evaluate the performance of some of the commercially available powders and correlate the same with different properties of these powder materials.

Moreover, previous studies primarily focused on MRR and surface finish in PMEDM. Existing works also reveal that the process parameters such as powder concentration, peak current, pulse-on time, duty cycle and gap voltage have significant influence on EDM characteristics. While these performance measures undoubtedly have enormous significance, surface integrity of the machined components perhaps plays a more vital role in influencing the performance during their intended applications and deciding the service life of the same components. Therefore, investigation into influences of various PMEDM parameters on various aspects of surface integrity is of utmost relevance. However, such studies have rarely been reported so far.

It is also observed from the literature that various methodologies were adopted to analyze different response characteristics in PMEDM. However, very few attempts have been made to correlate the interaction effect of PMEDM process parameters with process performance.

A great deal of research work pertaining to PMEDM of different grades of steel has been published during the last decade or so. In recent times, nickel-based super alloys are widely used in aerospace, chemical and marine industries owing to their supreme ability to retain the mechanical properties at elevated temperature in combination with remarkable resistance to corrosion. Some of the properties of these alloys such as low thermal conductivity, strain hardening tendency, chemical affinity and presence of hard and abrasives phases in the microstructure render these materials very difficult-to-cut using conventional machining processes. Although some amount of studies have been reported on EDM of nickel-based super alloys, exploits of PMEDM process in machining such alloys have hardly been explored. Few studies pertaining to EDM and PMEDM evaluated basic machining characteristics of Inconel 718. However, different other grades of super alloy with variation in chemical composition and properties should also be considered in order to attain deeper insight into the role of process mechanics on such alloys. Inconel 625 is one such grade of nickel-based super alloys of which EDM characteristics and role of powder materials have yet to be evaluated.

Considering all the gaps or incompleteness in the reviewed literature discussed above, the major objective of the current research work is to investigate the influence of various powder additives and process parameters on different performance measures with significant emphasis on various aspects of surface integrity in PMEDM during machining of Inconel 625.

The detailed objectives specific to the different sections of chapter 4 (results and discussion) are formulated as follows:

1. To establish 3D numerical models correlating temperature distribution, material removal rate (MRR), and residual stress with different process parameters such as peak current, pulse-on time, duty cycle and gap voltage during PMEDM utilizing different powders (graphite, aluminum and silicon).

2. To study the influence of powder materials, their size and concentration as well as PMEDM parameters, arranged using RSM-based design of experiment, on material removal rate (MRR) and radial overcut (ROC).

3. To investigate the effect of powder materials, their concentration as well as different process variables on various aspects of surface integrity such as crater distribution, surface morphology, surface crack density, surface roughness, formation of altered layers including recast layer and heat affected zone (HAZ), microhardness at surface and sub-surface regions, phase changes, grain size, lattice strain and residual stress after machining.

Chapter 3
Experimental details
3.1 Development of experimental setup

All experiments were conducted on a die sinking EDM machining setup (make: Electronica, India; model: ElektraPlusPS 50ZNC) as shown in Fig. 3.1. Since it was planned to use a fresh dielectric fluid with varying concentrations of powder for every experiment, a separate dielectric circulation system was designed, fabricated and attached to the existing machine as indicated in Fig. 3.1.
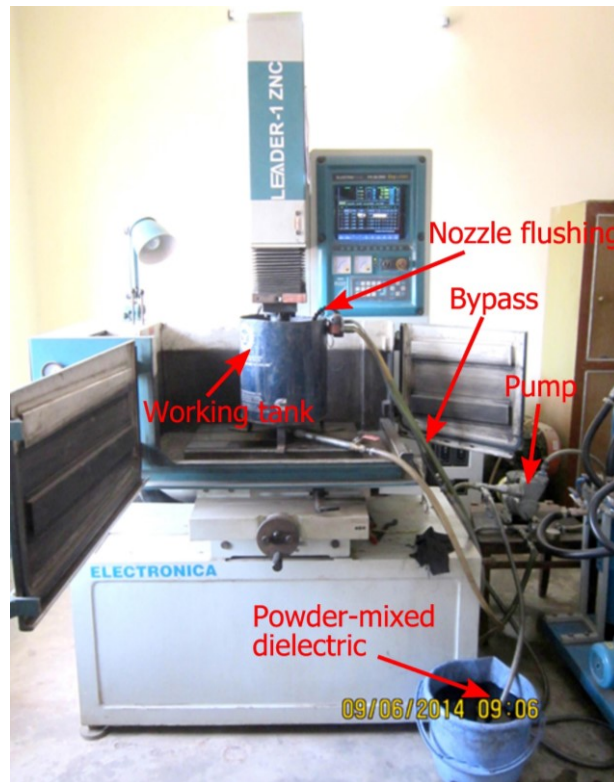
Fig. 3.1 Experimental setup

Schematic diagram of PMEDM setup is depicted in Fig. 3.2. The recirculation system consists of a cylindrical working tank of 20 liters, a work holding fixture, a dielectric reservoir (bucket), 0.5 HP pump and delivery pipes. A pressure gauge was also attached to the system to measure the dielectric pressure during experimentation. The pump receives

the dielectric fluid from the outlet of the cylindrical tank and recirculates it to the tool-work inter electrode gap to flush out the debris. The continuous circulation of the dielectric fluid avoids the settlement of powder particles in the flushing system. In the current investigation, side jet flushing was selected to flush out the debris.
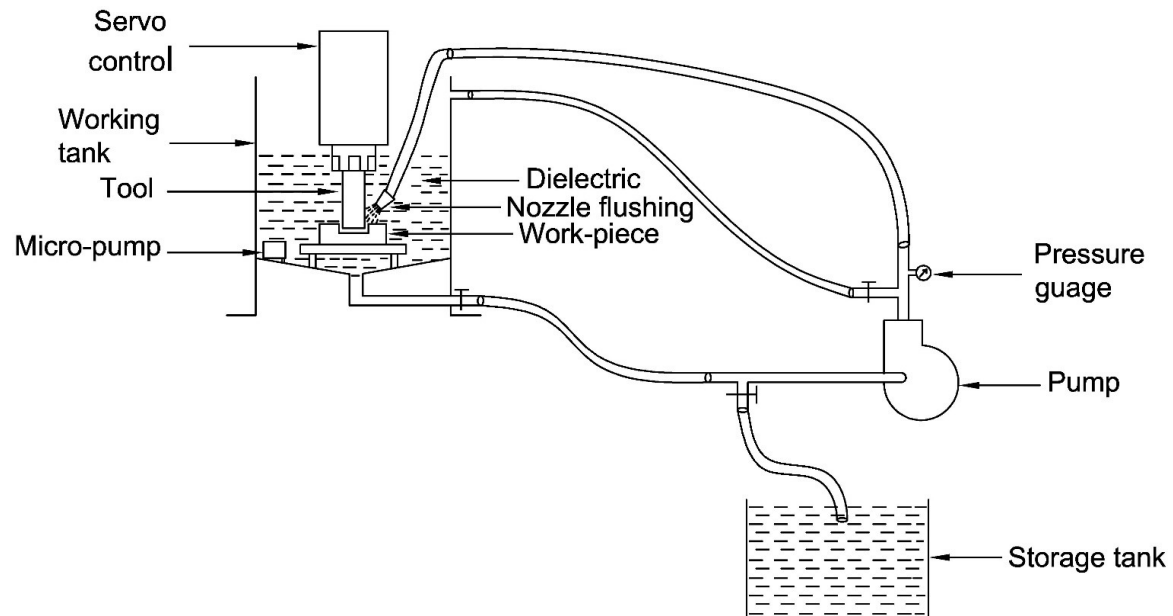
Fig. 3.2 Schematic of dielectric circulation system

3.2 Selection of materials

3.2.1 Workpiece and tool

Nickel-based super alloys have a wide range of industrial applications because of their properties, such as good tensile strength, excellent resistance to oxidation and corrosion along with thermal stability. Inconel 625 is an austenitic nickel-based super alloy, possessing excellent corrosion resistance to severe working environments. The chemical constituents of Inconel 625 are given in Table 3.1. The presence of chromium resists oxidization whereas molybdenum prevents corrosion in non-oxidizing environments. Niobium reduces crack formation during welding by stabilizing the weld pool. The High percentage of nickel arrests cracking due to chloride stress corrosion. Due to aforesaid properties, some of the specific applications of Inconel 625 include acid storage hardware, tubes for sour gas handling, chimney liners, furnace equipment and distillation columns [155]. However, the same properties pose a great challenge during conventional machining processes. Since Inconel 625 is conductive in nature, it is suitable for electric discharge machining. However, EDM characteristics of the same alloy have hardly been reported so

31

far. Hence, Inconel 625 was chosen as the workpiece material in the form of thin plates with dimensions of 40 mm x 40 mm x 5 mm. The properties of Inconel 625 are listed in Table 3.2. An electrolytic copper tool with a diameter of 12 mm and length of 60 mm has been used to perform the experiments.

Table 3.1 Chemical composition of as-received Inconel 625

Element	Weight (%)
Aluminum (Al)	0.32
Silicon (Si)	0.35
Sulfur (S)	0.01
Titanium (Ti)	0.38
Chromium (Cr)	22.36
Manganese (Mn)	0.35
Iron (Fe)	4.58
Nickel (Ni)	58.74
Niobium (Nb)	3.87
Molybdenum (Mo)	9.04

Table 3.2 Properties of Inconel 625 [155]

Mechanical properties			
Density	$8440 \ kg/m^3$		
Young's modulus	$2.07 \times 10^{11} \ N/m^2$		
Poisson's ration	0.308		
Maximum yield strength	634.3 MPa		
Electrical resistivity	129-134 $\mu\Omega$-cm		
Melting temperature	1573 K		
Thermal properties			
Temperature (K)	Thermal conductivity (W/m-K)	Coefficient of thermal expansion (m/m-ºC)	Specific heat (J/kg-K)
300	9.8	1.31×10^{-5}	410
500	14.1	1.33×10^{-5}	456
700	17.5	1.44×10^{-5}	511
900	20.8	1.53×10^{-5}	565
1100	25.2	1.62×10^{-5}	620

3.2.2 Powder materials

Three different powders i.e., aluminum (Al), graphite and silicon (Si) which have significant variation in their thermo-physical characteristics as shown in Table 3.3 were used as additives in kerosene dielectric. The average particle size of all the three powders claimed by the manufacturer (Sigma-Aldrich), is ~15 μm.

Table 3.3 Properties of powder materials

Property (Units)	Graphite	Aluminum	Silicon
Electrical resistivity (μΩ-cm)	5-30	5	10000
Thermal conductivity (W/m-K)	25-470	238	163
Heat of fusion (kJ/mol)	117	10.79	50.21
Specific heat (J/kg-K)	710	910	710
Melting temperature (ºC)	3550	660	1414
Density (g/cm^2)	1.26	2.7	2.33
Mohs hardness (HV)	1.5	3	6.5

3.3 Process parameters

Five process parameters i.e., powder concentration (C_p), peak current (I_p), pulse-on time (T_{on}), duty cycle (τ) and gap voltage (V_g) were selected for the present research work. Choice of parameters was influenced by the fact that these parameters have significant impact on various EDM and PMEDM characteristics as evident from Chapter 2. Lateral flushing with a pressure of 0.5 kg/cm^2 and positive polarity (workpiece +ve) were used for all the experiments. Tool working time and lift time were set to be 0.7 s and 0.3 s respectively. Servo sensitivity (SEN) which controls the speed of quill was chosen as 7. Anti-arc sensitivity (ASEN) which does not allow sparking when IEG is not clean was set to be 5. Depth of machined hole of 1 mm was kept same for all the samples throughout.

3.4 Design of experiments using RSM

The experiments were designed according to central composite design (CCD) of response surface methodology (RSM). It is a collection of mathematical and statistical techniques that are useful for modelling and analysis of problems in which output or response is influenced by several variables and the goal is to find the correlation between the response and the variables [156]. RSM has effectively been applied to study and optimize the processes. It offers enormous information from a small number of

experiments. In addition, it is possible to detect the interaction effect of the independent parameters on the response. The model easily clarifies the effect for binary combination of the independent process parameters. Furthermore, the empirical model that relates the response to the independent variables is used to obtain information. It has been widely used in analyzing various processes, designing the experiment, building models, evaluating the effects of several factors and searching for optimum conditions to give desirable responses and reduce the number of experiments [157–159]. The experimental values are analyzed, and the mathematical model is then developed that illustrates the relationship between the process variable and response. A second-order model generated using a typical RSM design is given in Eq. (3.1).

$$y = \beta_0 + \sum_{i=1}^{m} \beta_i x_i + \sum_{i=1}^{m} \beta_{ii} x_i^2 + \sum_{i,j=1, i \neq j}^{m} \beta_{ij} x_i x_j + e \tag{3.1}$$

where y is the corresponding response, X_i is the input variables and X_i^2 and $X_i X_j$ are the squares and interaction terms, respectively. The unknown regression coefficients are β_0, β_i, β_{ii} and β_{ij}, and the error in the model is depicted as 'e'.

Table 3.4 Process parameters and their levels

Parameter	Symbol	Level					Units
		-2	-1	0	1	2	
Powder concentration	C_p	0	2	4	6	8	g/l
Peak current	I_p	2	4	6	8	10	A
Pulse time	T_{on}	100	200	300	400	500	μs
Duty cycle	τ	55	65	75	85	95	%
Gap voltage	V_g	40	50	60	70	80	V

The process parameters and their levels are provided in Table 3.4. The ranges of the parameters were so chosen that the process falls under semi-finishing operation. The CCD is capable of fitting second order polynomial and is preferable if curvature is assumed to be present in the system. In the current research work, half factorial 2^K design (K factors each at two levels) was considered to reduce the experimental runs. Half factorial 32 run (2^5) unblocked design having 16 factorial points, 10 (2K, where K=5) axial points and 6 center points is shown in Table 3.5. Design Expert 7.0 software was used to determine the experimental design. According to the experimental design, 32 number of runs for each powder was obtained. Therefore, one complete set of experiment involves 96 number of runs. Each of the runs was repeated twice so that a total of 96 x 2 number of experimental runs were performed in the entire study.

Table 3.5 Plan of experiments

Standard order	Run number	Point type	C_p	I_p	T_{on}	τ	V_g
17	1	-1	-2	0	0	0	0
13	2	1	-1	-1	1	1	1
11	3	1	-1	1	-1	1	1
15	4	1	-1	1	1	1	-1
9	5	1	-1	-1	-1	1	-1
7	6	1	-1	1	1	-1	1
5	7	1	-1	-1	1	-1	-1
3	8	1	-1	1	-1	-1	-1
1	9	1	-1	-1	-1	-1	1
29	10	0	0	0	0	0	0
21	11	-1	0	0	-2	0	0
20	12	-1	0	2	0	0	0
25	13	-1	0	0	0	0	-2
26	14	-1	0	0	0	0	2
28	15	0	0	0	0	0	0
32	16	0	0	0	0	0	0
23	17	-1	0	0	0	-2	0
24	18	-1	0	0	0	2	0
30	19	0	0	0	0	0	0
31	20	0	0	0	0	0	0
27	21	0	0	0	0	0	0
22	22	-1	0	0	2	0	0
19	23	-1	0	-2	0	0	0
8	24	1	1	1	1	-1	-1
16	25	1	1	1	1	1	1
2	26	1	1	-1	-1	-1	-1
10	27	1	1	-1	-1	1	1
12	28	1	1	1	-1	1	-1
4	29	1	1	1	-1	-1	1
6	30	1	1	-1	1	-1	1
14	31	1	1	-1	1	1	-1
18	32	-1	2	0	0	0	0

3.5 Performance measures

Effect of powder materials and EDM parameters was investigated in terms of a large number of performance measures in the current research work. Productivity of EDM or PMEDM process is typically characterized by MRR while dimensional accuracy is expressed in terms of ROC. The present investigation attempts major emphasis on various aspects of surface integrity in terms of surface roughness, surface morphology, surface crack density, surface microhardness along with depth profile, microstructure and phases, grain size, lattice strain, white layer thickness and residual stress. Methodology of assessing these response characteristics is discussed below.

3.5.1 Material removal rate (MRR)

Weight of the workpiece before and after the experiment was measured using an electronic balance (Make: Shinko Denshi, Japan; Model: DJ 300S) shown in Fig. 3.3. Time duration of each experimental run was recorded using a digital stop watch. Eq. (3.2) was used to calculate the MRR.

Fig. 3.3 Electronic weighing machine

$$MRR = \frac{w_b - w_a}{\rho * T_{mach}}$$

(3.2)

where W_b and W_a are weights of the specimen before and after the machining, ρ is the density of workpiece material and 'T_{mach}' is machining time.

3.5.2 Surface roughness (SR)

Surface roughness expressed in terms of center line average (R_a) is defined as the average departure of roughness profile from the center line. The expression of R_a is given in Eq. (3.3).

$$R_a = \frac{1}{l}\int |y(x)|\, dx \qquad (3.3)$$

where l is the sampling length, y is height of peaks and valleys of roughness profile and x is the profile direction.

Fig. 3.4 Stylus type profilometer

Measurement of center line average i.e., R_a was carried out using a portable stylus type profilometer (Make: Taylor Hobson, Model: Surtronic 3+) shown in Fig. 3.4. The cut off and sampling lengths were set to be of 0.8 and 4 mm respectively. Measurements were carried out at three randomly chosen locations on each of the machined specimens. The average of three values was taken as the surface roughness of a particular specimen.

3.5.3 Radial overcut (ROC)

Cavities produced during EDM are always larger than the electrode size. The radial difference between size of electrode and cavity is called radial overcut (ROC). It becomes important when components with close tolerances are required to be produced. In the current investigation, a tool makers microscope (Make: Carl Zeiss, Germany) with a least count of 1 μm shown in Fig. 3.5 was used to measure the diameter of the machined holes. Radial overcut was calculated using Eq. (3.4).

$$ROC = \frac{D_h - D_t}{2} \tag{3.4}$$

where D_h is the machined hole diameter and D_t is the tool diameter.

Fig. 3.5 Tool makers microscope

3.5.4 Microhardness

Fig. 3.6 Vickers microhardness tester

Microhardness of the machined surfaces was measured at three different places using a Vickers microhardness tester (Make: Leco, USA; Model: LV 700) shown in Fig. 3.6. During measurement, a load of 50 g was applied with a dwell time of 15 s. The mean value was determined by taking the average of three measured values. In order to determine hardness depth profile machined surfaces of all the specimens were sectioned along the transverse length using a wire EDM setup (Make: Electronica, India; Model: Ecocut, ELPULS 15), followed by polishing using water proof polishing paper (SiC, grades: 220, 400, 600 and 1000). Subsequently, microhardness was measured along the cross-section of the cut specimens by maintaining a constant distance of 20 μm between each indentation starting from the edge of machined surface.

3.5.5 Surface morphology and crack density (SCD)

Surface morphology and density of surface cracks were evaluated using scanning electron microscopy (SEM) images of different magnification using a system (Make: JEOL, Japan; Model: JSM-6480) shown in Fig. 3.7. The measurement of SCD was carried out by measuring the length of cracks on five randomly selected areas on each specimen with a constant magnification of 250x. The average crack length on each specimen was divided by the area of SEM micrographs to obtain the SCD.

Fig. 3.7 Photograph of SEM setup

3.5.6 Altered layer thickness (ALT)

Formation of altered layer (recast layer + heat affected zone) is a regular occurrence in EDM or PMEDM process. In order to measure such layer thickness, the cut specimens were first mounted and polished successively using water proof SiC papers with decreasing of grit sizes of 220, 400, 600 and 1000. Subsequently, the surface was polished with diamond paste (Make: HIFIN, India; Grade: 01-0S-47) and HIFIN Fluid of "OS" type using a polishing cloth (make: Selvyt, UK). Further, the specimens were etched using Keller's reagent (95 ml H_2O, 2.5 ml HNO_3, 1.5 ml HCl, 1 ml HF) for around 30 s. This was necessary in order to distinguish white layer from the parent material. The micrographs of white layer were then recorded at a magnification of 500x using SEM. The area of white layer was measured by PDF viewer software on each SEM micrograph and the mean of white layer thickness was obtained by dividing the measured area by the length of the micrograph.

3.5.7 Phases, grain size and lattice strain

Fig. 3.8 X-ray diffractometer

These characteristics of work material before and after machining were evaluated using X-ray diffraction (XRD) technique. XRD works on the principle of Bragg's diffraction law and its measurement was carried out on a multipurpose X-ray diffraction system (Make: Rigaku, Japan; Model: Ultima IV) shown in Fig. 3.8. In addition to identification of various phases, shifting and broadening of peaks were also analyzed. Peak

broadening is typically quantified by full width half maxima (FWHM). All such analyses were performed using X'pert High score software.

Furthermore, grain size of as-received powders which are presumably stress free was calculated using Scherrer's equation. Since PMEDM would cause lattice deformation and variation in grain size, Scherrer's equation could not be used for measurement of grain size and lattice strain simultaneously. Therefore, Williamson-Hall plot (linear) with the ability to effectively separate the influence of both the aspects [160] has been utilized to determine grain size and lattice strain of work material before and after machining under different conditions. The Williamson-Hall formula is given in Eq. (3.5).

$$\frac{\beta \cos\theta}{K\lambda} = \frac{4e\sin\theta}{K\lambda} + \frac{1}{L} \tag{3.5}$$

where β = Integral breadth of peak, θ = Braggs angle, λ = wavelength of X-ray radiation=0.15418 nm, L = average crystallite size measured in a direction perpendicular to the direction of specimen, K = a constant, can be taken as 0.9, ℓ = strain induced. A plot of $\frac{\beta \cos\theta}{K\lambda}$ against $\frac{4e\sin\theta}{K\lambda}$ gives a linear relation with a slope of 2e and intercept of $\frac{K\lambda}{L}$. The integral breadth of a diffraction peak was calculated after appropriate background correction followed by fitting the peak using Pseudo–Voigt function. Brag-Brentano mode of XRD was adopted for this purpose.

3.5.8 Residual stress

The residual stress on the machined surfaces was determined using $\sin^2 \psi$ technique while performing the measurement in a separate high resolution XRD system (HRXRD, Make: PANalytical). First, the major phase i.e., peak with highest intensity was identified from trial measurements which revealed (1 1 1) peak observed at $2\theta = 42.75°$ using Cu (λ = 1.5418 A°) radiation. The lattice spacing measurement was performed in 7ψ tilts. The Lorentz polarization, Kα-2 splitting and background corrections were performed for the measured intensities. Peaks were analyzed using the Gaussian curve fit.

3.5.9 Crater diameter

Since mixing of powder with dielectric has prominent influence on crater dimension, the same was measured using the microscopic images captured on an optical microscope (Make: Carl Zeiss, Germany) shown in Fig. 3.9. Diameter of three craters on each specimen was measured using PDF viewer software and the average value was considered.

Fig. 3.9 Optical microscope

Chapter 4
Results and discussion

4.1 Numerical modeling of temperature distribution, material removal rate and thermal residual stress

The blending of powders in dielectric fluid during EDM makes the discharge procedure more complicated and random with a sequence of discharges distributed all over the surface. For simplifying the analysis, a few reasonable presumptions without altering with the basic PMEDM procedure are considered.

4.1.1 Assumptions

1. The modelling and its study indicate results for a single spark.
2. Thermal characteristics of the workpiece material are functions of temperatures. The change in the shape of workpiece due to thermal heating is negligible.
3. Density and specific heat of the workpiece material are independent of temperature.
4. Transient thermal analysis and Gaussian heat flux on workpiece are chosen.
5. Fraction of heat that goes into the workpiece (K_w) continues to be same under all parameter settings.
6. Material flushing efficiency is considered to be 20%.
7. Transfer of heat energy to the electrode is by conduction. Convection is used on the top area of the workpiece which is in contact with powder-mixed dielectric.
8. Workpiece material is homogeneous and isotropic and is free from any stress before machining.
9. The influence of impulse force is not considered during modelling.

4.1.2 Heat flux and boundary conditions

The governing differential heat conduction equation for an axisymmetric solid is given by Eq. (4.1)

$$\rho C \frac{\partial T}{\partial t} = \left[\frac{1}{r} \frac{\partial}{\partial r} \left(Kr \frac{\partial T}{\partial r} \right) + \frac{\partial}{\partial z} \left(K \frac{\partial T}{\partial z} \right) \right] \tag{4.1}$$

where, ρ is the density, C is the specific heat and K is the thermal conductivity of the work material, T is the temperature, t is the time and r and z are coordinate axes shown in Fig. 4.1.

During pulse-on time, flow of electrons takes place from cathode to anode creating a plasma channel between them. Earlier, researchers have assumed such plasma channel as uniform heat flux. However, researchers who had used Gaussian heat distribution obtained more accurate and realistic results. Fig. 4.1 shows the distribution of heat flux to the workpiece. Guassian heat distribution is given by Eq. (4.2).

$$Q_W(r) = \frac{4.57 K_f V_g I_p R_w}{\pi r^2} \exp\left\{-4.5\left(\frac{r}{R}\right)^2\right\}$$

(4.2)

where, V_g and I_p are breakdown voltage and peak current during the process respectively, R_w is the fraction of heat transferred to the workpiece.
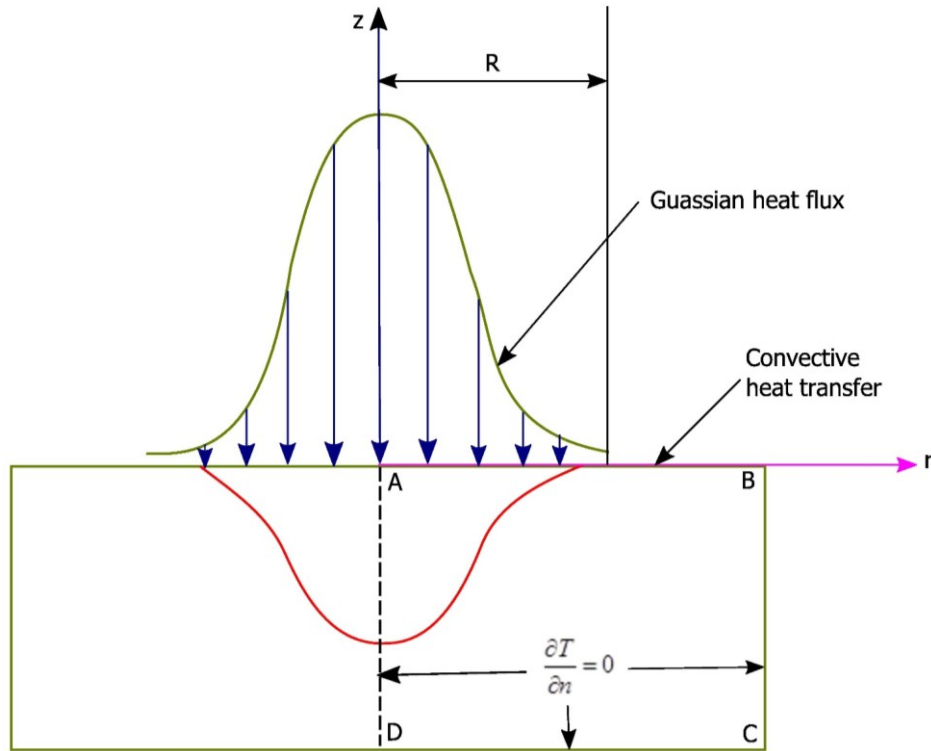
Fig. 4.1 Heat flux distribution in PMEDM

Various thermal boundary conditions applied during the PMEDM process are shown in Fig. 4.1. Heat is transferred as per Gaussian heat flux distribution on the top surface up to spark radius (R). Convective heat transfer takes place for the remaining portion. All other sides (BC, CD and AD) are considered to be insulated as there is no heat transfer along

44

these directions. These sides are sufficiently away from the spark region. The boundary conditions are mentioned below.

1. For AB boundary

$$K\frac{\partial T}{\partial z} = Q_W(r) \text{ where } r < R$$

$$K\frac{\partial T}{\partial z} = h(T - T_0) \text{ where } R <= r$$

2. For boundaries BC, CD and AD

$$\frac{\partial T}{\partial n} = 0$$

where, h is the heat transfer coefficient between the workpiece surface and powder mixed dielectric, $Q_W(r)$ is the heat flux owing to the spark, T_0 is the initial temperature which is equal to room temperature and T is the temperature.

4.1.3 Spark radius

In PMEDM process spark radius or its growth is a complex phenomenon and it involves many thermo-physical processes. Calculation of the spark radius by experimental or mathematical means is also a difficult issue. DiBitonto et al. [161] formulated a mathematical relation for spark radius. Erden [162], further modified the equation for spark radius in terms of power and discharge time. The equation for spark radius is given in Eq. (4.3).

$$R(t) = ZP^m T_{on}{}^n \tag{4.3}$$

where, $R(t)$ is the spark radius at a particular instant, P and T_{on} are power and pulse-on time respectively, Z, m and n are empirical constants. Kansal et al. [82] used a spark radius of 120 μm which is 30-50% more than that of Shankar et al. [163]. In the current study spark radius is assumed to be 100 μm which is in between above two values.

4.1.4 Material flushing efficiency

In most of the papers, researchers considered material flushing efficiency as 100 % [94,151], meaning entire melted material is removed from crater during flushing. But the experimental results show that only 10-30% of molten material is actually removed from the crater [161,164]. In the current study material flushing efficiency is assumed as 20 %. Thus, the error between predicted and experimental results can be reduced.

4.1.5 Methodology

PMEDM is a complicated process which involves many physical phenomena as well as interaction among them. FEM is an approximate method for real engineering problems. FEM makes it possible to simulate these problems related to PMEDM. To develop a model based on FEM, a powerful software is required which can consider all these aspects. ANSYS is such a software which uses FEM for the analysis of various processes. In the current study, numerical model and the analysis of the PMEDM process is carried out using FEM software ANSYS 15.0 utilizing transient thermal analysis (FLUENT) module. Geometry of the workpiece was prepared with a dimension of 1×1×0.25 mm for Inconel 625 the properties of which are listed in the Table 3.2. Then the model was meshed using 3D tetrahedral elements of 2.5 μm size. Fig. 4.2 shows the meshing of entire workpiece region of the developed model.
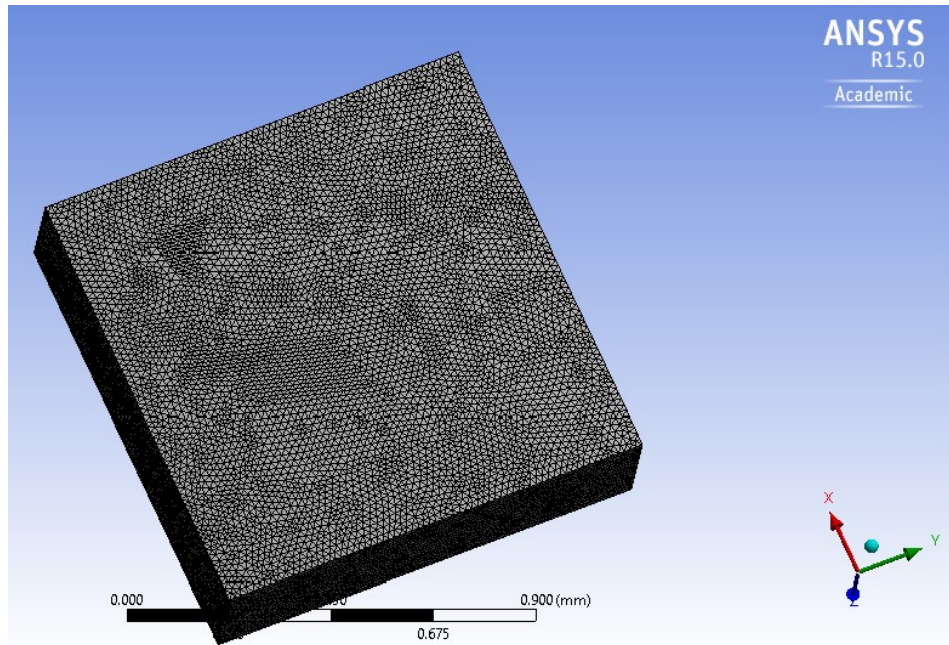
Fig. 4.2 Meshed workpiece material

Finite element simulation with ANSYS was performed for different process parameter settings to study the temperature profile after PMEDM. From the temperature profiles, the amount of volume removed during a single crater was calculated. The cooling rate and stresses induced due to the heating of the workpiece by spark was also evaluated for some select cases. The process parameters varied during this simulation work are powder material (graphite, aluminum and silicon), peak current, pulse-on time, duty cycle and gap voltage. Other parameters such as R_w and spark radius are kept constant.

Using the variables from Table 3.2 and Eq. (4.2), the heat flux values are calculated for different process settings. These calculated heat fluxes are used as thermal loading in ANSYS (FLUENT) environment for transient thermal analysis.

4.1.6 Temperature distribution
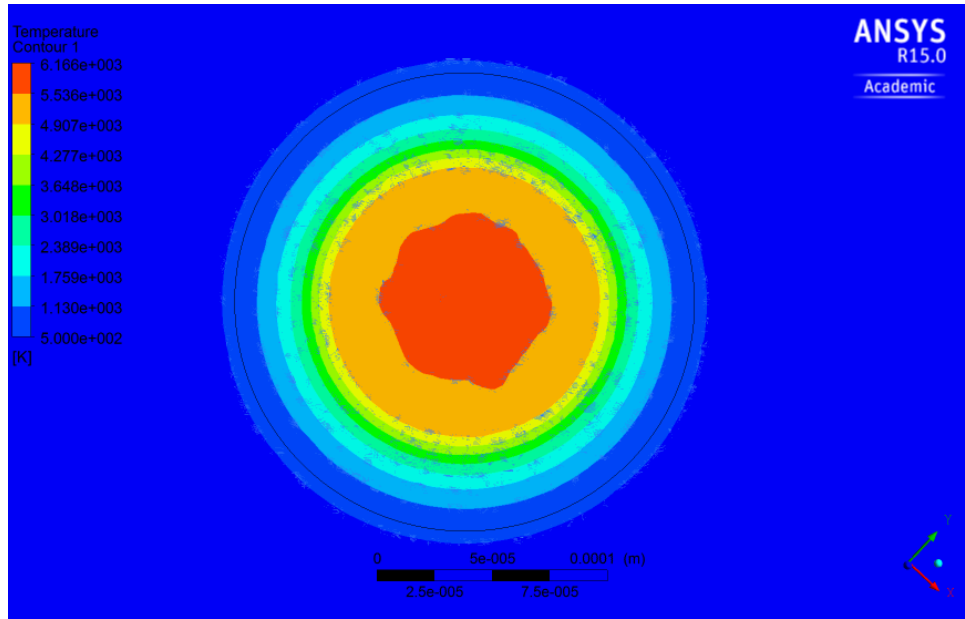
Fig. 4.3 Temperature distribution along the radial direction

A representative image of temperature distribution along the radial direction is shown in Fig. 4.3. It can be observed from Fig. 4.3 that the maximum temperature is generated at the center of the crater and with increase in radial distance the temperature drops. A Gaussian distribution was observed for temperature along the radial direction of the crater for all the levels of process parameters.

Temperature distribution in the depth direction at center of crater is shown in Fig. 4.4 as a sample representation. It can be observed that within a very short depth temperature drops very quickly to even below the melting point of the workpiece material. Similar observations were made for other parameter settings as well. For higher energy settings, this phenomenon takes place at a slightly more depth. Thus, the temperature in the radial direction follows a Gaussian distribution wherein it is maintained at a very high value in radial direction and substantially lower in the crater depth direction. This leads to a crater formation with larger diameter but small depth, thus, forming shallow craters.
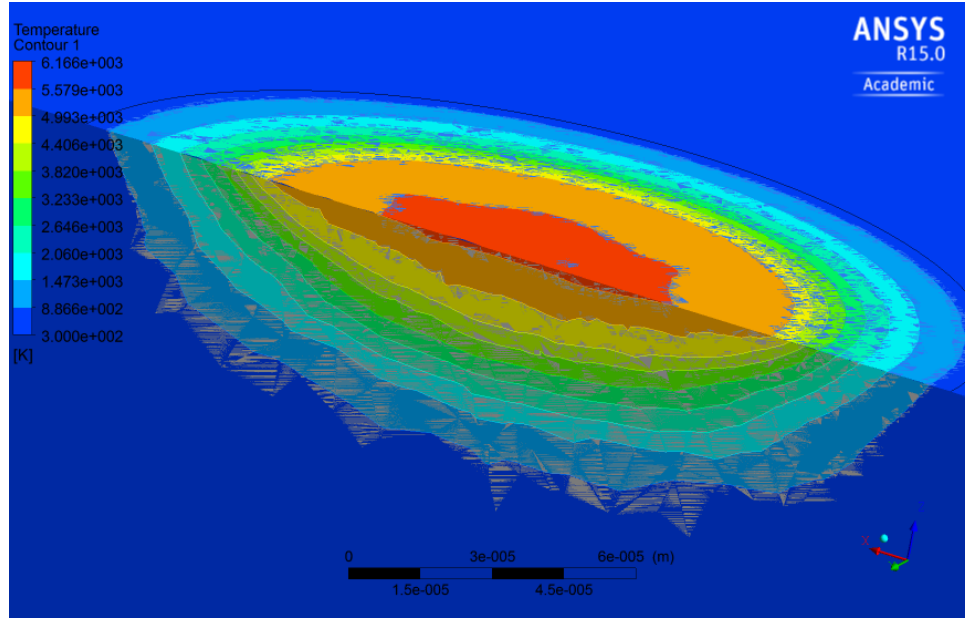
Fig. 4.4 Depth profile of the temperature distribution

Simulated temperature distribution was also identified in ranges to identify the different regions and provide an insight of the changes in the metal properties. The remaining workpiece material after removal of the crater volume assumes the shape of the region above melting temperature. It can be observed that the volume of material removed by the crater is broadly a part of a sphere and its volume can be calculated accordingly. As discussed earlier, the craters formed are of shallow depth. Overlapping of many such craters during actual material removal in PMEDM, may lead to a smoother finish of the machined surface. This may be one of the possible mechanims for achievement of superior surface finish during PMEDM process as observed by past experimental investigations discussed in chapter 2.

4.1.7 Determination of MRR

Prediction of MRR depends upon the crater morphology. The morphology of the crater is assumed to be hemispherical dome shape as observed in Fig. 4.5. The crater volume can be calculated by using Eq. (4.4).

$$C_v = \frac{1}{6}\pi d(3r^2 + d^2) \tag{4.4}$$

where r is the radius of spherical dome and d is the depth of the crater.

Total material removal in the entire machining time depends on number of pulses (*NOP*). It is calculated by dividing the total machining time by pulse duration as shown in Eq. (4.5).
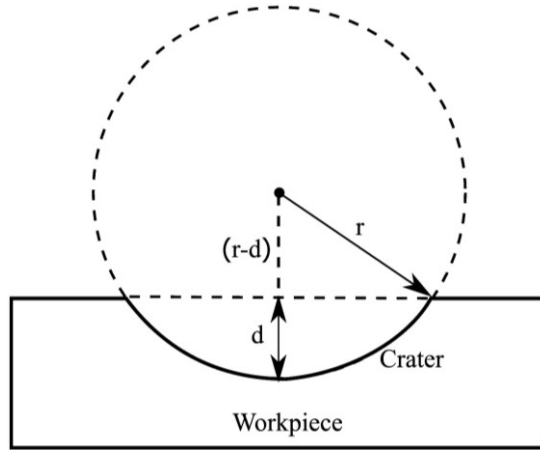
Fig. 4.5 Assumed crater shape
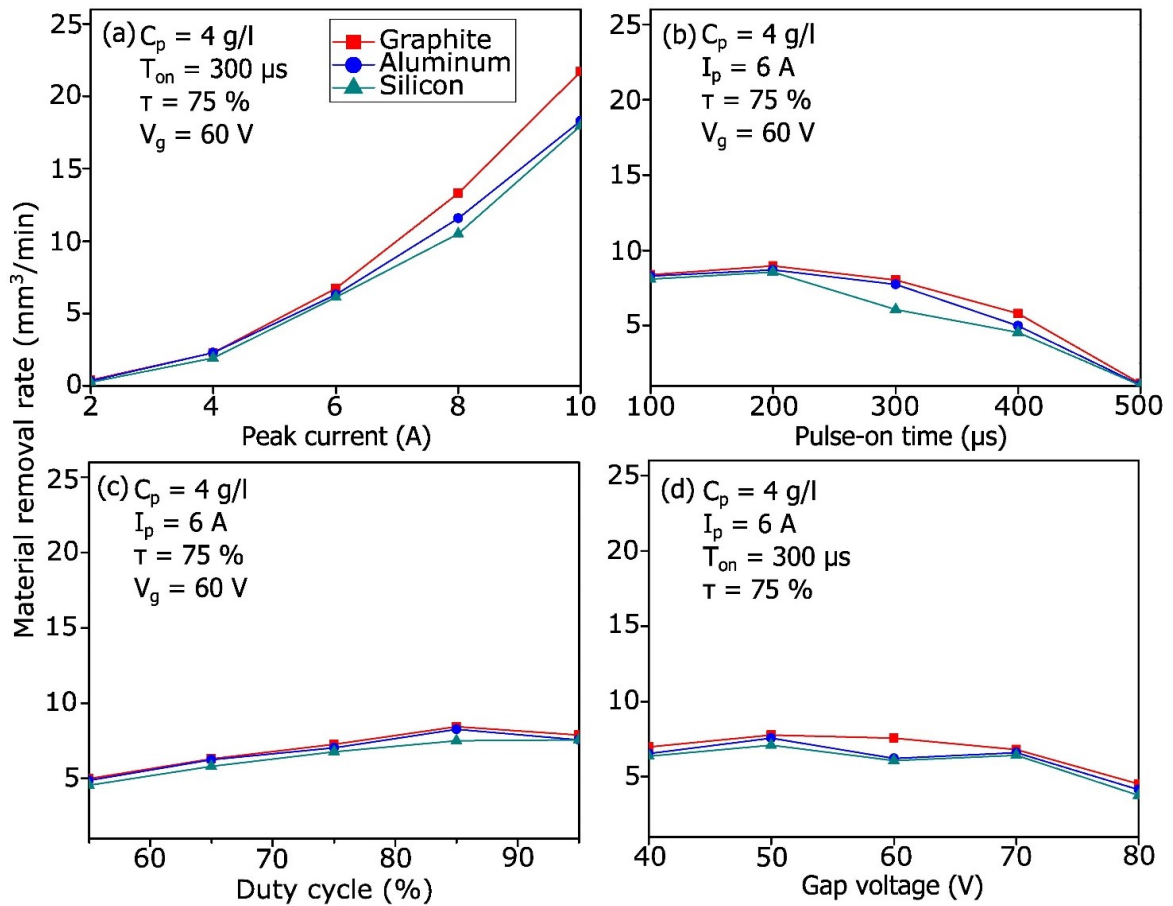
Fig. 4.6 Predicted MRR values for different experimental conditions

$$NOP = \frac{T_{mach}}{T_{on} + T_{off}} \tag{4.5}$$

where T_{mach} is the machining time, T_{on} is pulse-on time and T_{off} is pulse-off time.
The MRR for the given machining duration can be determined using Eq. (4.6).

$$MRR = \frac{C_v * NOP}{T_{mach}} \tag{4.6}$$

The predicted MRR values during PMEDM of Inconel 625 using three different dielectrics are presented in Fig. 4.6. The MRR values obtained using different powder-mixed dielectrics are very close to each other. Graphite powder-mixed dielectric produced slightly higher MRR compared to other two powders. MRR increases with peak current significantly due to the rise in thermal energy. MRR is all most constant upto a pulse-on time of 200 μs. Further increase in pulse-on time has diminished MRR due to the reduction in NOP as shown in Eq. (4.5). No significant variation in MRR is realized with respect to duty cycle and gap voltage. Careful observation would indicate that MRR declines slightly at too high duty cycle (95 %).

4.1.8 Determination of thermal residual stress
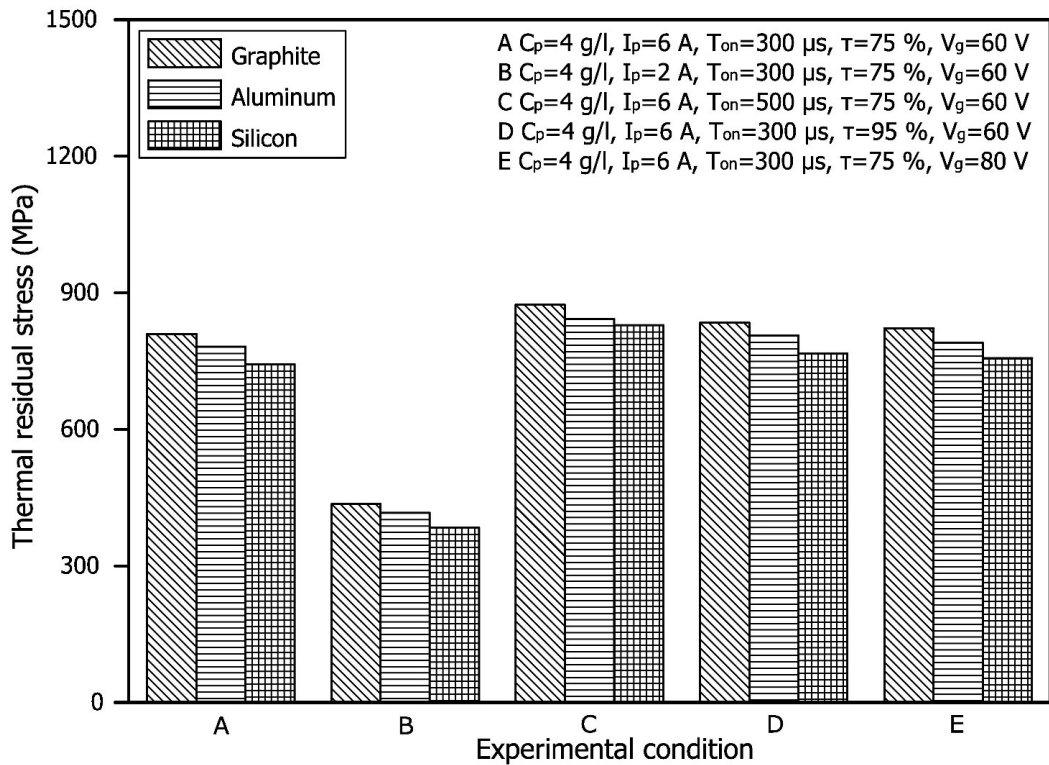
Fig. 4.7 Predicted thermal residual stress for different experimental conditions

The temperature distribution profiles obtained using FLUENT were transferred to STATIC STRUCTURAL module. Analyses were completed using the boundary conditions mentioned earlier. Fig. 4.7 shows the variation of average equivalent von-Mises stress generated on the workpiece due to heat energy associated with spark with respect to the change in process parameters.

It is observed that increase in process parameters such as peak current, pulse-on time, duty cycle and gap voltage led to the increase in thermal residual stress due to the raise in discharge heat energy. Among, the three powders, silicon has produced least thermal residual stress followed by aluminum and graphite due to its less thermal conductivity compared to other two.

4.2 Influence of powder materials and EDM parameters on material removal rate and radial overcut

4.2.1 Characterization of powder materials

As-received aluminum, graphite and silicon powders were characterized using various non-destructive testing methods such as scanning electron microscopy (SEM), particle size analysis, and X-ray diffraction to determine the actual size, distribution, and the presence of impurities. The results thus obtained were used to study the influence of powder size and impurities on various PMEDM characteristics of Inconel 625.

SEM micrographs of different powder additives are shown in Fig. 4.8. Although aluminum particles evidently have smoother surface compared to the other two, agglomeration of individual particles can also be noticed. Average size of the agglomerated particles is about ~15 µm, whereas the individual size might be less (3-6 µm), as observed from Fig. 4.8. On the other hand, graphite powder shows irregular shape with a mean size of ~20 µm. Silicon particles have sharp edges with irregular shape and correspond to an average size of ~10 µm.
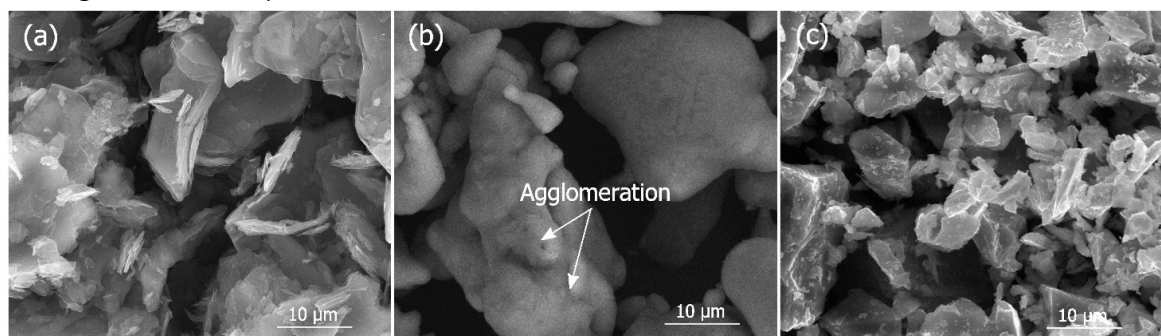
Fig. 4.8 Different powder additives (a) aluminum (b) graphite and (c) silicon used in PMEDM

The size distribution for different powders measured by a particle analyzer is shown in Fig. 4.9. Average size of graphite, silicon and aluminum particles comprising of maximum volume of sample size is ~12, ~16 and ~26 µm respectively. Evidently, graphite exhibits highest volume % of small particles followed by silicon and aluminum. On the other hand, aluminum indicated a small range of particle size distribution followed by silicon and graphite. One of the reasons for larger particle size measured for aluminum is the presence of extensive twinning and agglomeration in the samples [165]. In this case, particle size analyzer measured the agglomerations instead of particle size.
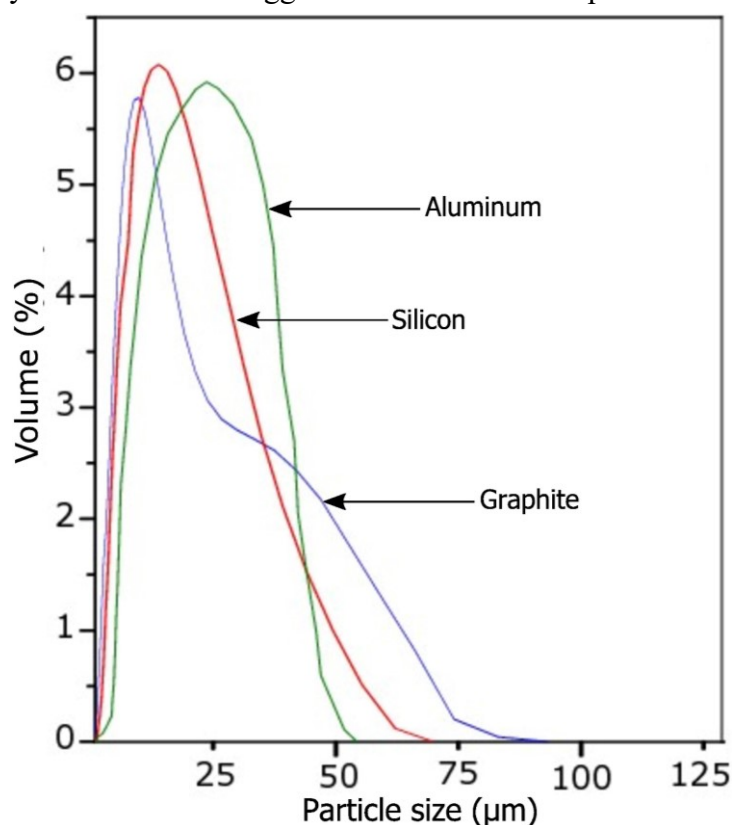
Fig. 4.9 Particle size distribution of different powders

X-ray diffraction (XRD) spectra of as-received powders are demonstrated in Fig. 4.10. Comparison with standard XRD patterns enabled an unambiguous identification of the phases present in all three powders. Presence of oxides i.e, Al_2O_3 and SiO_2 corresponding to (2 0 0), (2 2 0) phases were observed for aluminum and silicon powders respectively. No graphite oxide (GO) [166] phase could be found for graphite powder. From the XRD spectra, the average crystallite sizes of the as-received powders were calculated by using Scherrer's formula given in Eq. (4.2)

$$L = \frac{K\lambda}{\beta\cos\theta} \qquad\qquad (4.2)$$

where L is the mean crystallite size, K is the shape factor taken as 0.9, λ is the wavelength of the incident beam (1.54 A°), β is full width half maxima (FWHM) and θ is the Bragg angle. The average crystallite size of aluminum, graphite and silicon was found to be 20, 39 and 22 nm respectively. Apparent discrepancy in powder size might be explained by the fact that formation of particle takes place by combination of several crystallites. It may be noted that during PMEDM process it is the particle which actually contributes to alteration in electro-physical phenomena at the discharge gap. Therefore the size of the particle is of more relevance in the context of PMEDM process.
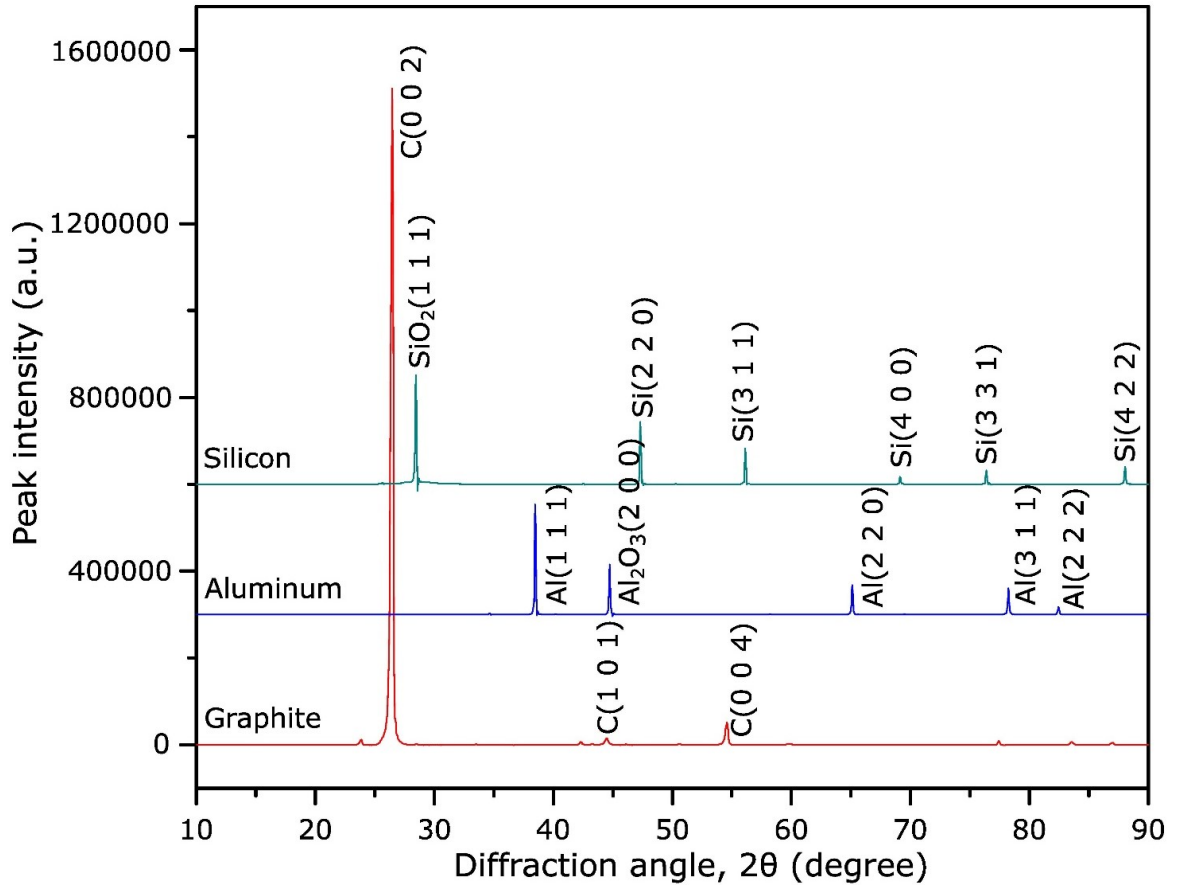
Fig. 4.10 XRD spectra of as-received powders

4.2.2 Material removal rate

For all the three powders, enhancement of MRR was observed when powder particles were uniformly dispersed in the dielectric. Such improvement in MRR can be attributed to the reduction of breakdown strength of the dielectric when conductive particles are added

to it. Gap between the two electrodes increases significantly in PMEDM compared to conventional EDM.

Table 4.1 MRR for different powders

Run	C_p (g/l)	I_p (A)	T_{on} (µs)	τ (%)	V_g (V)	MRR (mm^3/min)		
						Graphite	Aluminum	Silicon
1	0	6	300	75	60	5.529	5.529	5.529
2	2	4	400	85	70	0.644	0.686	0.625
3	2	8	200	85	70	12.745	13.568	12.374
4	2	8	400	85	50	10.473	11.149	10.168
5	2	4	200	85	50	3.735	3.976	3.626
6	2	8	400	65	70	5.197	5.533	5.046
7	2	4	400	65	50	0.52	0.554	0.505
8	2	8	200	65	50	12.759	13.582	12.387
9	2	4	200	65	70	2.715	3.015	2.478
10	4	6	300	75	60	5.638	5.638	5.299
11	4	6	100	75	60	8.01	8.638	7.529
12	4	10	300	75	60	21.304	23.104	20.025
13	4	6	300	75	40	7.219	7.723	6.786
14	4	6	300	75	80	3.934	4.215	3.698
15	4	6	300	75	60	5.683	5.683	5.342
16	4	6	300	75	60	6.168	6.168	5.798
17	4	6	300	55	60	4.744	5.103	4.459
18	4	6	300	95	60	7.19	7.683	6.758
19	4	6	300	75	60	6.542	6.542	6.149
20	4	6	300	75	60	7.023	7.023	6.602
21	4	6	300	75	60	6.814	6.814	6.405
22	4	6	500	75	60	1.048	1.619	0.985
23	4	2	300	75	60	0.293	0.36	0.275
24	6	8	400	65	50	11.049	11.878	10.089
25	6	8	400	85	70	11.98	12.874	10.938
26	6	4	200	65	50	3.691	3.968	3.37
27	6	4	200	85	70	3.163	3.706	3.148
28	6	8	200	85	50	19.05	20.479	17.393
29	6	8	200	65	70	12.301	11.664	11.183
30	6	4	400	65	70	0.484	0.52	0.442
31	6	4	400	85	50	0.768	0.825	0.701
32	8	6	300	75	60	10.254	6.505	8.726

The increase in gap causes enlarged discharge passages. At the same time, the powder particles try to bridge the discharge gap between both the electrodes. This facilitates the dispersion of discharge into several increments resulting in increase in sparking frequency and hence, MRR increases [108]. The measured MRR values for different powder-mixed dielectrics are provided in Table 4.1.
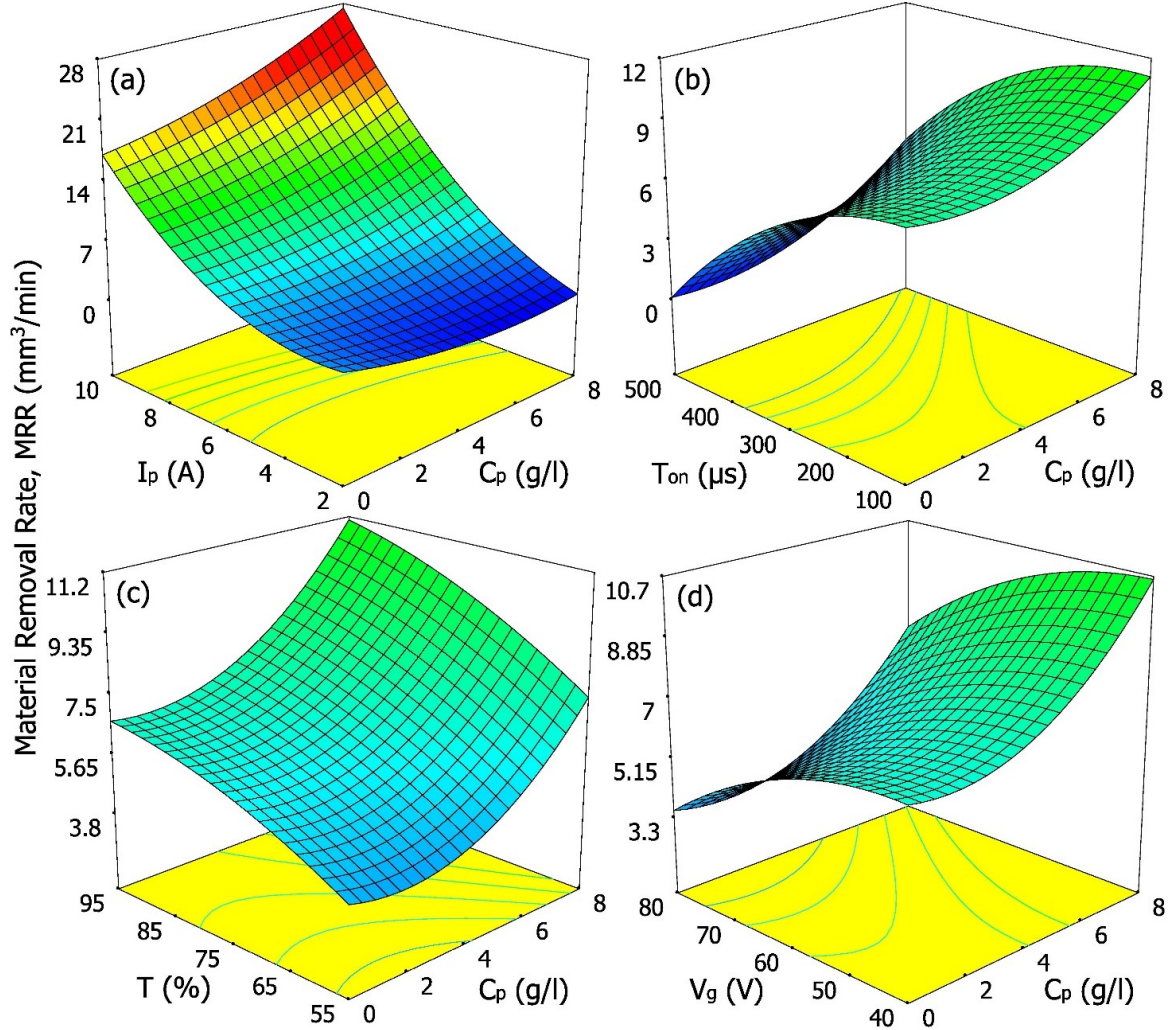
Fig. 4.11 Surface plots (a) C_p vs. I_p (b) C_p vs. T_{on} (c) C_p vs. τ and (d) C_p vs. V_g for MRR using graphite powder

Fig. 4.11, Fig. 4.12 and Fig. 4.13 show the effect of different powder materials and process parameters on MRR. Increase in peak current lead to the rise in MRR due to an increase in discharge energy. For low pulse-on time, the heating time of workpiece was so short that only a small part of material was melted, indicating a reduction in MRR. When pulse duration is prolonged, sufficient discharge energy in combination with better peak current density can be obtained. After the melted material is completely removed, a better

MRR is acquired, and highly efficient impulsive force is achieved. If pulse duration is too long, the plasma channel will be so much expanded that the density of electrical discharge energy may be reduced. Consequently, MRR declined.

With increase in duty cycle, spark energy per pulse increases leading to higher MRR. However, at higher duty cycle, accumulated debris and powder particles result in short circuiting leading to arcing and unstable discharge conditions. Thus, MRR decreased, due to unfavorable flushing conditions.
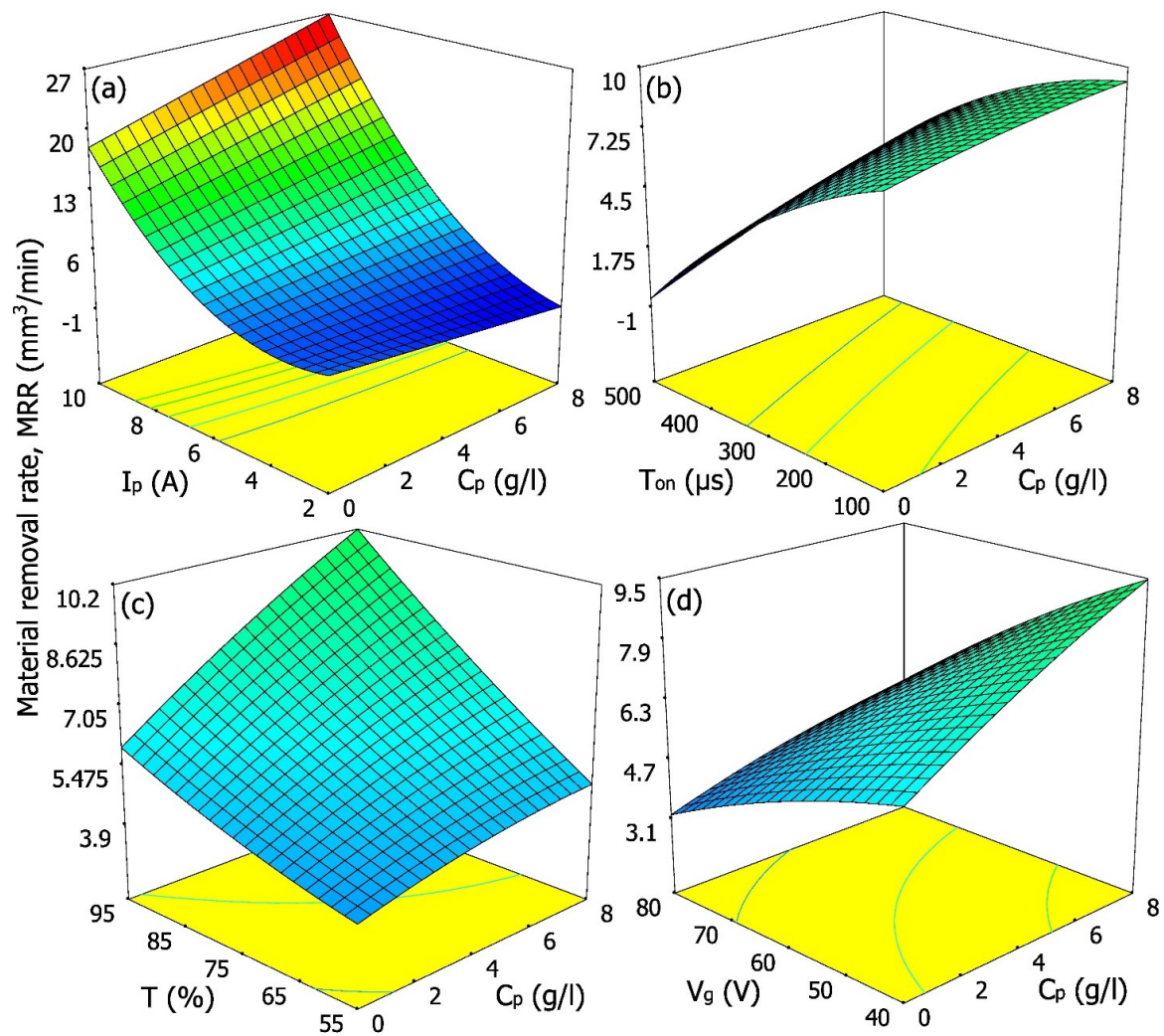
Fig. 4.12 Surface plots (a) C_p vs. I_p (b) C_p vs. T_{on} (c) C_p vs. τ and (d) C_p vs. V_g for MRR using aluminum powder

Keeping all other parameters constant, increased gap voltage causes a hike in energy per spark leading to higher MRR. However, at larger gap voltage, space between electrode and workpiece becomes larger. Hence, time required to fill the inter electrode gap with

neutral particles and ions is raised due the increase in gap voltage. Consequently a slight reduction in MRR was realized.
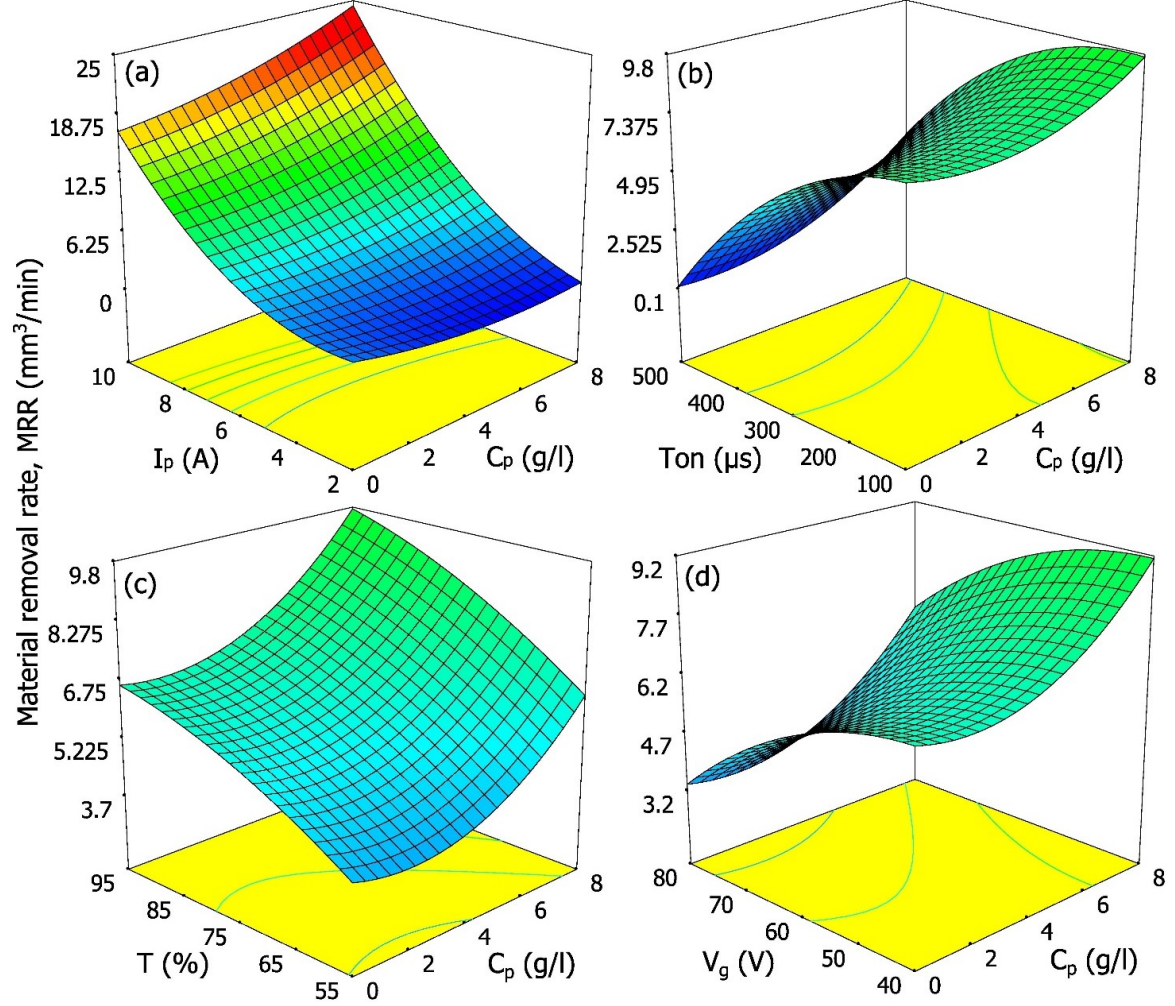
Fig. 4.13 Surface plots (a) C_p vs. I_p (b) C_p vs. T_{on} (c) C_p vs. τ and (d) C_p vs. V_g for MRR using silicon powder

Overall, aluminum powder produced the highest MRR followed by graphite and silicon up to 6 g/l concentration. This is due to the lower electrical resistivity of Al (2.89 μΩ-cm) powder compared to graphite (103 μΩ-cm) and Si (2325 μΩ-cm).

Lower electrical resistivity of Al allows the sparking to take place from a larger distance compared to other particles leading to a rise in sparking frequency. In addition, debris is easily and quickly flushed away due to the increased spark gap. Hence, highest MRR was achieved for aluminum powder in the low concentration range (up to 6 g/l). At higher concentrations, aluminum agglomerates (as seen in Fig. 4.8 and Fig. 4.9) and the large particles adhere to workpiece leading to short circuiting and arcing. On the other hand, low density of graphite (1.26 g/cc) compared to Al (2.70 g/cc) and Si (2.33 g/cc) allows it

to mix easily with the dielectric resulting in higher MRR at 8 g/l concentration. Si powder has the least electrical and thermal conductivities among the three powders. The presence of small amount of SiO$_2$ (Fig. 4.10) further reduces the electrical and thermal conductivities of Si powder. Hence, it had the least influence on MRR.

Analysis of variance (ANOVA) was conducted to test the significance of the model and lack of fit. If the probability (P) value is less than 0.05, it is statistically significant at 95 % confidence interval, but if it exceeds 0.1, it is not significant. Significant models and insignificant lack of fit are desirable. Quadratic model was selected for MRR to consider curvature effect. Table 4.2 illustrates the abridged ANOVA for MRR using three different powder-mixed dielectrics. P < 0.0001 for all three cases indicates that the models are significant. The insignificant lack of fit values of 0.8187, 0.3541 and 0.8355 for graphite, aluminum and silicon powders imply that the models fit well with the experimental data. The correlation coefficients for MRR using graphite, aluminum and silicon powder-mixed dielectrics are 99.53 %, 99.07 % and 99.25 % respectively. In addition, there are minor differences between Adj R^2 and Pred R^2. After deleting insignificant process parameters, RSM-based mathematical models for MRR using three different dielectrics have been obtained and shown in equations (4.3), (4.4) and (4.5).

Table 4.2 Abridged ANOVA for MRR

Source	Graphite	Aluminum	Silicon
Model	P < 0.0001	P < 0.0001	P < 0.0001
Lack of fit	P = 0.8187	P = 0.3541	P = 0.8355
Residual	0.47	0.93	0.47
R^2	0.9953	0.9907	0.9925
Adj R^2	0.9915	0.9849	0.9904
Pred R^2	0.9846	0.9681	0.9853

$$(MRR)_{Graphite} = 4.69 - 1.461*A - 1.942*B + 0.00934*C - 0.1477*D \qquad (4.3)$$
$$+ 0.268*E + 0.094*A^2 + 0.2757*B^2 - 0.000046*C^2 - 0.002029*E^2$$
$$+ 0.1987*A*B - 0.002271*B*C + 0.03763*B*D - 0.02937*B*E$$
$$+ 0.000238*C*E$$

$$(MRR)_{Al} = 16.85276 - 0.82184*A - 2.78309*B - 0.011298*C - 0.1773*D \qquad (4.4)$$
$$+ 0.036167*E + 0.19186*A*B - 0.000181*B*C + 0.044628*B*D$$
$$- 0.037653*B*E + 0.000329*C*E + 0.34633*B^2 - 0.000027*C^2$$

$$(MRR)_{Si} = 2.86 - 1.103*A - 1.566*B + 0.0094*C - 0.1284*D + 0.249*E \quad (4.5)$$
$$+ 0.0729*A^2 + 0.2618*B^2 - 0.000043*C^2 - 0.001798*E^2 + 0.1438*A*B$$
$$- 0.002108*B*C + 0.03395*B*D - 0.02808*B*E + 0.000199*C*E$$

From Table 4.3, Table 4.4 and Table 4.5 it is evident that the difference between experimental MRR and predicated MRR using regression modelling is minimum compared to those obtained using numerical modelling. This shows that fitted model equations give better results compared to numerical models under the given experimental conditions. Higher MRR was predicted using numerical modelling as there may be difference between assumed percentage of heat transfer to workpiece (20 %) and actual experimental heat transfer. And the flushing efficiency which was assumed to be 20 %, may even be less in actual experimental conditions.

Table 4.3 Comparison of experimental and predicted MRR for graphite mixed-dielectric

Experimental condition	Experimental MRR	Predicted MRR			
		Numerical modelling		Regression modelling	
		MRR	% error	MRR	% error
I_p=2 A, T_{on}=300 μs, τ=75 %, V_g=60 V	0.293	0.32	9.22	0.308	5.12
I_p=4 A, T_{on}=300 μs, τ=75 %, V_g=60 V	1.965	2.28	16.03	1.921	2.24
I_p=6 A, T_{on}=300 μs, τ=75 %, V_g=60 V	6.128	6.74	9.99	6.091	0.6
I_p=8 A, T_{on}=300 μs, τ=75 %, V_g=60 V	11.944	13.3	11.35	12.075	1.1
I_p=10 A, T_{on}=300 μs, τ=75 %, V_g=60 V	21.304	21.7	1.86	20.867	2.05
I_p=6 A, T_{on}=100 μs, τ=75 %, V_g=60 V	8.01	8.375	4.56	8.023	0.16
I_p=6 A, T_{on}=200 μs, τ=75 %, V_g=60 V	8.769	8.96	2.18	8.788	0.22
I_p=6 A, T_{on}=300 μs, τ=75 %, V_g=60 V	7.023	8.04	14.48	6.987	0.51
I_p=6 A, T_{on}=400 μs, τ=75 %, V_g=60 V	5.14	5.8	12.84	5.208	1.32
I_p=6 A, T_{on}=500 μs, τ=75 %, V_g=60 V	1.048	1.14	8.78	0.962	8.21
I_p=6 A, T_{on}=300 μs, τ=55 %, V_g=60 V	4.744	4.97	4.76	4.32	8.94
I_p=6 A, T_{on}=300 μs, τ=65 %, V_g=60 V	6.09	6.29	3.28	6.217	2.09
I_p=6 A, T_{on}=300 μs, τ=75 %, V_g=60 V	6.819	7.27	6.61	6.782	0.54
I_p=6 A, T_{on}=300 μs, τ=85 %, V_g=60 V	7.819	8.45	8.07	7.779	0.51
I_p=6 A, T_{on}=300 μs, τ=95 %, V_g=60 V	7.19	7.89	9.74	7.442	3.5
I_p=6 A, T_{on}=300 μs, τ=75 %, V_g=40 V	7.219	6.96	3.59	7.106	1.57
I_p=6 A, T_{on}=300 μs, τ=75 %, V_g=50 V	7.756	7.75	0.08	7.806	0.64
I_p=6 A, T_{on}=300 μs, τ=75 %, V_g=60 V	6.874	7.56	9.98	6.837	0.54
I_p=6 A, T_{on}=300 μs, τ=75 %, V_g=70 V	6.153	6.8	10.52	6.19	0.6
I_p=6 A, T_{on}=300 μs, τ=75 %, V_g=80 V	3.934	4.5	14.39	3.875	1.5

Table 4.4 Comparison of experimental and predicted MRR for aluminum mixed-dielectric

Experimental condition	Experimental MRR	Predicted MRR			
		Numerical modelling		Regression modelling	
		MRR	% error	MRR	% error
I_p=2 A, T_{on}=300 µs, τ=75 %, V_g=60 V	0.371	0.33	11.05	0.40	8.09
I_p=4 A, T_{on}=300 µs, τ=75 %, V_g=60 V	2.092	2.27	8.51	1.95	6.69
I_p=6 A, T_{on}=300 µs, τ=75 %, V_g=60 V	5.856	6.3	7.58	5.87	0.26
I_p=8 A, T_{on}=300 µs, τ=75 %, V_g=60 V	12.338	11.56	6.31	11.83	4.07
I_p=10 A, T_{on}=300 µs, τ=75 %, V_g=60 V	21.943	18.3	16.6	21.12	3.81
I_p=6 A, T_{on}=100 µs, τ=75 %, V_g=60 V	7.905	8.28	4.74	8.12	2.77
I_p=6 A, T_{on}=200 µs, τ=75 %, V_g=60 V	9.027	8.7	3.62	8.48	6.07
I_p=6 A, T_{on}=300 µs, τ=75 %, V_g=60 V	6.808	7.74	13.69	6.76	0.6
I_p=6 A, T_{on}=400 µs, τ=75 %, V_g=60 V	5.403	4.97	8.01	5.11	5.44
I_p=6 A, T_{on}=500 µs, τ=75 %, V_g=60 V	1.079	1.06	1.76	1.08	0.46
I_p=6 A, T_{on}=300 µs, τ=55 %, V_g=60 V	4.886	4.85	0.74	4.44	9.17
I_p=6 A, T_{on}=300 µs, τ=65 %, V_g=60 V	6.192	6.24	0.78	5.92	4.44
I_p=6 A, T_{on}=300 µs, τ=75 %, V_g=60 V	6.572	7.04	7.12	6.56	0.17
I_p=6 A, T_{on}=300 µs, τ=85 %, V_g=60 V	8.328	8.26	0.82	7.67	7.89
I_p=6 A, T_{on}=300 µs, τ=95 %, V_g=60 V	7.405	7.57	2.23	7.94	7.31
I_p=6 A, T_{on}=300 µs, τ=75 %, V_g=40 V	7.117	6.54	8.11	7.61	6.93
I_p=6 A, T_{on}=300 µs, τ=75 %, V_g=50 V	8.131	7.56	7.02	7.70	5.31
I_p=6 A, T_{on}=300 µs, τ=75 %, V_g=60 V	6.652	6.2	6.79	6.62	0.53
I_p=6 A, T_{on}=300 µs, τ=75 %, V_g=70 V	6.299	6.6	4.78	5.89	6.49
I_p=6 A, T_{on}=300 µs, τ=75 %, V_g=80 V	4.052	4.12	1.68	3.99	1.46

Table 4.5 Comparison of experimental and predicted MRR for silicon mixed-dielectric

Experimental condition	Experimental MRR	Predicted MRR			
		Numerical modelling		Regression modelling	
		MRR	% error	MRR	% error
I_p=2 A, T_{on}=300 µs, τ=75 %, V_g=60 V	0.27	0.24	11.11	0.28	5.09
I_p=4 A, T_{on}=300 µs, τ=75 %, V_g=60 V	1.86	1.93	3.76	1.79	3.6
I_p=6 A, T_{on}=300 µs, τ=75 %, V_g=60 V	5.72	6.12	6.99	5.7	0.33
I_p=8 A, T_{on}=300 µs, τ=75 %, V_g=60 V	11.19	10.5	6.17	11.31	1.01

I_p=10 A, T_{on}=300 µs, τ=75 %, V_g=60 V	20.02	17.97	10.24	19.62	2.02
I_p=6 A, T_{on}=100 µs, τ=75 %, V_g=60 V	7.52	8.07	7.31	7.58	0.8
I_p=6 A, T_{on}=200 µs, τ=75 %, V_g=60 V	8.22	8.55	4.01	8.24	0.19
I_p=6 A, T_{on}=300 µs, τ=75 %, V_g=60 V	6.50	6.06	6.77	6.54	0.62
I_p=6 A, T_{on}=400 µs, τ=75 %, V_g=60 V	4.81	4.54	5.61	4.86	1.02
I_p=6 A, T_{on}=500 µs, τ=75 %, V_g=60 V	0.98	1.02	4.08	0.93	5.18
I_p=6 A, T_{on}=300 µs, τ=55 %, V_g=60 V	4.45	4.53	1.8	4.057	9.02
I_p=6 A, T_{on}=300 µs, τ=65 %, V_g=60 V	5.68	5.81	2.29	5.79	1.95
I_p=6 A, T_{on}=300 µs, τ=75 %, V_g=60 V	6.36	6.77	6.45	6.34	0.31
I_p=6 A, T_{on}=300 µs, τ=85 %, V_g=60 V	7.37	7.51	1.9	7.30	0.91
I_p=6 A, T_{on}=300 µs, τ=95 %, V_g=60 V	6.75	7.55	11.85	7.06	4.6
I_p=6 A, T_{on}=300 µs, τ=75 %, V_g=40 V	6.78	6.35	6.34	6.71	1.09
I_p=6 A, T_{on}=300 µs, τ=75 %, V_g=50 V	7.28	7.08	2.75	7.31	0.41
I_p=6 A, T_{on}=300 µs, τ=75 %, V_g=60 V	6.42	6.06	5.61	6.4	0.31
I_p=6 A, T_{on}=300 µs, τ=75 %, V_g=70 V	5.78	6.41	10.9	5.79	0.26
I_p=6 A, T_{on}=300 µs, τ=75 %, V_g=80 V	3.69	3.75	1.63	3.68	0.46

4.2.3 Radial overcut

The addition of conductive powder particles to the dielectric drastically reduces its breakdown strength. The low break down strength allows the sparking to take place from a long distance [108]. Consequently, it results in increased radial overcut. The measured ROC values for different powder-mixed dielectrics are presented in Table 4.6.

Fig. 4.14, Fig. 4.15 and Fig. 4.16 demonstrate the influence of different powder materials and process parameters on radial overcut (ROC). ROC increased along with peak current and pulse-on time. This is due to high discharge energy removing large amount of molten material. There is no significant variation of ROC with respect to duty cycle and gap voltage. However, ROC slightly increased with duty cycle due to the increase in discharge energy. ROC declined at large duty cycle (95 %) due to the piling up of debris caused by the insufficient flushing. The effect is more evident for graphite and silicon mixed-dielectrics. Aluminum has the minimal influence due to agglomeration of particles at high concentration.

There was small increase in ROC with gap voltage due to increased discharge energy. However, at larger voltages, ROC appeared to decline slightly due to diminished MRR. Radial overcut significantly varies with properties of added particles. Silicon powder had least effect on ROC. The reasons are attributed to the thermo-physical characteristics of the

Si powder. Si has the highest electrical resistivity among the three powders. Therefore, among the three powder-suspended dielectrics, Si powder-suspended dielectric possesses the highest insulating strength. Al produced the largest ROC due to its high electrical conductivity.

Table 4.6 ROC for different powders

Run	C_p (g/l)	I_p (A)	T_{on} (μs)	τ (%)	V_g (V)	ROC (μm)		
						Graphite	Aluminum	Silicon
1	0	6	300	75	60	25.79	25.79	25.79
2	2	4	400	85	70	34.38	61.88	20.63
3	2	8	200	85	70	36.9	66.43	22.14
4	2	8	400	85	50	45.13	92.82	30.94
5	2	4	200	85	50	53.14	95.66	31.89
6	2	8	400	65	70	78.3	140.95	46.98
7	2	4	400	65	50	38.2	68.75	22.92
8	2	8	200	65	50	44.29	79.71	26.57
9	2	4	200	65	70	29.52	53.14	17.71
10	4	6	300	75	60	51.71	112.07	31.02
11	4	6	100	75	60	41.7	85.06	25.02
12	4	10	300	75	60	56.71	113.08	34.03
13	4	6	300	75	40	48.37	91.07	29.02
14	4	6	300	75	80	48.5	91.03	29.1
15	4	6	300	75	60	53.38	112.08	32.03
16	4	6	300	75	60	52.77	111.99	31.66
17	4	6	300	55	60	46.37	83.06	26.02
18	4	6	300	95	60	52.99	99.67	30.22
19	4	6	300	75	60	45.04	111.96	30.32
20	4	6	300	75	60	51.71	112.07	31.02
21	4	6	300	75	60	51.71	111.17	31.02
22	4	6	500	75	60	53.38	106.08	32.03
23	4	2	300	75	60	35.03	68.05	21.02
24	6	8	400	65	50	58.67	116.17	35.2
25	6	8	400	85	70	83.12	158	47.88
26	6	4	200	65	50	52.91	104.75	31.74
27	6	4	200	85	70	60.46	119.72	36.28
28	6	8	200	85	50	43.46	86.05	26.08
29	6	8	200	65	70	47.24	93.53	28.34
30	6	4	400	65	70	26.89	53.24	16.13
31	6	4	400	85	50	51.34	101.65	30.8
32	8	6	300	75	60	54.04	89.28	32.43
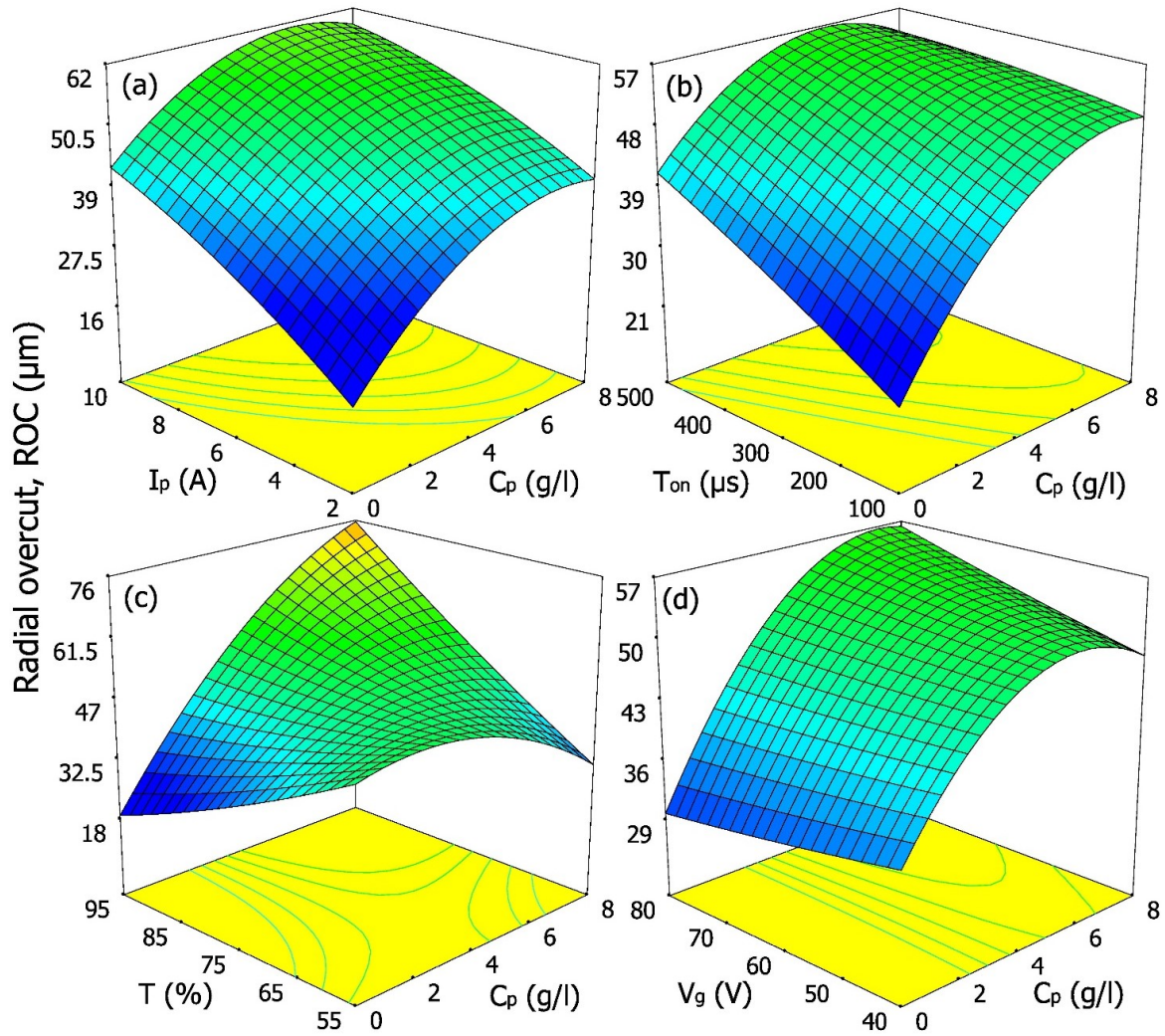
Fig. 4.14 Surface plots (a) C_p vs. I_p (b) C_p vs. T_{on} (c) C_p vs. τ and (d) C_p vs. V_g for ROC using graphite powder

ROC increased with increase in powder concentration. The presence of conductive or semi-conductive powders in the working gap can drastically lowers the breakdown strength of dielectric, eventually leading to a higher spark gap.

Table 4.7 illustrates the ANOVA for ROC using three different powder-mixed dielectrics. P < 0.0001 for all three cases indicate that the models are significant. The insignificant lack of fit values of 0.4027, 0.1523 and 0.3290 for graphite, aluminum and silicon powders indicate that the models fit well with the experimental data. The correlation coefficients for ROC using graphite, aluminum and silicon powder-mixed dielectrics are 95. 38 %, 91.42 % and 98.43 % respectively exhibit a good agreement between measured and predicted values. In addition, there are minor differences between Adj R^2 and Pred R^2.

After deleting insignificant process parameters, RSM-based mathematical models for ROC using three different dielectrics are expressed in equations (4.6), (4.7) and (4.8).
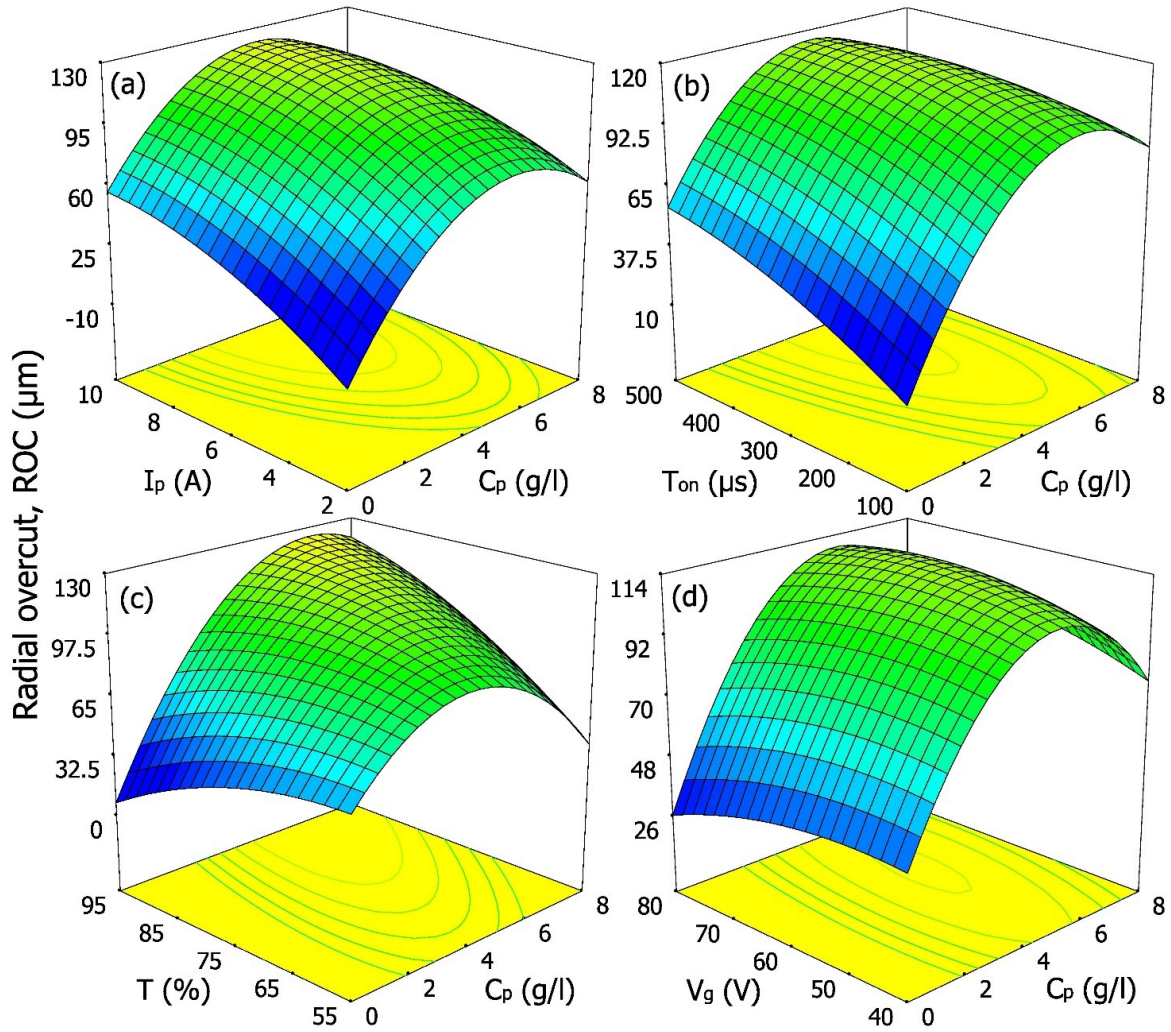
Fig. 4.15 Surface plots (a) C_p vs. I_p (b) C_p vs. T_{on} (c) C_p vs. τ and (d) C_p vs. V_g for ROC using aluminum powder

Table 4.7 Abridged ANOVA for ROC

Source	Graphite	Aluminum	Silicon
Model	P < 0.0001	P < 0.0001	P < 0.0001
Lack of fit	P = 0.4027	P = 0.1523	P = 0.3290
Residual	11.37	9.29	1.49
R^2	0.9538	0.9142	0.9843
Adj R^2	0.9247	0.8670	0.9676
Pred R^2	0.8264	0.7767	0.9353
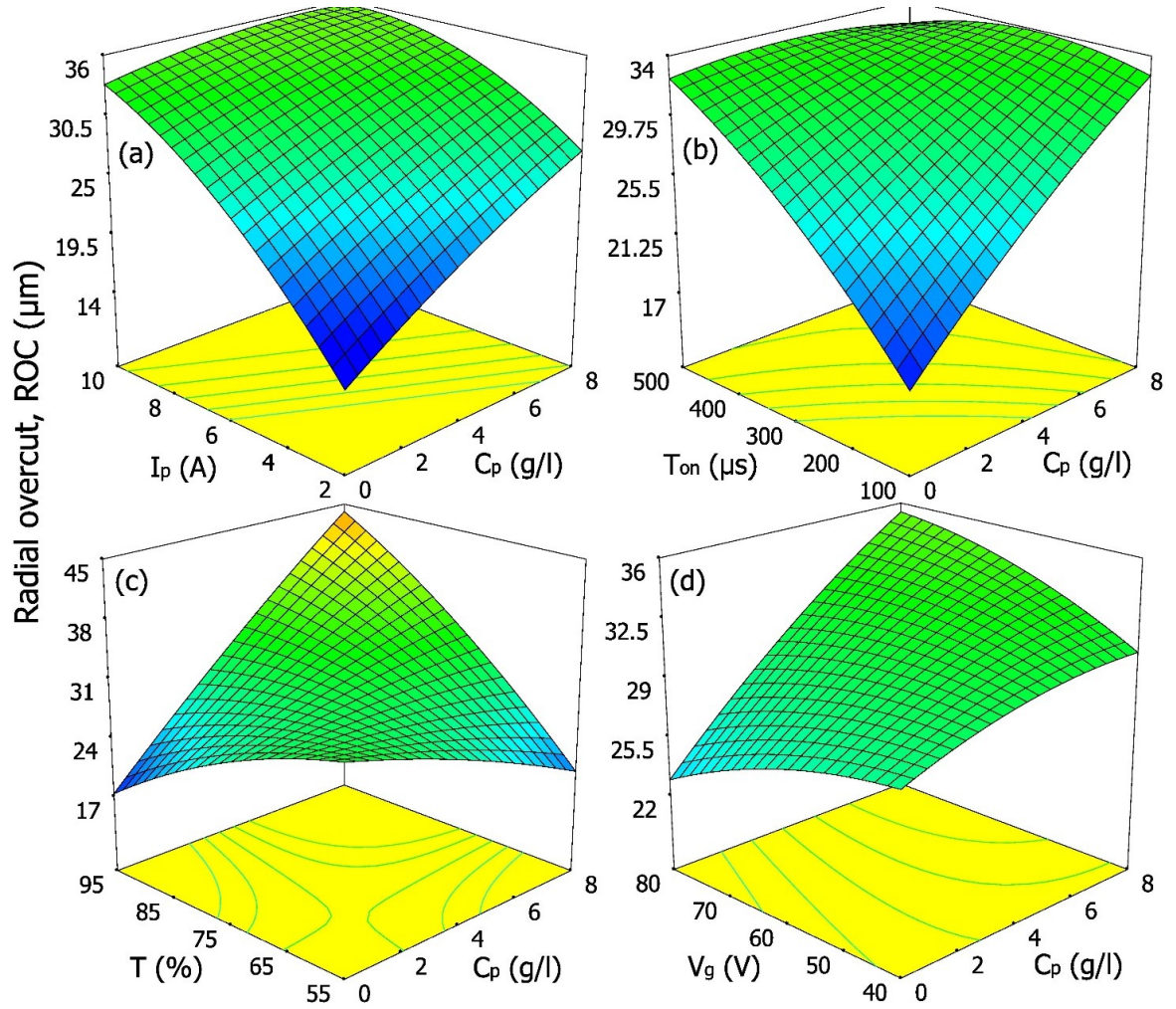
Fig. 4.16 Surface plots (a) C_p vs. I_p (b) C_p vs. T_{on} (c) C_p vs. τ and (d) C_p vs. V_g for ROC using silicon powder

$$(ROC)_{Graphite} = 230.5 - 2.1*A - 21.5*B - 0.4493*C + 1.259*D - 3.126*E \qquad (4.6)$$
$$- 2.577*A^2 + 0.386*A*D + 0.0844\,B*C - 0.394*B*D + 0.522*B*E$$

$$(ROC)_{Al} = 124.3 - 7.33*A - 4.26*B - 0.2096*C + 0.468*D - 2.238*E \qquad (4.7)$$
$$- 0.1362*B^2 - 0.00396*D^2 - 0.1708*A*B - 0.00487*A*C$$
$$+ 0.1194*A*D + 0.0302*A*E + 0.02657*B*C - 0.1286*B*D$$
$$+ 0.1661\,B*E + 0.001473*C*E + 0.00906*D*E$$

$$(ROC)_{Si} = 42.39 - 1.513*A - 1.692*B - 0.05913*C - 0.0939*D \qquad (4.8)$$
$$- 0.616*E - 0.0733*A^2 + 0.03278*A*D + 0006185\,*B*C - 0.032*B*D$$
$$+ 0.04391*B*E + 0.000438*C*E + 0.00303*D*E$$

65

4.3 Influence of powder materials and EDM parameters on surface integrity

4.3.1 Crater distribution
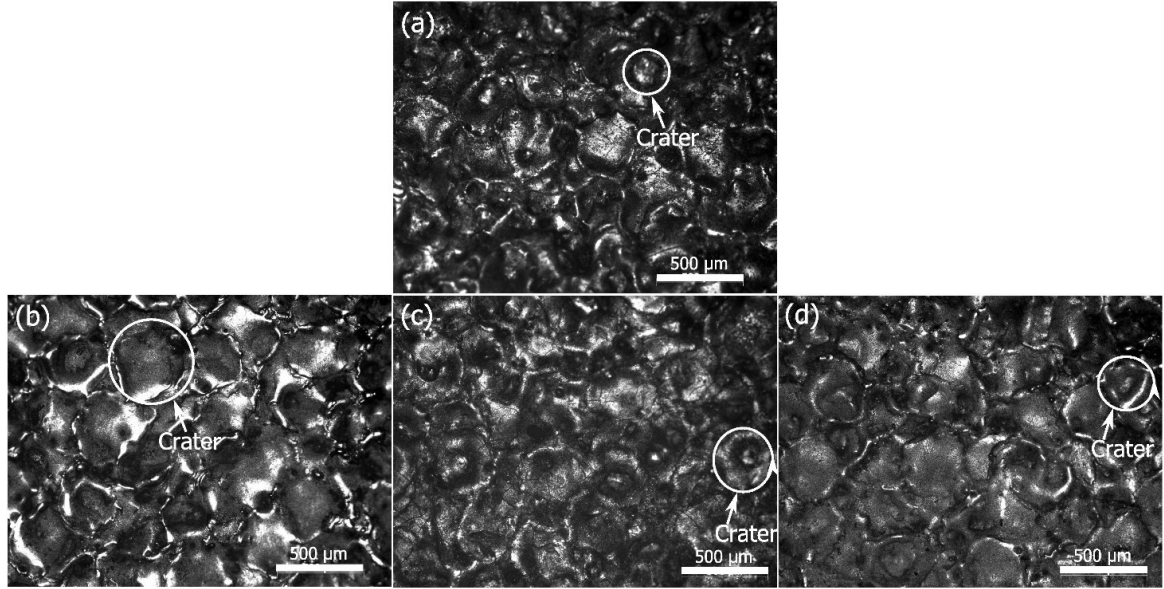
Fig. 4.17 Distribution of craters using (a) no powder (b) graphite (c) aluminum and (d) silicon powders for C_p= 4 g/l, I_p= 6 A, T_{on}= 300 μs, τ= 75 % and V_g= 60 V
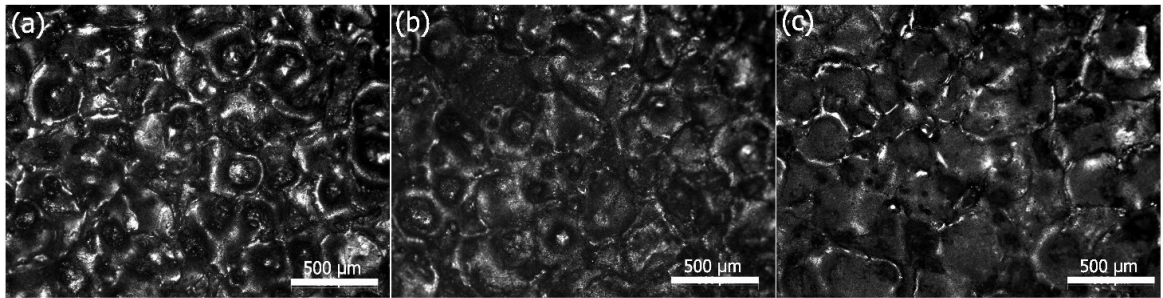
Fig. 4.18 Distribution of craters using (a) Graphite (b) Aluminum and (c) Silicon powders for C_p= 8 g/l, I_p= 6 A, T_{on}= 300 μs, τ= 75 % and V_g= 60 V

Microscopic images in Fig. 4.17 show the crater depth and size of the machined surface using different powder-mixed dielectrics. Deep and small craters were observed on the surface machined by conventional EDM (Fig. 4.17(a)). For all the three powder-mixed dielectrics, larger and shallower craters were observed compared to conevential EDM ('A' and 'B' of Fig. 4.23). This is due to enhanced conductivity which causes spark

generation from a long distance. Enlarged IEG allows the expansion of plasma channel width.

Simultaneously, external hydrostatic force acting on the plasma channel decreases. Thus, large and shallow cavities are formed on the workpiece since discharge energy spreads over a larger area. Among the three powders, graphite produced largest cavities due to the combination of its low density, high electrical and thermal conductivities. It is followded by aluminum and silicon. However, the difference in crater size among the threee powder-mixed dielectrics is very small.
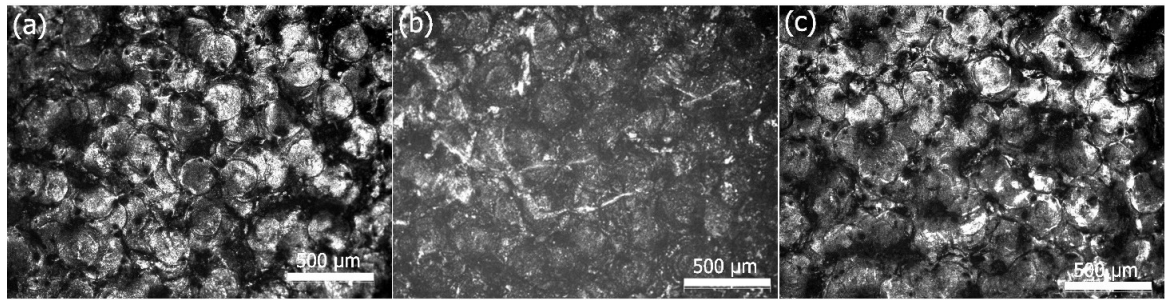
Fig. 4.19 Distribution of craters using (a) graphite (b) aluminum and (c) silicon powders for C_p= 4 g/l, I_p= 2 A, T_{on}= 300 µs, τ= 75 % and V_g= 60 V

Crater size and depth increased at high powder concentration (8 g/l) compared to low powder concentration (4 g/l) as shown in Fig. 4.18. This is due to the increased spark gap allowing the plasma channel expansion with powder addition.

Fig. 4.19 shows the crater distribution at a peak current of 2 A. The craters are small, flat and distintinctly visible. It is due to the small amount of discharge energy associated with low peak current.
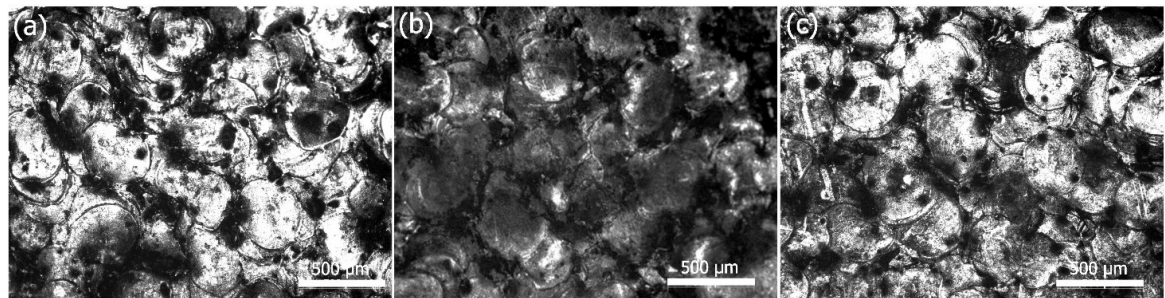
Fig. 4.20 Distribution of craters using (a) graphite (c) aluminum and (c) silicon powders for C_p= 4 g/l, I_p= 6 A, T_{on}= 500 µs, τ= 75 % and V_g= 60 V

Large, flat and distinct craters were observed at a pulse-on time of 500 µs as shown in Fig. 4.20. Larger craters are due to the expansion of plasma channel with pulse-on time. Reduction of plasma channel pressure also allows the molten material to flow over a large area.
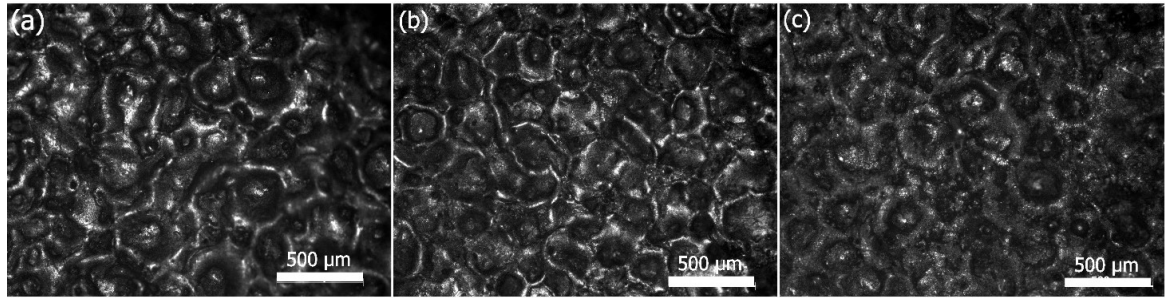
Fig. 4.21 Distribution of craters using (a) graphite (c) aluminum and (c) silicon powders for C_p= 4 g/l, I_p= 6 A, T_{on}= 300 µs, τ= 95 % and V_g= 60 V
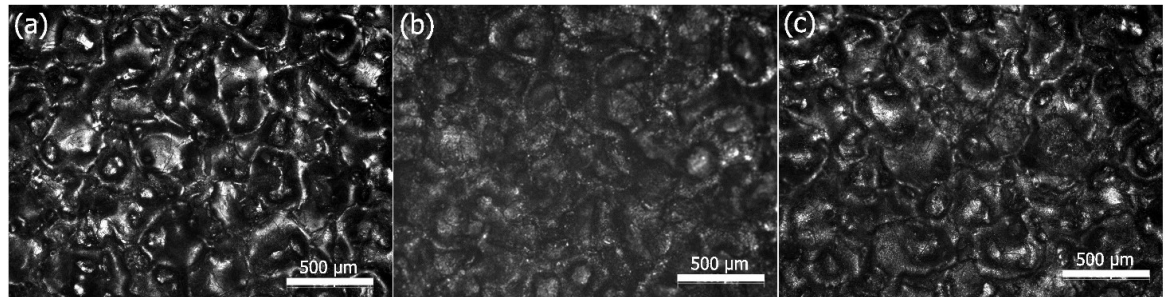
Fig. 4.22 Distribution of craters using (a) graphite (c) aluminum and (c) silicon powders for C_p= 4 g/l, I_p= 6 A, T_{on}= 300 µs, τ= 75 % and V_g= 80 V

Crater size increased slightly with the increase in duty cycle as shown in Fig. 4.21. This may be due to the flow of molten metal at the crater edges as the time available for debris removal is very short. Craters also appeared to be deep due to bulging of molten metal at the crater edges because of insufficient cooling time.

Crater diameter slightly increased with gap voltage due to enlargement of the IEG at higher voltages. Comparitively shallow craters were obtained as shown in Fig. 4.22 due to the decreased plasma channel pressure on the moltan metal.

The avregae crater diameter for different powder materials, their concentartion and maching conditions is shown in Fig. 4.23.
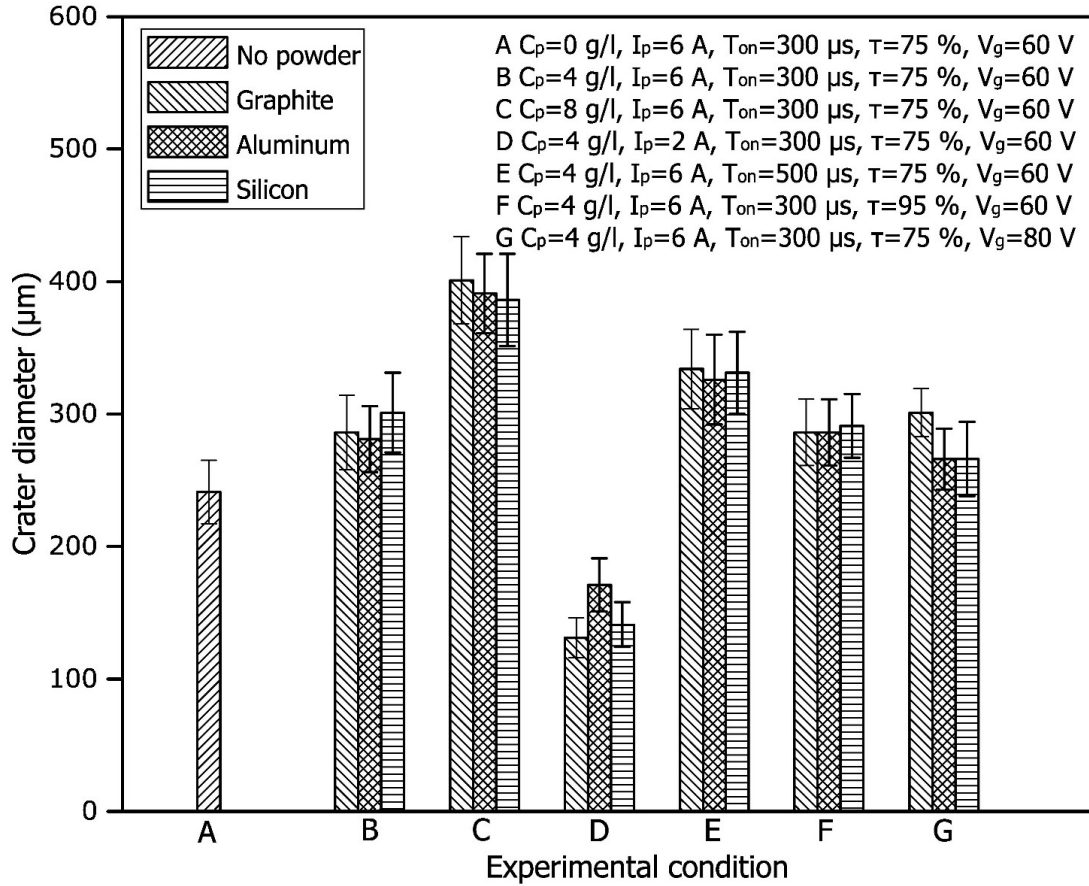
Fig. 4.23 Variation of crater diameter with different machining conditions

4.3.2 Surface topography

EDM surface is characterized by overlapping craters, globules of debris, uneven fusing structure, pockmarks and cracks. These defects are depiected in Fig. 4.24 which includes various SEM images of the machined surfaces using both pure dielectric (without powder) and different powder-suspended dielectric at 4 g/l concentration. Among others, cracking is one of the significant surface defects since it causes deterioration in resistance to fatigue and corrosion of the material especially under tensile loading condition. There are two types of cracks in EDM. Circumferential cracks orginate from the edge of the crater, while penetrating cracks go deep in to the sub-surface layers and even base material. Ekmekci and Ersöz [167] demonstrated the mechanism of formation such cracks.

It is evident from Fig. 4.24 that the surface obtained using conventional EDM seems to consist of more number of surface defects (surface cracks in particular) along with deep craters. PMEDM did not only minimize number of surface defects, but also left shallow craters.
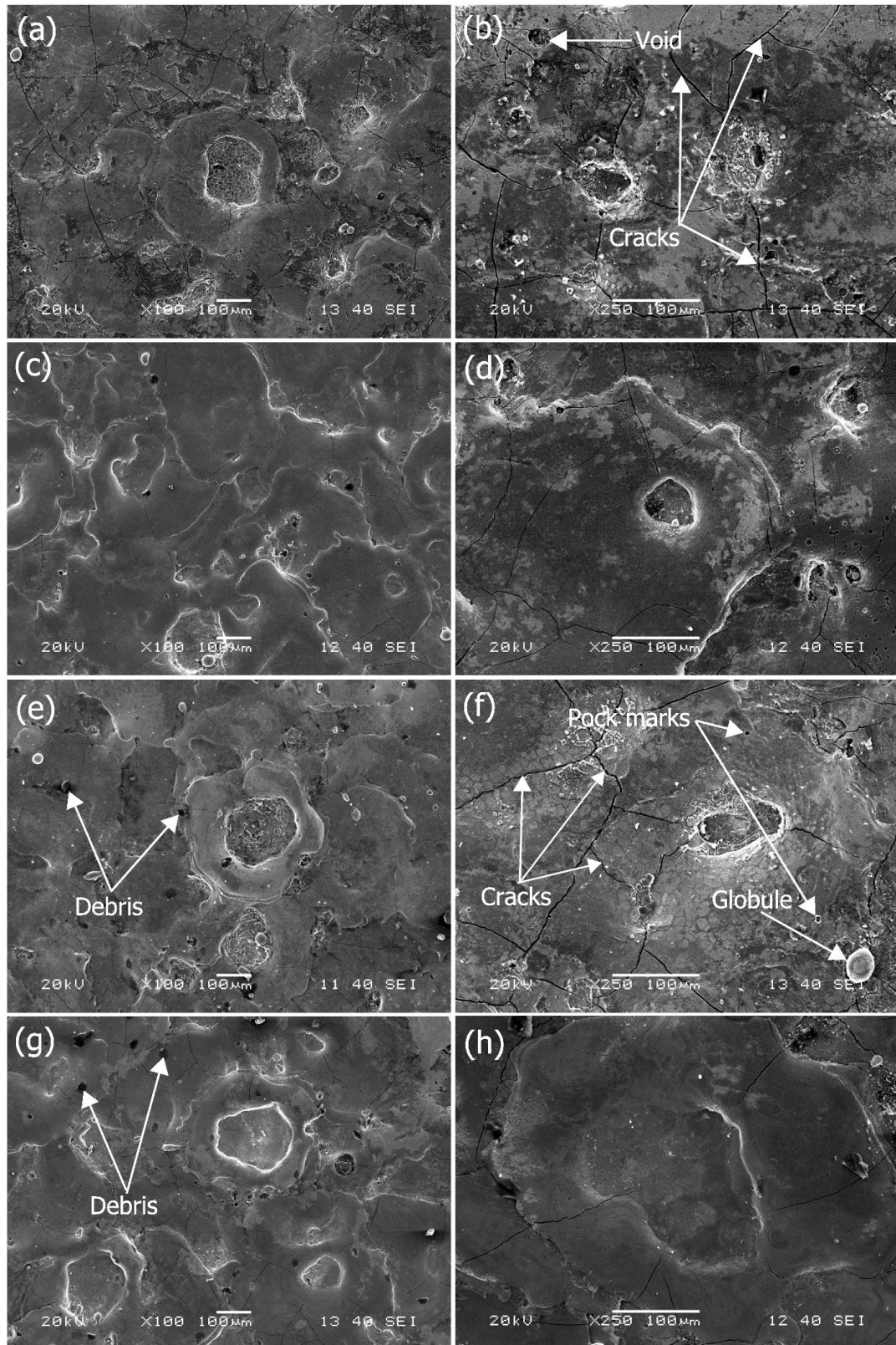
Fig. 4.24 Surface morphology using (a, b) no powder (c, d) graphite (e, f) aluminum and (g, f) silicon powders for C_p= 4 g/l, I_p= 6 A, T_{on}= 300 μs, τ= 75 % and V_g= 40 V
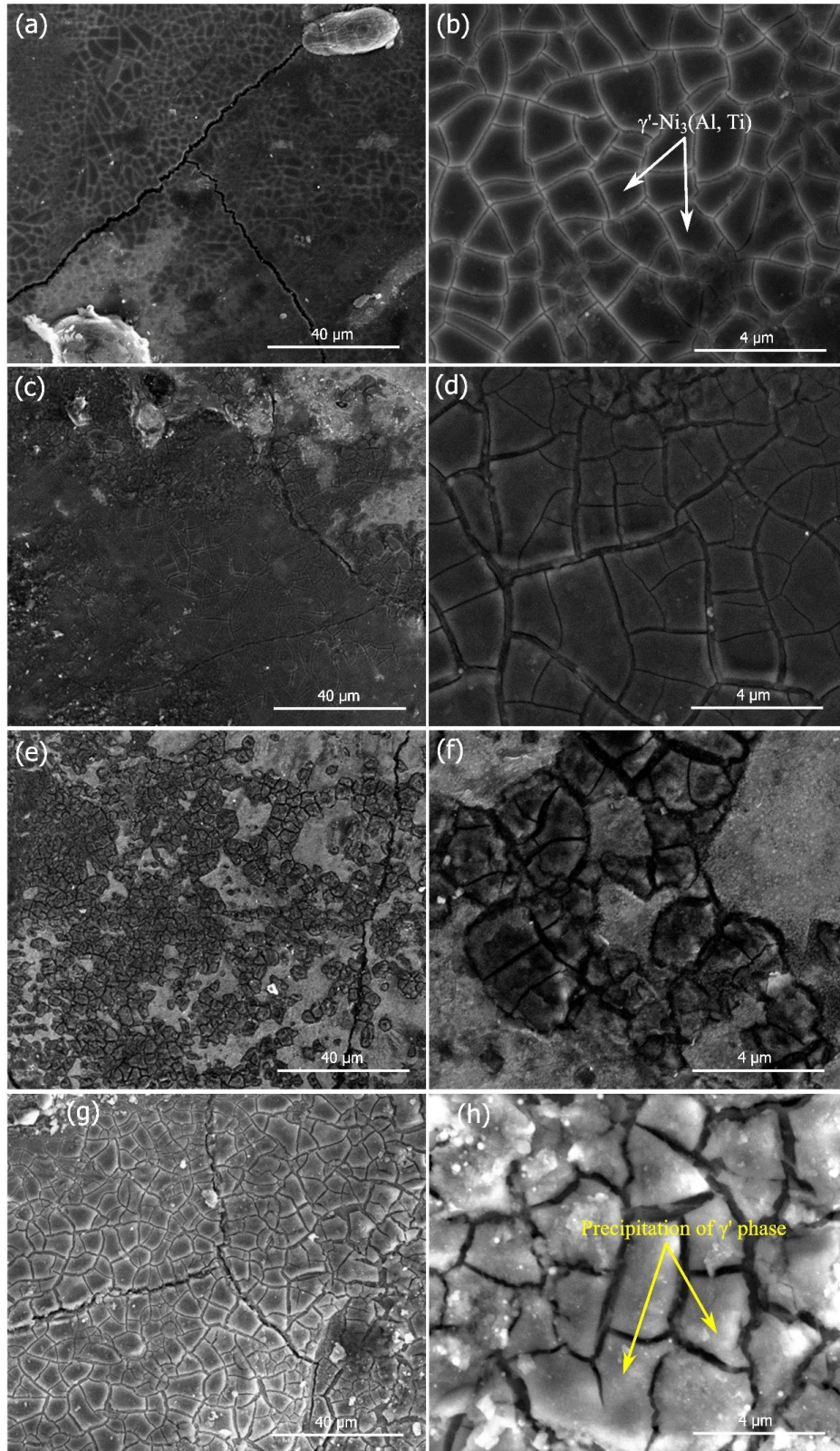
Fig. 4.25 Micromorphology of the machined surfaces using (a, b) no powder (c, d) graphite (e, f) aluminum and (g, h) silicon powders for C_p= 4 g/l, I_p= 6 A, T_{on}= 300 μs, τ= 75 % and V_g= 40 V

In PMEDM, high thermal conductivity of the added powder takes away some part of residual heat from the sparking zone. Uniform energy distribution, slow cooling rate of the molten metal due to less plasma channel pressure also reduce the formation of micro-cracks [21]. Among the different powders, surface generated with graphite mixed EDM exibited smothest morphology. Capability of graphite to tackle surface damage compared to other two powders may be explained by very high heat of fusion coupled with high thermal conductivity (Table 3.3) and consequent restriction of thermal energy transferred to the workpiece surface. It is also evident from Fig. 4.24(g, h) that silicon powder also resulted in shallow crater and less surface damage also due to considerably high heat of fusion (around 4 times that of aluminum).

Careful investigation of the higher magnification images i.e. Fig. 4.24(b), (d), (f) and (h) would reveal that all surface cracks primarily nucleate from the ridges of the crater and extend along the machined surface. This phenomenon might be attributed to high transformational stresses evolved during melting and resolidification processes.

Since heat flux could be more uniformly distributed all over the machined surface due to mixing of the powders with the dielectric, such stress could be minimized and hence severity of surface cracking was mitigated in comparison with EDM using pure dielectric. Minimum surface cracking could be observed with graphite powder as its high thermal conductivity helps in uniform distribution and dissipation of heat to the workpiece surfaces to limit the number of craters produced.

Another feature that may have an impact on the performance of graphite is its excellent lubricity, which may have some effects in terms of wetting of the particles by the melted surface [37]. It is followed by Si-suspended dielectric due to high heat of fusion. Al powder-suspended dielectric resulted in more severe thermal cracking owing to very less heat of fusion. Higher magnification images revealed the solidified globules of molten metal and pockmarks on the surface machined using conventional EDM. Smooth surface with very little amount of resolidified molten metal was observed for Si powder-mixed dielectric due to the combination of small particle size and abrasive action.

The study reveals interesting microstructure of Inconel 625 after EDM and PMEDM processes. Comparing the microstructures depicted in Fig. 4.25 with that of as-received Inconel 625, it becomes evident that precipitation of γ' phases from matrix of γ phase (austenitic) is promoted due to EDM process as a result of heating and cooling cycles [168]. This precipitated γ' phase is an intermetallic phase consisting mainly of $Ni_3(Al\ Ti)$ and one of the major contributors for precipitation hardening of Inconel 625 [169]. This γ' phase hinders dislocation movement and hence improves creep resistance of the alloy. When the

same phase is present in more volume fraction, it augments the strength of the material owing to its ordered structure and high degree of coherency with γ phase [170].
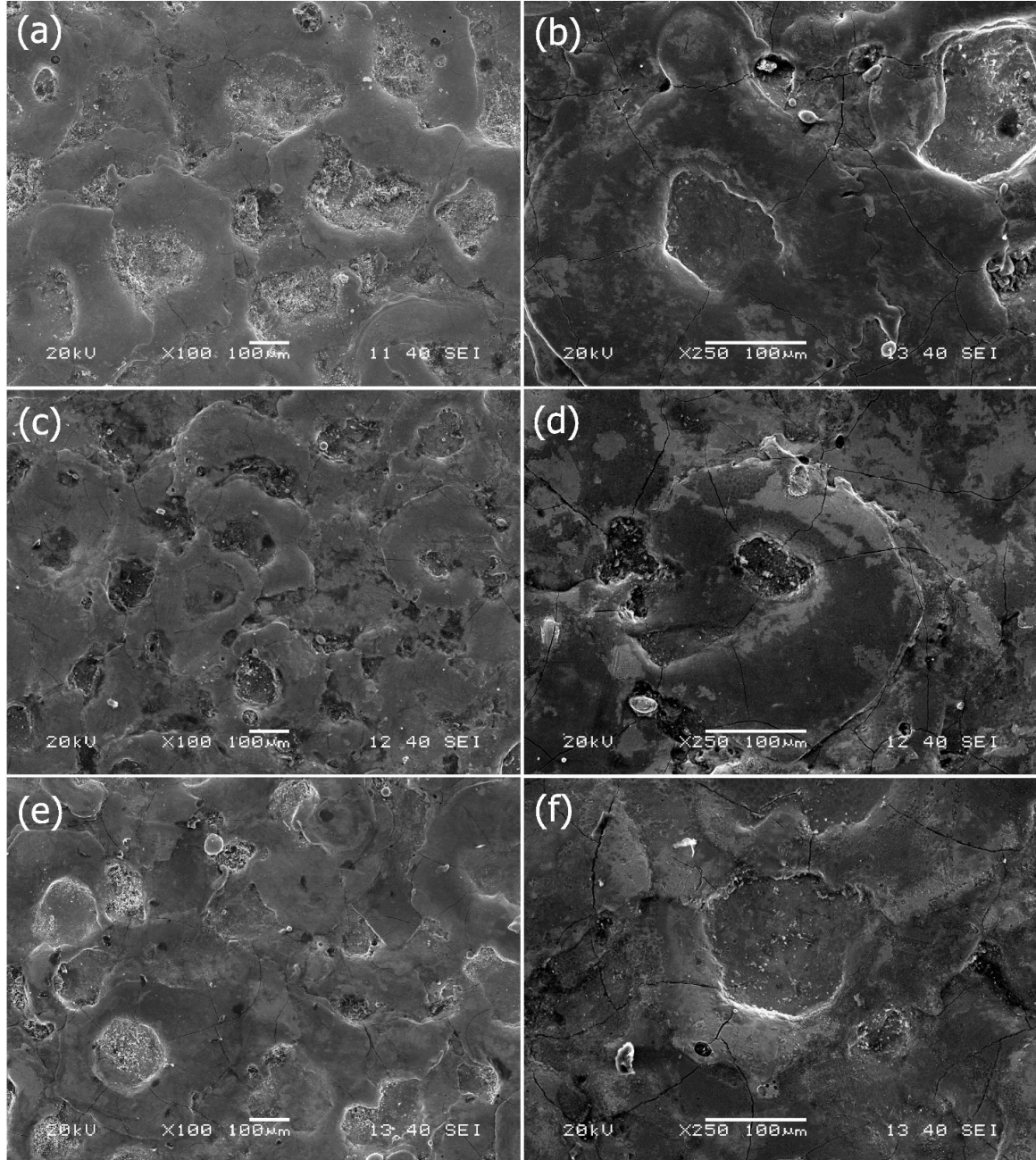
Fig. 4.26 Surface morphology using (a, b) graphite (c, d) aluminum and (e, f) silicon powders for C_p= 8 g/l, I_p= 6 A, T_{on}= 300 μs, τ= 75 % and V_g= 40 V

Careful consideration of Fig. 4.25 would indicate that such structure existed only in discrete domains, not uniformly distributed at the entire machined surface. Moreover, prominent γ' phase was detected after EDM with pure dielectric as well that mixed with

different powders, although their appearance looks different. Moreover, availability of more carbon atoms due to pyrolysis of kerosene dielectric leads to rise in metal carbides of the form $M_{23}C_6$ or MC precipitated in the grain boundaries. As a consequence of both these phenomena, hardness of the machined workpiece is expected to increase.
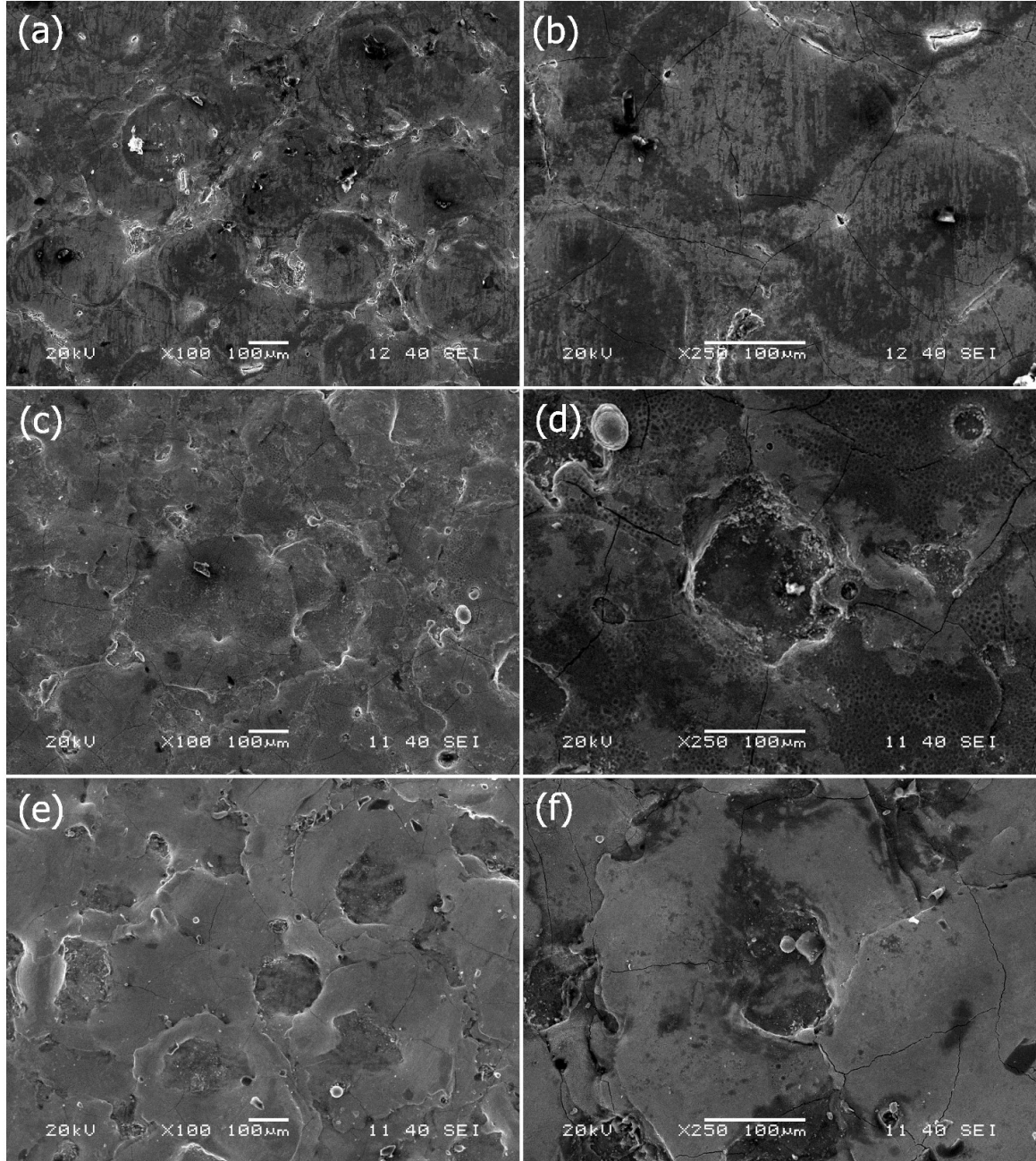
Fig. 4.27 Surface morphology using (a, b) graphite (c, d) aluminum and (e, f) silicon powders for C_p= 4 g/l, I_p= 2 A, T_{on}= 300 µs, τ= 75 % and V_g= 40 V

At a high powder concentration of 8 g/l, the amount of pock marks and globules on the surface increased as shown in Fig. 4.26 due to the availability of higher discharge energy.
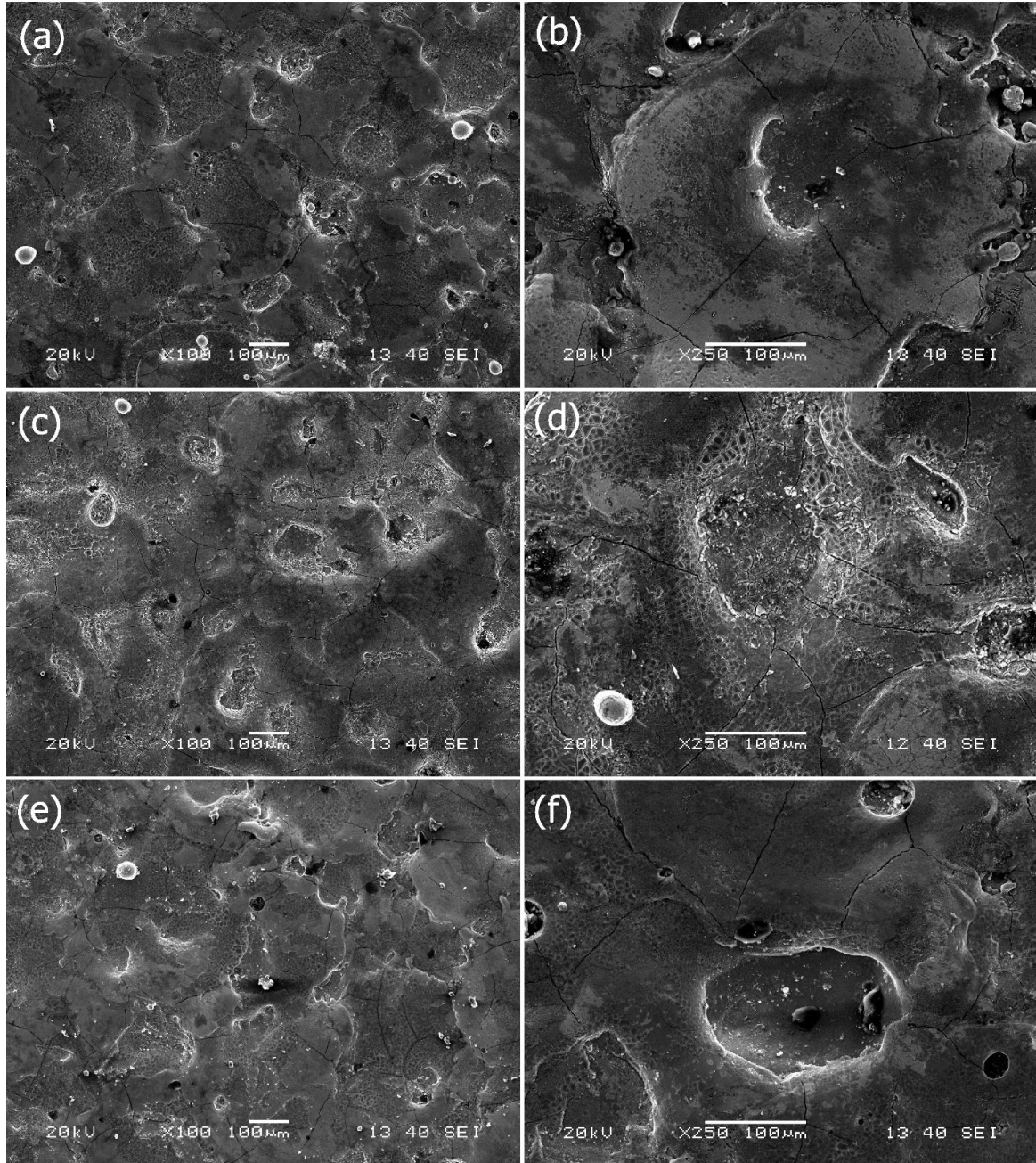
Fig. 4.28 Surface morphology using (a, b) graphite (c, d) aluminum and (e, f) silicon powders for C_p= 4 g/l, I_p= 6 A, T_{on}= 500 μs, τ= 75 % and V_g= 40 V

It was observed from Fig. 4.27 that at low peak current the craters were shallow and the density of global appendages and pockmarks was low, whereas at higher peak current, the craters were deeper and global appendages were most evident.
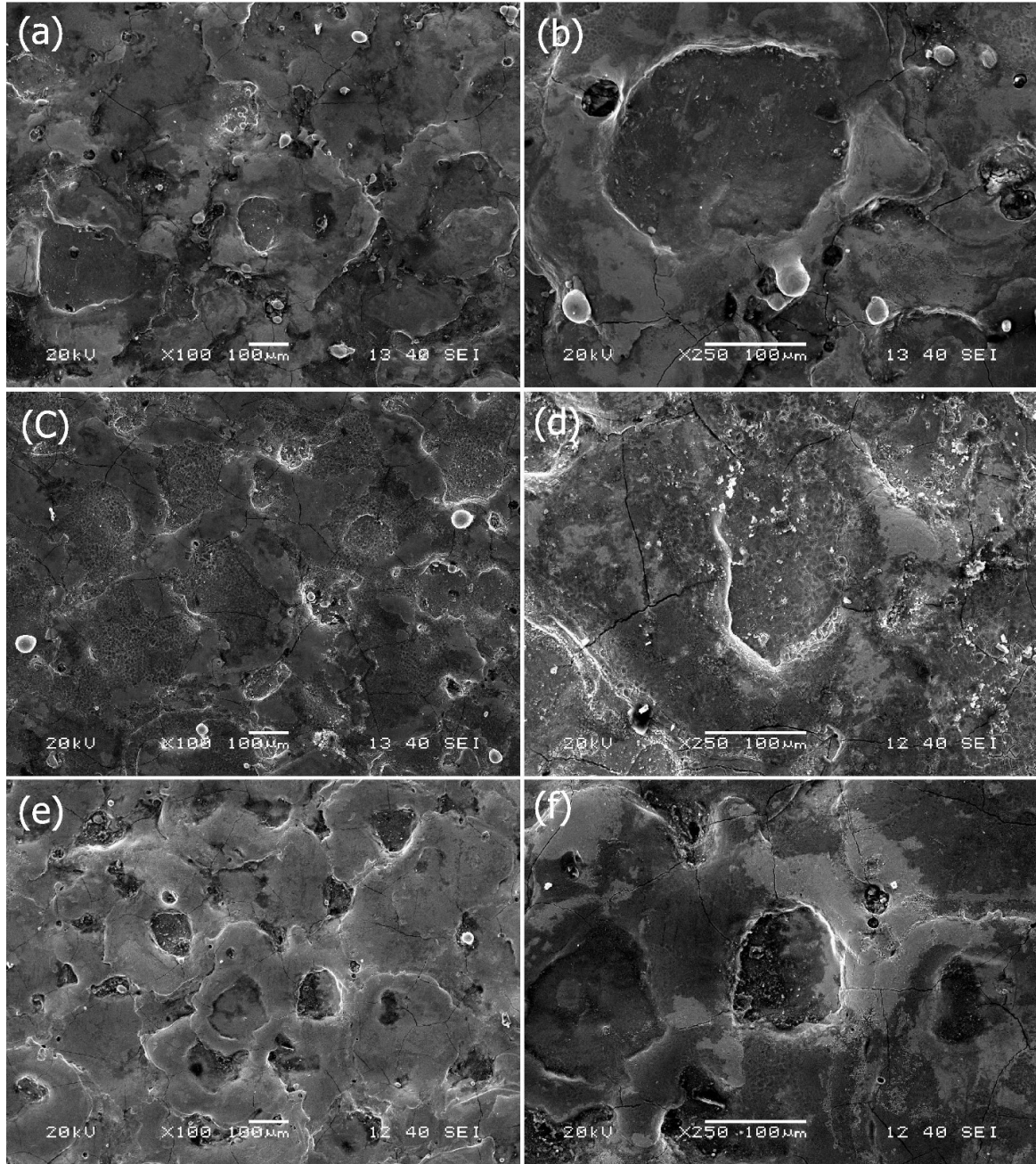
Fig. 4.29 Surface morphology using (a, b) graphite (c, d) aluminum and (e, f) silicon powders for C_p= 4 g/l, I_p= 6 A, T_{on}= 300 μs, τ= 95 % and V_g= 40 V

The effect of increased pulse-on time on the surface structure is evident from Fig. 4.28. The amount and size of the pockmarks were increased due to the availability of extended duration of heat transfer.
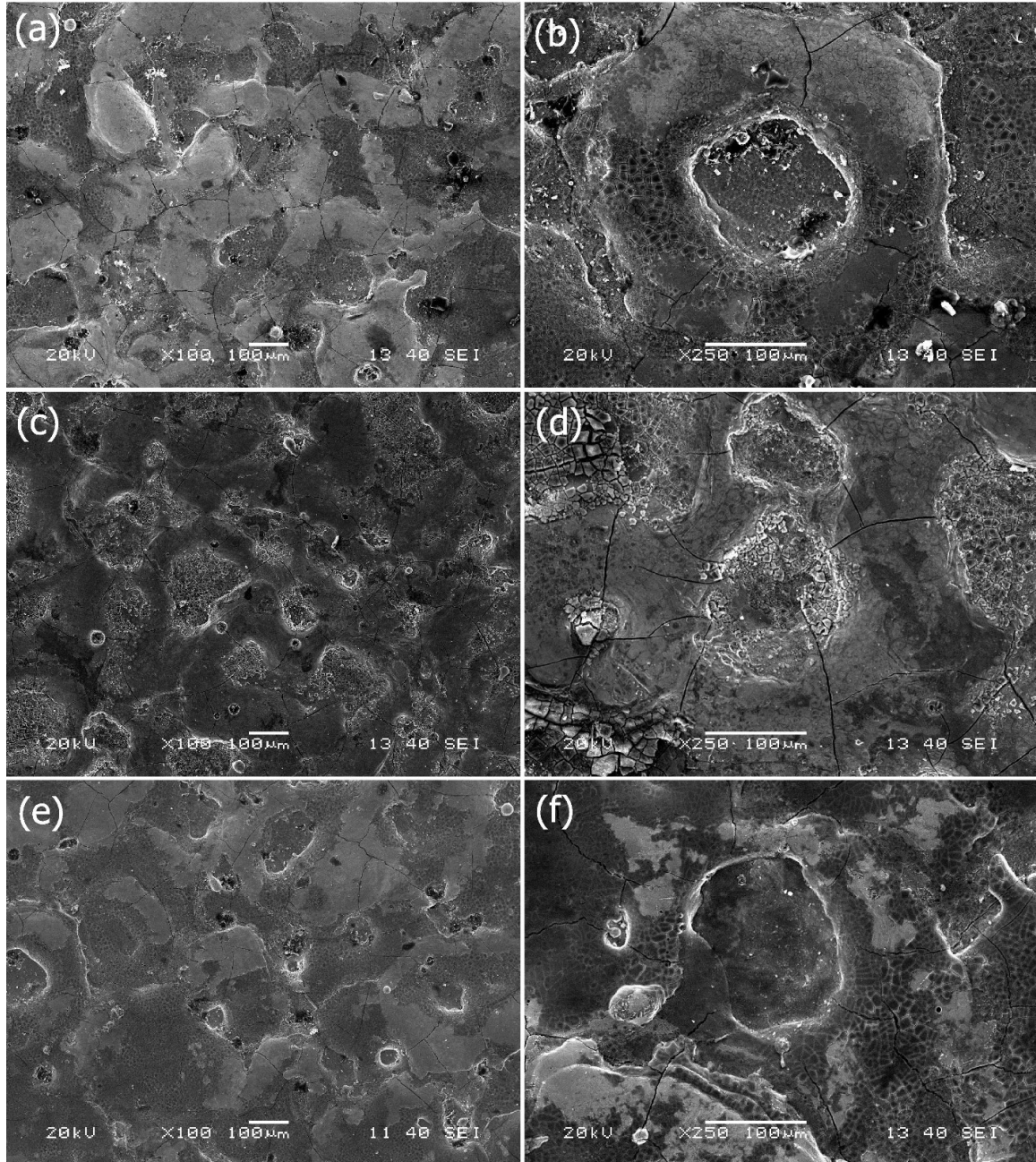
Fig. 4.30 Surface morphology using (a, b) graphite (c, d) aluminum and (e, f) silicon powders for C_p= 4 g/l, I_p= 6 A, T_{on}= 300 μs, τ= 75 % and V_g= 80 V

At high duty cycle value of 95 %, it is clearly evident in Fig. 4.29 that a great deal of resolidified globules was observed on the machined surface due to insufficient flushing

action. Very deep craters were formed due to the bulging of molten material at the edges of the craters. Large pockmarks were observed as the time needed for the escaping of gases is very less. They were deep with a high density of global appendages with the resulting surfaces thus being matt in appearance.

A relatively smooth surface with little amount of solidified globules was observed as shown in Fig. 4.30 at a gap voltage of 80 V. This may be due to the enhanced spark gap at a high voltage allowing easier flush out of debris. The amount and size of pock marks were also reduced as the large spark gap allows easier escape of gases.

4.3.2.1 Surface crack density

Table 4.8 SCD for different powders

Run	C_p	I_p	T_{on}	τ	V_g	SCD ($\mu m/\mu m^2$)		
	(g/l)	(A)	(μs)	(%)	(V)	Graphite	Aluminum	Silicon
1	0	6	300	75	60	0.021	0.021	0.021
2	2	4	400	85	70	0.015	0.017	0.015
3	2	8	200	85	70	0.023	0.024	0.024
4	2	8	400	85	50	0.023	0.029	0.027
5	2	4	200	85	50	0.008	0.01	0.009
6	2	8	400	65	70	0.02	0.027	0.025
7	2	4	400	65	50	0.016	0.018	0.017
8	2	8	200	65	50	0.022	0.024	0.023
9	2	4	200	65	70	0.007	0.008	0.008
10	4	6	300	75	60	0.015	0.018	0.017
11	4	6	100	75	60	0.014	0.014	0.016
12	4	10	300	75	60	0.023	0.027	0.026
13	4	6	300	75	40	0.014	0.016	0.016
14	4	6	300	75	80	0.013	0.017	0.015
15	4	6	300	75	60	0.015	0.014	0.013
16	4	6	300	75	60	0.015	0.018	0.017
17	4	6	300	55	60	0.015	0.019	0.017
18	4	6	300	95	60	0.015	0.019	0.017
19	4	6	300	75	60	0.014	0.016	0.016
20	4	6	300	75	60	0.015	0.015	0.015
21	4	6	300	75	60	0.015	0.014	0.014
22	4	6	500	75	60	0.017	0.021	0.02
23	4	2	300	75	60	0.007	0.008	0.008
24	6	8	400	65	50	0.018	0.022	0.024
25	6	8	400	85	70	0.016	0.019	0.02

26	6	4	200	65	50	0.009	0.01	0.011
27	6	4	200	85	70	0.006	0.007	0.008
28	6	8	200	85	50	0.015	0.019	0.021
29	6	8	200	65	70	0.015	0.019	0.021
30	6	4	400	65	70	0.011	0.012	0.013
31	6	4	400	85	50	0.01	0.012	0.014
32	8	6	300	75	60	0.014	0.016	0.017
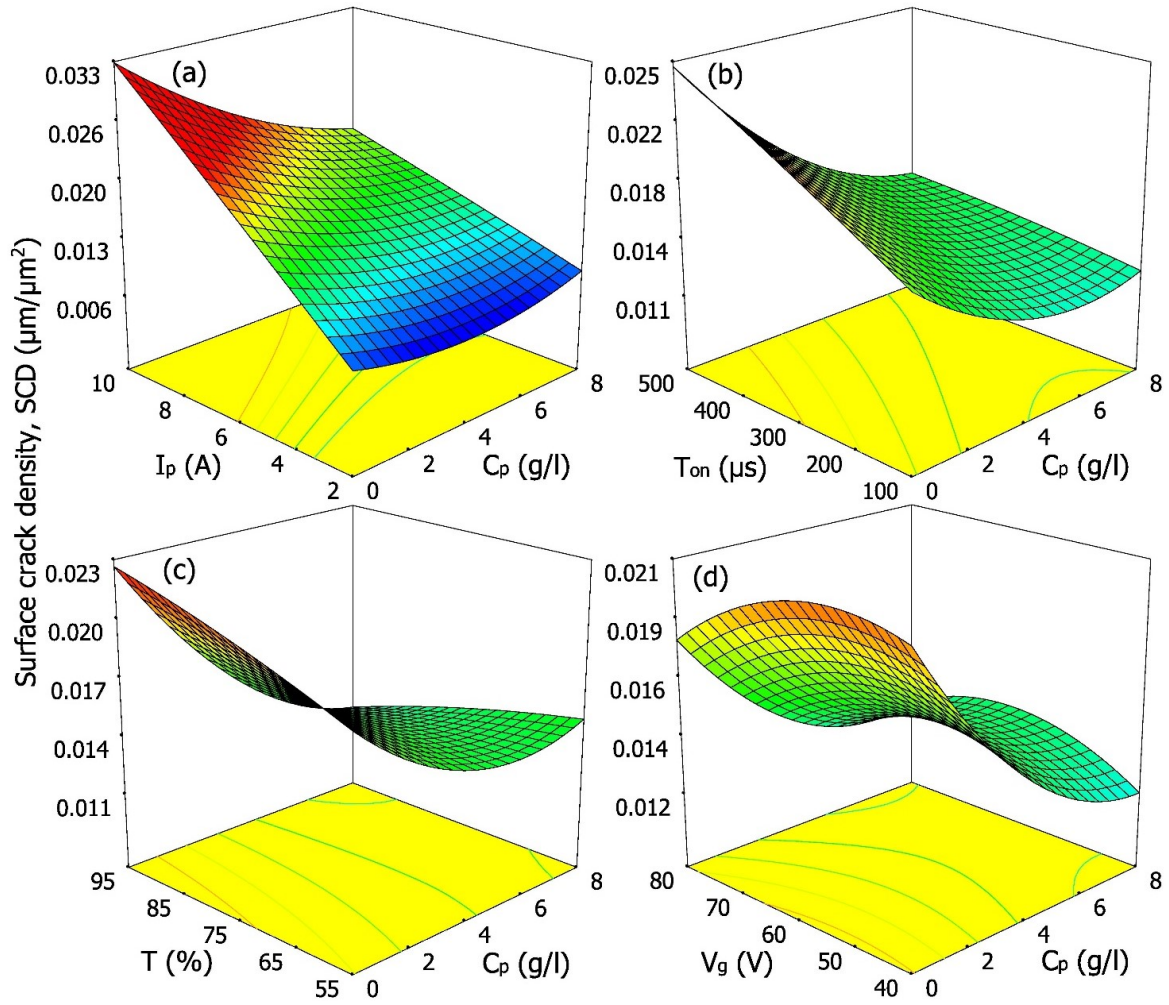
Fig. 4.31 Surface plots (a) C_p vs. I_p (b) C_p vs. T_{on} (c) C_p vs. τ and (d) C_p vs. V_g for SCD using graphite powder

Minimum SCD could be observed with graphite powder due to its high thermal conductivity. It is followed by Al-suspended dielectric due to a combination of high electrical and thermal conductivities. Si powder-suspended dielectric resulted in more severe thermal cracking due to its low thermal and electrical conductivities. However, at

higher powder concentrations (more than 6g/l), aluminum produced the highest SCD. This can be attributed to larger concentration of agglomerated aluminum particles which might have caused arcing.
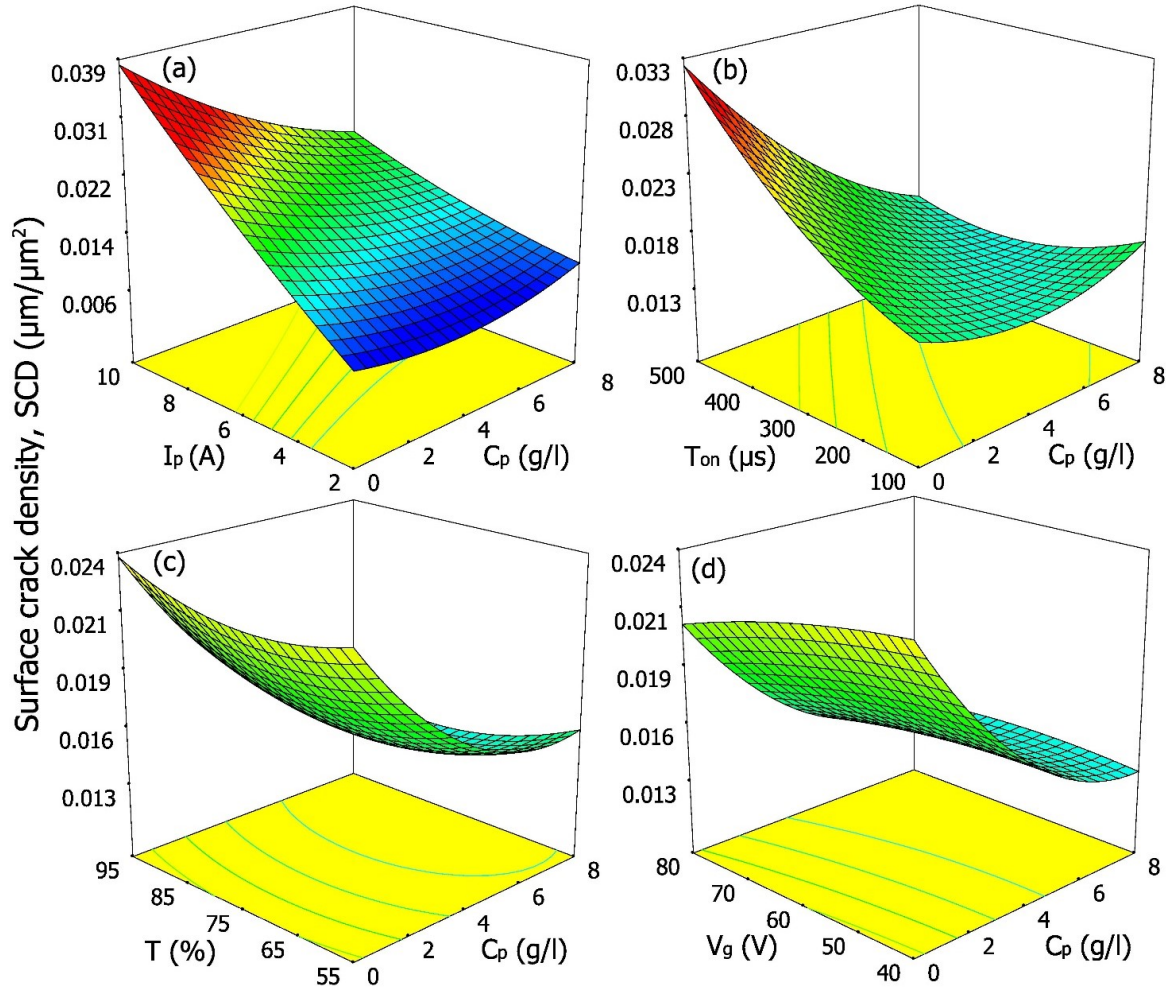
Fig. 4.32 Surface plots (a) C_p vs. I_p (b) C_p vs. T_{on} (c) C_p vs. τ and (d) C_p vs. V_g for SCD using aluminum powder

Table 4.9 illustrates the abridged ANOVA for SCD using three different powder-mixed dielectrics. $P < 0.0001$ for all three cases indicates that the models are significant. The insignificant lack of fit values of 0.4635, 0.6514 and 0.7538 for graphite, aluminum and silicon powders imply that the models fit well with the experimental data. The correlation coefficients for SCD using graphite, aluminum and silicon powder-mixed dielectrics are 99.11 %, 91.70 % and 93.28 % respectively. In addition, there are minor differences between Adj R^2 and Pred R^2. After deleting insignificant process parameters, RSM-based mathematical models for SCD using three different dielectrics have been determined and represented in equations (4.9), (4.10) and (4.11).
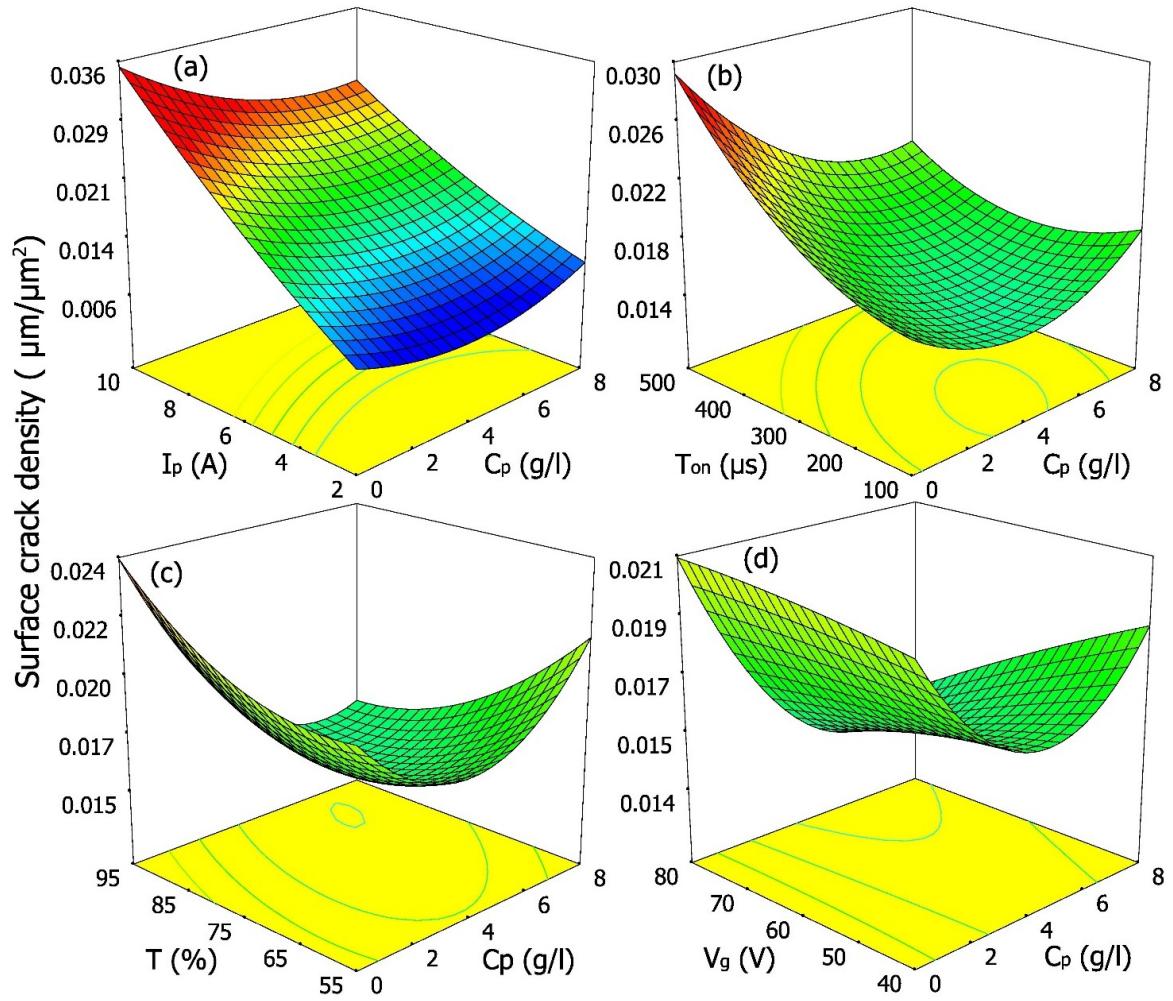
Fig. 4.33 Surface plots (a) C_p vs. I_p (b) C_p vs. T_{on} (c) C_p vs. τ and (d) C_p vs. V_g for SCD using silicon powder

$$(SCD)_{Graphite} = 0.0096 + 0.001667*A + 0.003308*B + 0.000052*C \qquad (4.9)$$
$$-0.000473*D - 0.000099*E + 0.000126*A^2 - 0.000004*E^2$$
$$-0.000192A*B - 0.000033*A*D - 0.000007*B*C + 0.000021*B*D$$
$$+0.000008*D*E$$

$$(SCD)_{Al} = 0.0136 + 0.001752*A + 0.00465*B + 0.000061*C \qquad (4.10)$$
$$-0.000841*D + 0.000005*D^2 - 0.000231*A*B - 0.000004*A*C$$
$$-0.000004*B*C$$

$$(SCD)_{Si} = -0.00286 - 0.002114*A + 0.004065*B + 0.00001*C \qquad (4.11)$$
$$+0.000202*A^2 - 0.000005*B*C$$

81

Table 4.9 Abridged ANOVA for SCD

Source	Graphite	Aluminum	Silicon
Model	P < 0.0001	P < 0.0001	P < 0.0001
Lack of fit	P = 0.4635	P = 0.7538	P = 0.6514
Residual	$3.19*10^{-7}$	$2.46*10^{-6}$	$2.86*10^{-6}$
R^2	0.9911	0.9328	0.9170
Adj R^2	0.9837	0.9132	0.8970
Pred R^2	0.9453	0.8497	0.8580

4.3.2.2 Surface roughness

Table 4.10 SR for different powders

Run	C_p (g/l)	I_p (A)	T_{on} (µs)	τ (%)	V_g (V)	SR (µm) Graphite	SR (µm) Aluminum	SR (µm) Silicon
1	0	6	300	75	60	8.3	8.3	8.3
2	2	4	400	85	70	3.8	3.5	3.4
3	2	8	200	85	70	10.4	10.7	10.2
4	2	8	400	85	50	10.4	9.8	8.4
5	2	4	200	85	50	6.6	6.2	5.9
6	2	8	400	65	70	9.7	9	8.6
7	2	4	400	65	50	3.3	3.1	2.9
8	2	8	200	65	50	9	10.1	9.6
9	2	4	200	65	70	7.3	6.8	6.5
10	4	6	300	75	60	6.9	7.1	6.2
11	4	6	100	75	60	7.1	7.5	6.3
12	4	10	300	75	60	10.4	10.7	9.3
13	4	6	300	75	40	6.3	5.8	5.6
14	4	6	300	75	80	6.7	6.9	6.2
15	4	6	300	75	60	6.6	5.4	4.7
16	4	6	300	75	60	6.9	7.1	6.2
17	4	6	300	55	60	6.6	7.7	6.1
18	4	6	300	95	60	6.8	7.5	6
19	4	6	300	75	60	6.3	6.5	5.6
20	4	6	300	75	60	6.8	6	5.2
21	4	6	300	75	60	6.6	5.6	4.8
22	4	6	500	75	60	5.4	4.8	4.6
23	4	2	300	75	60	3.2	3.2	2.8
24	6	8	400	65	50	6.9	8.3	6.1
25	6	8	400	85	70	6.9	8.3	6.1
26	6	4	200	65	50	5.1	5.4	4
27	6	4	200	85	70	4.6	5.5	4.1

28	6	8	200	85	50	7.1	8.5	6.3
29	6	8	200	65	70	8.1	9.7	7.2
30	6	4	400	65	70	3.8	4.6	3.4
31	6	4	400	85	50	2.6	3.1	2.3
32	8	6	300	75	60	6.4	7.4	5.7
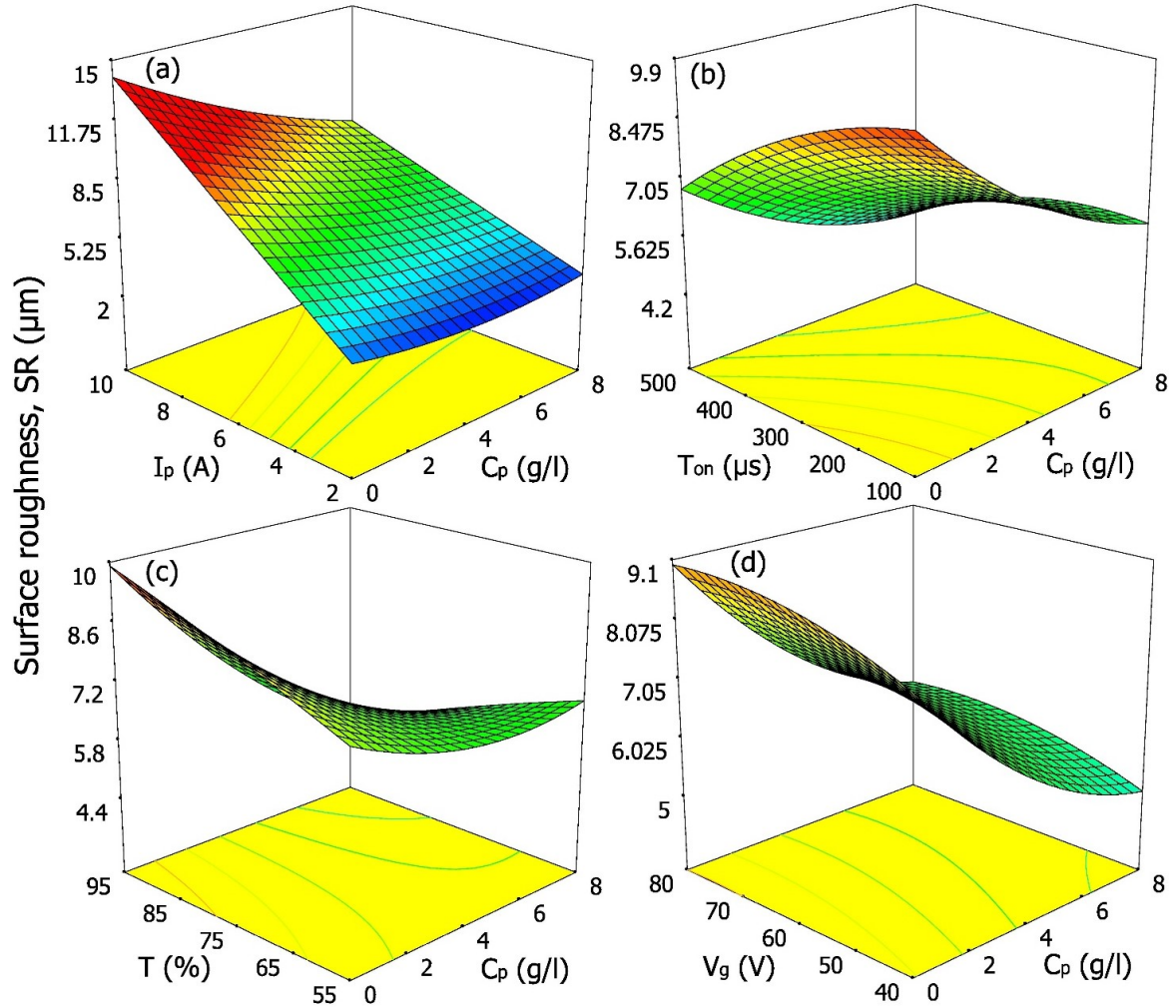
Fig. 4.34 Surface plots (a) C_p vs. I_p (b) C_p vs. T_{on} (c) C_p vs. τ and (d) C_p vs. V_g for SR using graphite powder

A considerable decrease in SR took place with the addition of conductive powder particles such as Al, graphite and Si to the dielectric. Plasma channel gets widened and enlarged when powder particles are mixed with the dielectric. Multiple sparking among the powder particles, distributes the discharge energy over a large area. As a result, large and shallow craters are formed on the workpiece surface [29].

In addition to this, the molten metal is not heavily pressed by the plasma channel and the gas bubbles. These conditions reduce the entrapping of gas in the cavities. Thus, the surface becomes less concave, smooth and uniform [36]. The measured SR values for different powder-mixed dielectrics are provided in Table 4.10.
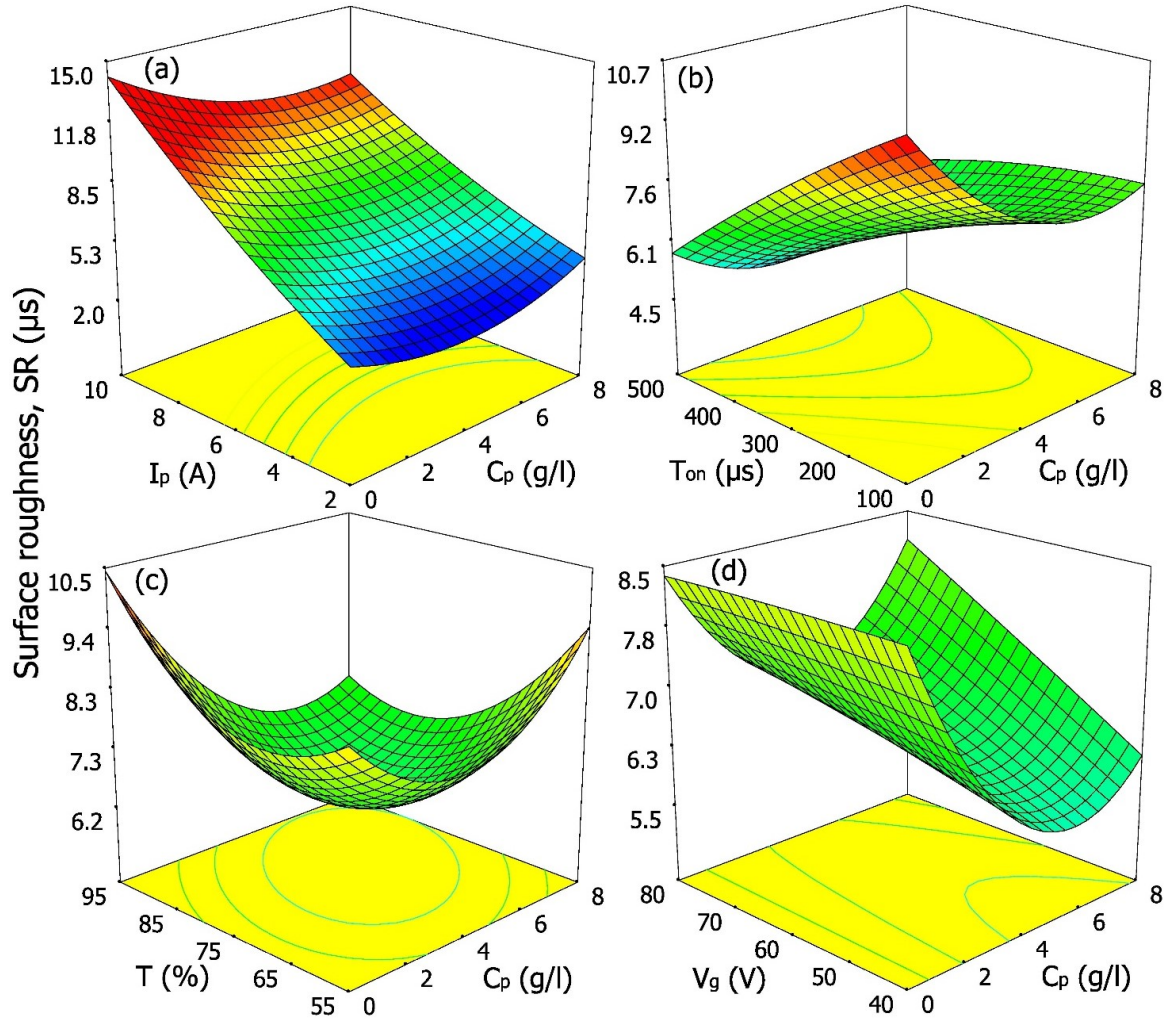
Fig. 4.35 Surface plots (a) C_p vs. I_p (b) C_p vs. T_{on} (c) C_p vs. τ and (d) C_p vs. V_g for SR using aluminum powder

Fig. 4.34, Fig. 4.35 and Fig. 4.36 show the effect of different powder materials and process parameters on SR. Discharge energy increases with peak current causing an hike in impulsive force and removing more molten and gasified materials. This generates deeper and larger discharge craters resulting in high SR. On the other hand, SR slightly decreased with increase in pulse-on time. This may be due to the expansion of discharge column leading to large and shallow cavities. An increase in SR was noted with the raise in duty cycle. This is attributed to the dominant effect of discharge energy per pulse leading to

deeper cavity and insufficient time for flushing the removed debris. SR increased with gap voltage due to the increase in discharge energy. At too long voltage values, IEG becomes very large and spark frequency reduces. This caused SR to decline.
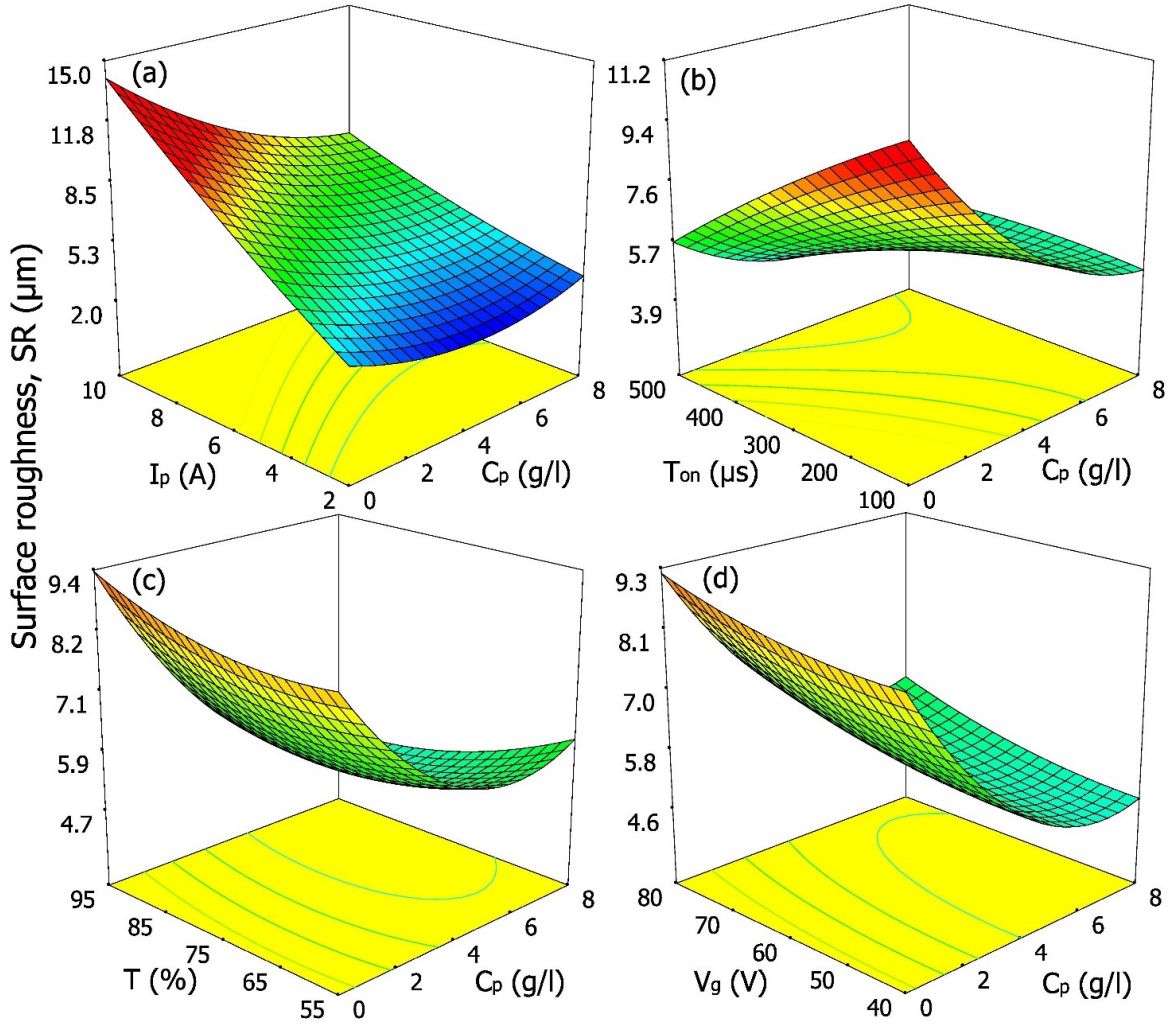
Fig. 4.36 Surface plots (a) C_p vs. I_p (b) C_p vs. T_{on} (c) C_p vs. τ and (d) C_p vs. V_g for SCD using silicon powder

Silicon powder produced the least SR followed by aluminum and graphite owing to its low electrical and thermal conductivities. At a given instance, more number of Si particles enter the electrode gap due to its smaller size. As a consequence, overall discharge energy is more evenly distributed in a larger area. Formation of multiple number of smaller craters during a single discharge also takes place [24]. Use of smaller Si powder particles has, therefore, produced superior surface quality compared to the larger size particles of aluminum and graphite materials. The sharp edges of silicon powder as evident in Fig. 4.8, also augment the abrasive action of the particles on the crater edges. Thus, shallow craters

are observed in case of silicon particles mixed dielectric. Although Al powder has higher electrical conductivity than graphite powder, it provides higher surface roughness than that of graphite powder.

There may be several reasons behind this behavior. First, the density of Al powder is greater than that of graphite powder, which prohibits it from mixing uniformly with the dielectric. Therefore, discharge energies are more evenly distributed among the powder particles in case of graphite powders, which make it suitable for generating smaller and shallow craters. On the other hand, the Al powder has a tendency to agglomerate owing to the electrostatic force or Van der Walls force when added to dielectric. SR decreased with increase in powder concentration and started to decline at high concentrations. It is due to enlarged discharge heat area, which results in reduction in discharge density to form large diameter, shallow craters on the surface. Presence of excessive powder particles causes short circuiting that is responsible for the increase in SR.

Table 4.11 illustrates the abridged ANOVA for SR using three different powder-mixed dielectrics. P < 0.0001 for all three cases indicates that the models are significant. The insignificant lack of fit values of 0.1007, 0.8142 and 0.8939 for graphite, aluminum and silicon powders imply that the models fit well with the experimental data. The correlation coefficients for MRR using graphite, aluminum and silicon powder-mixed dielectrics are 97.88 %, 94.16 % and 95.18 % respectively. In addition, there are minor differences between Adj R^2 and Pred R^2. After deleting insignificant process parameters, RSM-based mathematical models for SR using three different dielectrics have been obtained and shown in equations (4.12), (4.13) and (4.14).

Table 4.11 Abridged ANOVA for SR

Source	Graphite	Aluminum	Silicon
Model	P < 0.0001	P < 0.0001	P < 0.0001
Lack of fit	P = 0.1007	P = 0.8142	P = 0.8939
Residual	0.14	0.37	0.26
R^2	0.9788	0.9416	0.9518
Adj R^2	0.9654	0.9212	0.9350
Pred R^2	0.9078	0.8979	0.9090

$$(SR)_{Graphite} = -9.88 + 0.905*A - 0.28*B - 0.01599*C + 0.2096*D \qquad (4.12)$$
$$+0.2808*E + 0.0373*A^2 - 0.000013*C^2 - 0.0875*A*B - 0.01438*A*D$$
$$+0.002938*B*C + 0.00938*B*D - 0.0035*D*E$$

$$(SR)_{Al} = 23.86 - 0.887 * A + 0.504 * B - 0.019 * C - 0.46 * D + 0.0242 * E \qquad (4.13)$$
$$+0.0911 * A^2 + 0.00302 * D^2 + 0.001875 * B * C$$

$$(SR)_{Si} = 6.12 - 0.985 * A + 0.871 * B - 0.02142 * C + 0.0217 * E + 0.0796 * A^2 \qquad (4.14)$$
$$-0.0969 * A * B + 0.001625 A * C + 0.001375 * B * C$$

4.3.3 Altered layer

EDM being primarily thermal process typically results in different distinct zones in the sub-surface regions. Owing to immense surface heating material removal takes by vaporization. During the process some molten material remains and subsequently resolidifies during cooling (flushing of dielectric) to form a recast layer. Very high thermal energy also alters the microstructure of sub-surface region to a certain depth which is called heat affected zone (HAZ). The zone beyond thermally affected layer is called as bulk material which remains unaffected by the process. The entire heat affected zone inclusive of recast layer is termed as altered layer thickness (ALT).
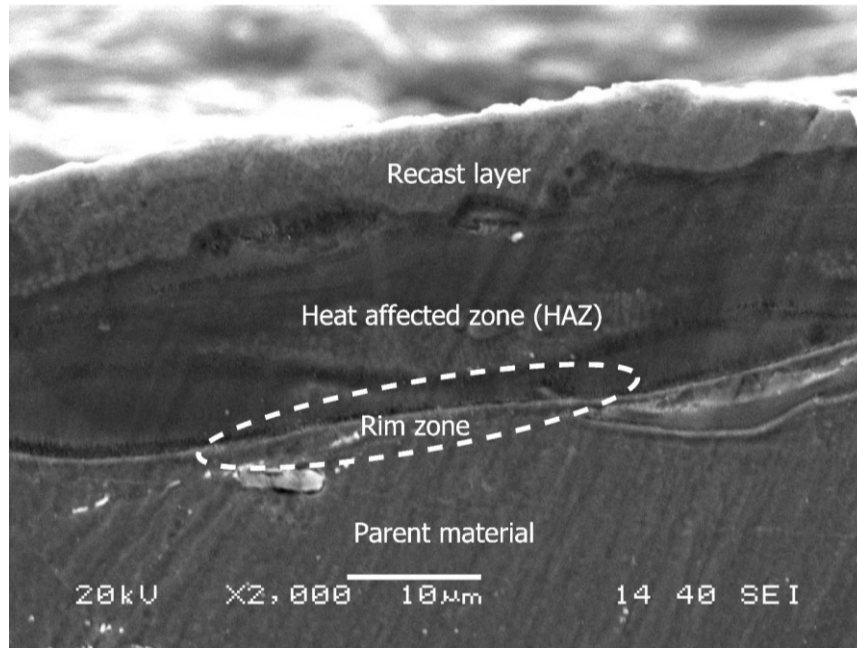
Fig. 4.37 Sub-surface regions of the machined layer

Fig. 4.37 shows four different zones at the sub-surface after machining. The top most zone is the recast layer followed by heat affected zone. The interface between HAZ and bulk material is called rim zone [39]. In many occasions it is difficult to discern between recast layer and HAZ. Therefore, in the current study ALT has been measured and plotted against various parameters after EDM with and without powders.

87

Fig. 4.38 Altered layer using (a) no powder (b) graphite (c) aluminum and (d) silicon powders for C_p= 4 g/l, I_p= 6 A, T_{on}= 300 μs, τ= 75 % and V_g= 40 V
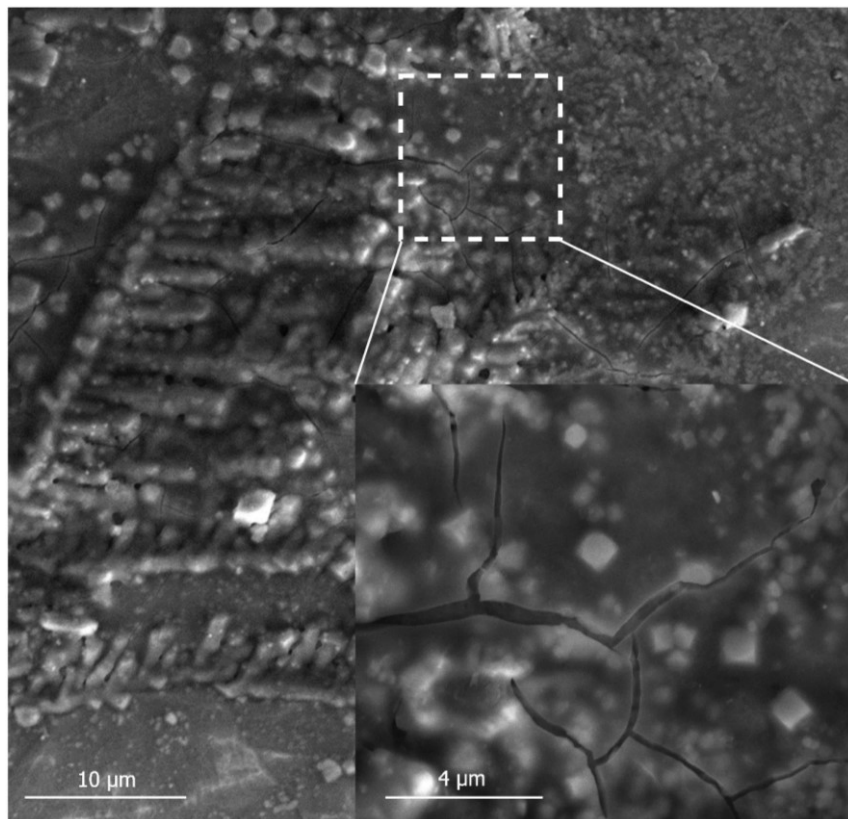
Fig. 4.39 Cracks within the altered layer in conventional EDM (no powder)

Fig. 4.38 shows formation of altered layer after EDM without powder and PMEDM using graphite, aluminum and silicon powders. Evidently altered layer thickness is more in conventional EDM compared to PMEDM process. It has already been observed that powders help distribution of thermal energy over a larger area so that heat density gets reduced. As a consequence, depth of penetration of thermal energy would be less in PMEDM. This causes thermally affected layer to shrink. Graphite has all along resulted in minimum ALT owing to its highest heat of fusion and thermal conductivity. Less ALT for aluminum mixed EDM could be the result of higher thermal conductivity of aluminum than silicon.

Moreover, for conventional EDM, altered layer was non uniform and nature of cracking was distinct from PMEDM. In addition to surface cracks being extended upto sub-surface region (Fig. 4.38(a)), cracks also developed within HAZ (Fig. 4.39) as a result of more intense heating and cooling and consequent rise in residual stress. Such crack network could not be located in any of the samples machined using PMEDM. So it can be inferred that mixing of powder with dielectric effectively lowers density of heat and residual stress finally leading to reduction in ALT.
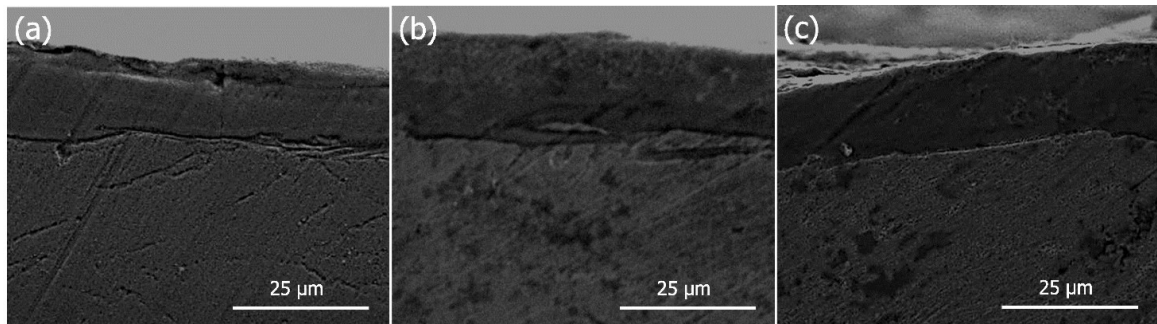
Fig. 4.40 Altered layer using (a) graphite (b) aluminum and (c) silicon powders for C_p= 8 g/l, I_p= 6 A, T_{on}= 300 µs, τ= 75 % and V_g= 40 V

Increase in concentration of powders in dielectric has clearly brought reduction in ALT as evident from Fig. 4.40. This may be attributed to enlargement of discharge gap and widening of plasma channel with increase in concentration and consequent mitigated intensity of discharge. However, for aluminum powder, this reduction is least prominent compared to the other two. This is due to the agglomeration of aluminum particles at higher concentration leading to possibility of arcing and restriction of flow of dielectric in the discharge gap.

The altered layer appeared to be thinner (Fig. 4.41) as the peak current decreases. This is due to the fact that, increase in the peak current leads to an increase in the pulse energy

which increases the rate of melting and evaporation of electrodes. This causes higher volume of molten material and the dielectric fluid is unable to flush away all the molten material causing it to build upon the surface of the parent material.
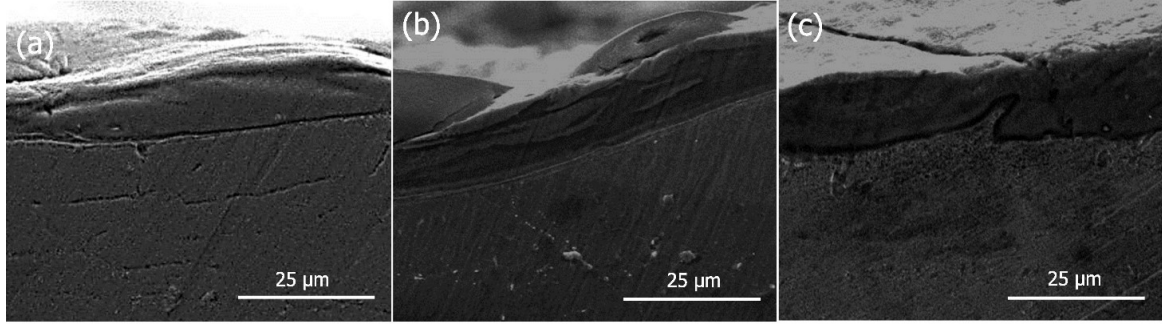
Fig. 4.41 Altered layer using (a) graphite (b) aluminum and (c) silicon powders for C_p= 4 g/l, I_p= 2 A, T_{on}= 300 μs, τ= 75 % and V_g= 40 V

When pulse-on time duration was increased, altered layer thickness also increased as shown in Fig. 4.42 regardless of powder additive. The increase in ALT as a result of increasing pulse-on time is mainly attributed to the production of more molten material by the greater discharge energy magnitudes. Although more molten material is produced, the amount of molten material removed by flushing remains relatively constant and results in a net increase in ALT.
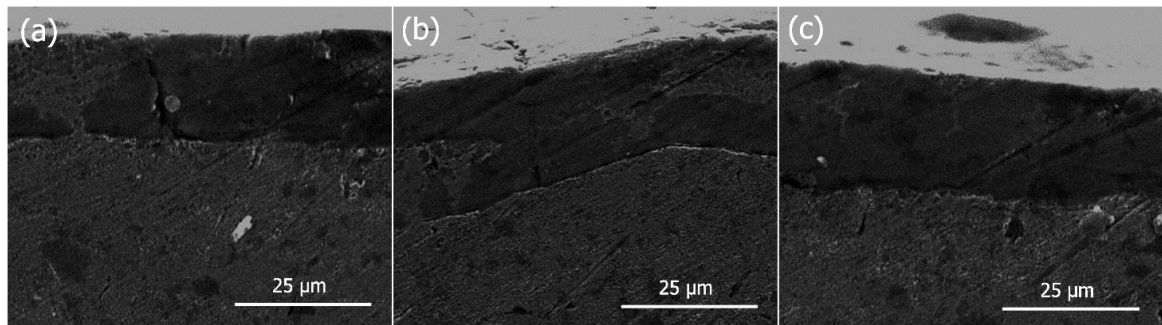
Fig. 4.42 Altered layer using (a) graphite (b) aluminum and (c) silicon powders for C_p= 4 g/l, I_p= 6 A, T_{on}= 500 μs, τ= 75 % and V_g= 40 V

Increase in duty cycle caused prominent increase in ALT particularly for PMEDM using aluminum and silicon powders (Fig. 4.43). This may be explained by greater thermal energy associated with prolonged sparking. Owing to higher heat of fusion and thermal conductivity samples machined with graphite powder were more immune to such rise in discharge energy.

The altered layer thickness decreased with gap voltage (Fig. 4.44) as the expansion of spark gap allowed more powder into it causing fall in discharge energy and consequent heat input to the work surface.
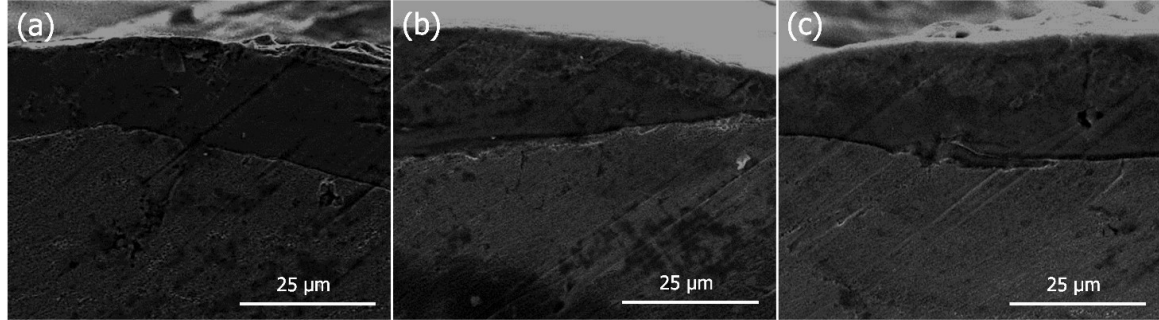
Fig. 4.43 Altered layer using (a) graphite (b) aluminum and (c) silicon powders for C_p= 4 g/l, I_p= 6 A, T_{on}= 300 µs, τ= 95 % and V_g= 40 V
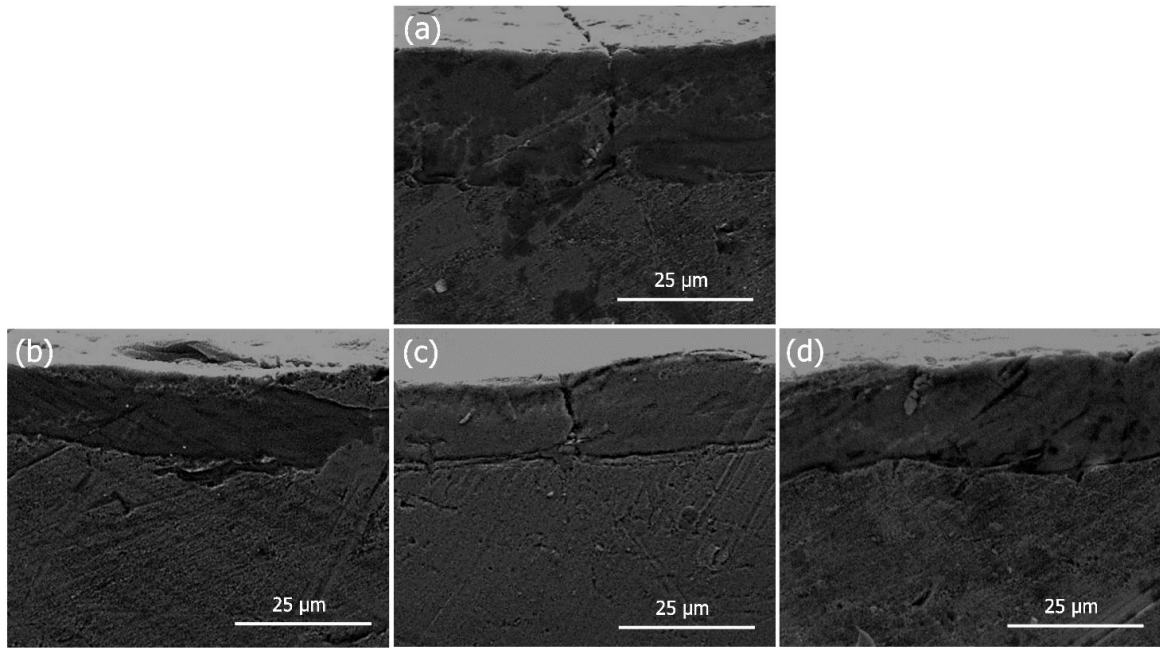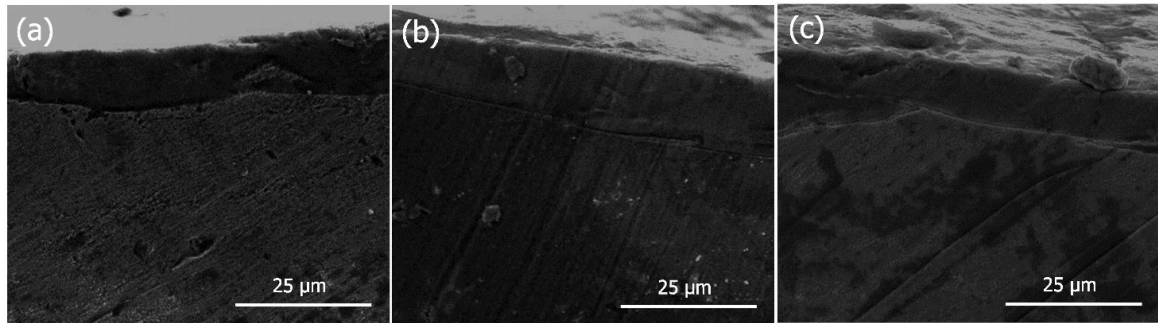

Fig. 4.44 Altered layer using (a) graphite (b) aluminum and (c) silicon powders for C_p= 8 g/l, I_p= 6 A, T_{on}= 300 µs, τ= 75 % and V_g= 80 V

**4.3.3.1 Influence of process parameters on ALT**

High spark gap is produced when powder particles are suspended in dielectric due to the reduction in overall electrical resistivity. The enlarged spark gap results in low discharge energy distribution on the workpiece surface. Besides, the added powder takes some part of heat away from the sparking zone. These two phenomena lead to a shallow melted zone in the workpiece surface [29]. Hence a thin altered layer as shown in Fig. 4.38(b), (c) and (d) is realized in case of PMEDM compared to conventional EDM (Fig. 4.38(a)).

The altered layer was continuous and evenly distributed in case of powder mixed dielectric. The measured ALT values for different powder-mixed dielectrics is given in Table 4.12. Corresponding surface plots are shown in Fig. 4.45, Fig. 4.46 and Fig. 4.47.

ALT increased with the increase in peak current. At high peak current values, a steep thermal gradient builds up beneath the melting zone due to the availability of high discharge

energy. This thermal effect causes the production of molten material that is not completely flushed out by the dielectric. The remaining molten metal solidifies and forms a thick altered layer during the pulse-off time [172].

Table 4.12 ALT for different powders

Run	C_p (g/l)	I_p (A)	T_{on} (μs)	τ (%)	V_g (V)	ALT (μm)		
						Graphite	Aluminum	Silicon
1	0	6	300	75	60	31.97	31.97	31.97
2	2	4	400	85	70	22.45	22.92	27.05
3	2	8	200	85	70	32.05	36.29	42.84
4	2	8	400	85	50	39.02	39.84	42.62
5	2	4	200	85	50	12.85	13.12	15.49
6	2	8	400	65	70	36.88	37.66	36.79
7	2	4	400	65	50	24.85	25.38	29.95
8	2	8	200	65	50	32.87	33.56	39.62
9	2	4	200	65	70	11.22	11.46	13.53
10	4	6	300	75	60	23.61	26.52	28.45
11	4	6	100	75	60	17.47	17.83	22.28
12	4	10	300	75	60	35.51	39.88	42.79
13	4	6	300	75	40	21.3	21.75	25.68
14	4	6	300	75	80	20.31	24.62	25.22
15	4	6	300	75	60	18.04	20.26	27.08
16	4	6	300	75	60	23.62	26.52	28.46
17	4	6	300	55	60	23.42	28.48	27.29
18	4	6	300	95	60	23.08	27.74	27.82
19	4	6	300	75	60	21.5	24.14	25.91
20	4	6	300	75	60	19.77	22.2	27.93
21	4	6	300	75	60	18.43	20.69	27.13
22	4	6	500	75	60	26.58	28.01	28.95
23	4	2	300	75	60	10.75	12.07	12.95
24	6	8	400	65	50	27.68	36.17	33.36
25	6	8	400	85	70	24.1	31.5	29.05
26	6	4	200	65	50	13.07	17.08	15.75
27	6	4	200	85	70	8.85	11.57	10.67
28	6	8	200	85	50	23.54	30.76	28.36
29	6	8	200	65	70	23.55	30.79	28.39
30	6	4	400	65	70	15.25	19.93	20.9
31	6	4	400	85	50	15.63	20.42	18.83
32	8	6	300	75	60	17.79	27.38	26.06

ALT increased with the increase in pulse-on time. At higher pulse-on duration, high energy is produced so that the thickness of molten metal is more, which cannot be removed by flushing. The amount of debris also increases with pulse-on time. This debris upon cooling adheres and solidifies on the workpiece surface. Increase in spark gap with voltage, allows more powder particles into the spark gap resulting in reduction of ALT. Also, discharge column ebarates and less impulsive force (energy) will reach to the workpiece resulting in diminished ALT.
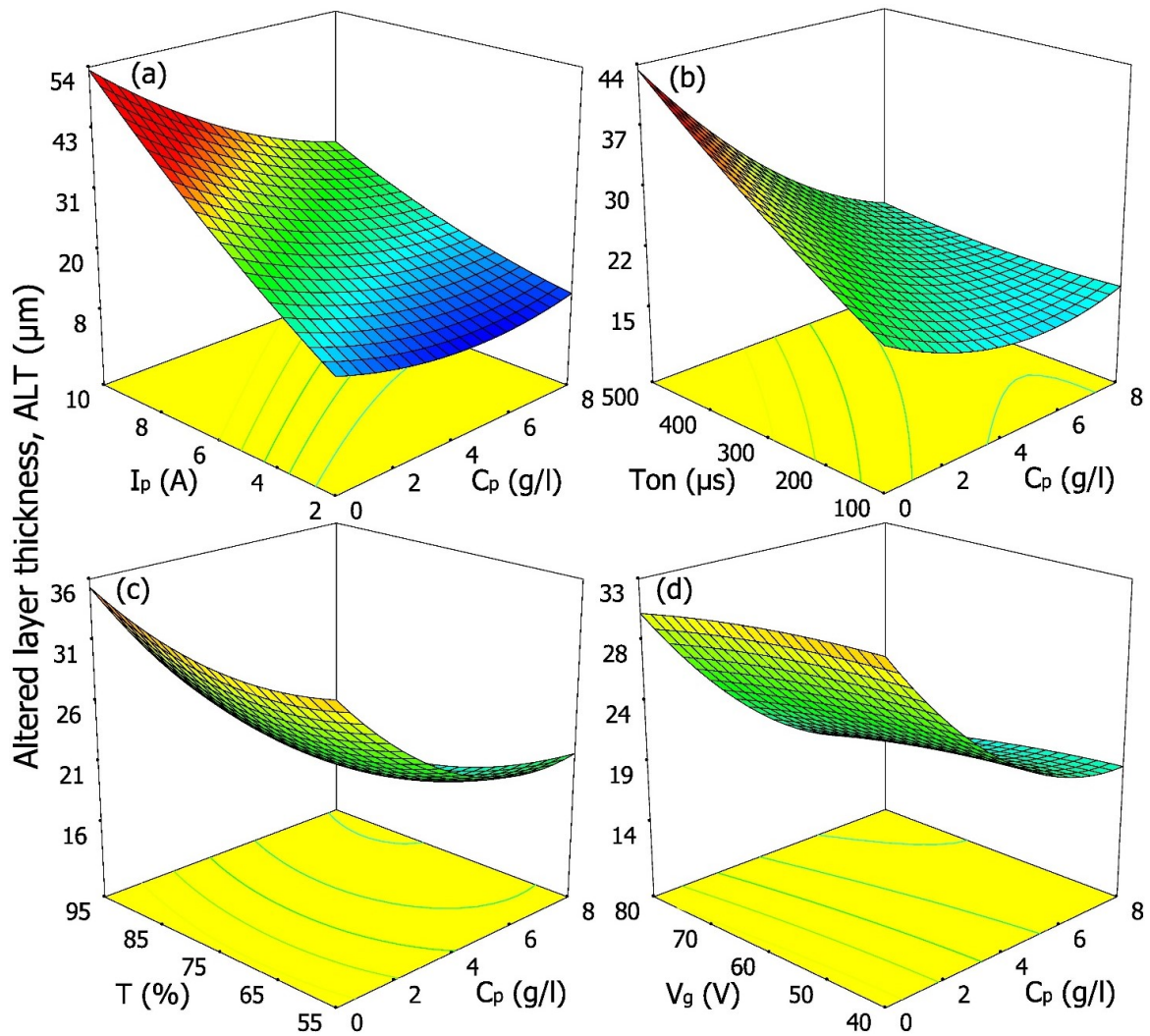
Fig. 4.45 Surface plots (a) C_p vs. I_p (b) C_p vs. T_{on} (c) C_p vs. τ and (d) C_p vs. V_g for ALT using graphite powder

Among the three powders, graphite resulted in the least ALT due to its high thermal conductivity. It is followed by aluminum due to the combination of high thermal and electrical conductivities. Silicon produced highest ALT due to its poor thermal and electrical conductivities.
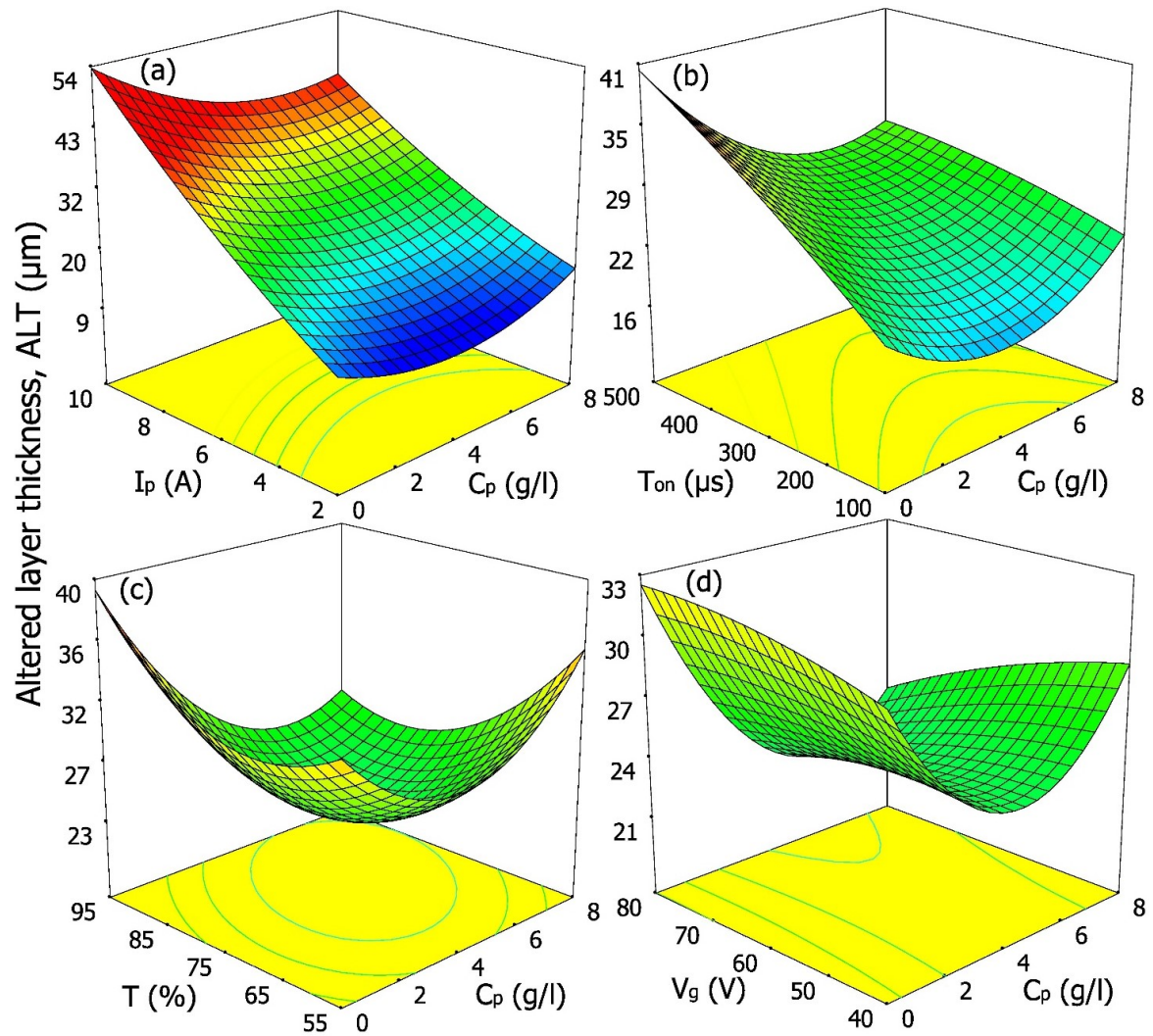
Fig. 4.46 Surface plots (a) C_p vs. I_p (b) C_p vs. T_{on} (c) C_p vs. τ and (d) C_p vs. V_g for ALT using aluminum powder

Table 4.13 illustrates the abridged ANOVA for ALT using three different powder-mixed dielectrics. P < 0.0001 for all three cases indicates that the models are significant. The insignificant lack of fit values of 0.9619, 0.9330 and 0.9846 for graphite, aluminum and silicon powders imply that the models fit well with the experimental data. The correlation coefficients for MRR using graphite, aluminum and silicon powder-mixed dielectrics are 96.19 %, 93.30 % and 98.46 % respectively. In addition, there are minor differences between Adj R^2 and Pred R^2. After deleting insignificant process parameters, RSM-based mathematical models for MRR using three different dielectrics have been obtained and shown in equations (4.15), (4.16) and (4.17).
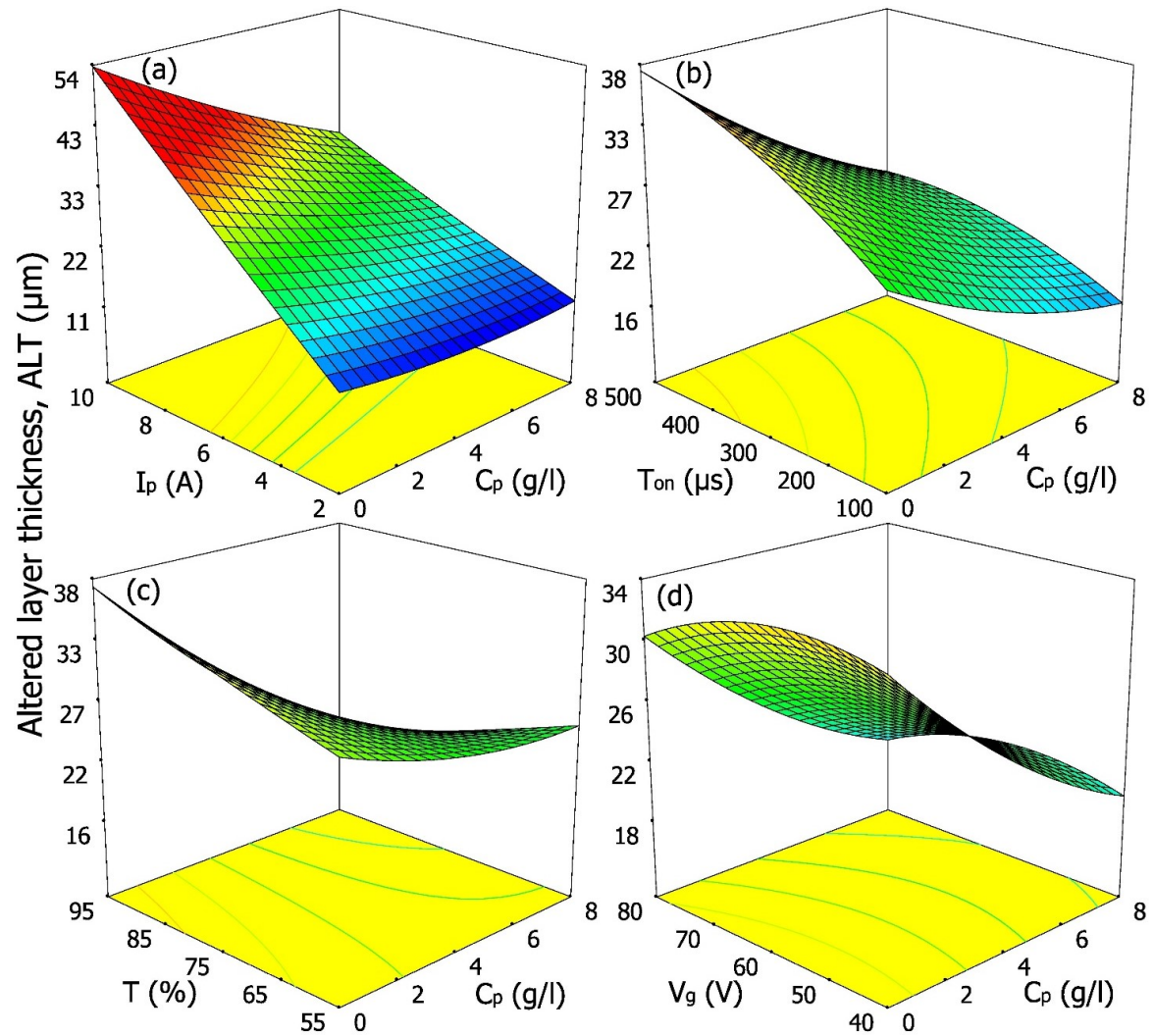
Fig. 4.47 Surface plots (a) C_p vs. I_p (b) C_p vs. T_{on} (c) C_p vs. τ and (d) C_p vs. V_g for ALT using silicon powder

Table 4.13 Abridged ANOVA for ALT

Source	Graphite	Aluminum	Silicon
Model	P < 0.0001	P < 0.0001	P < 0.0001
Lack of fit	P = 0.9532	P = 0.7719	P = 0.2298
Residual	3.03	5.62	1.47
R^2	0.9619	0.9330	0.9846
Adj R^2	0.9486	0.9134	0.9749
Pred R^2	0.9399	0.8917	0.9440

$$(WLT)_{Graphite} = -17.84 + 0.59*A + 6.448*B + 0.0842*C - 0.0714*E \qquad (4.15)$$
$$+ 0.2095*A^2 - 0.365*A*B - 0.00643*A*C - 0.00516*B*C$$

$$(WLT)_{Al} = 50.4 - 3.592*A + 5.994*B + 0.0696*C - 1.649*D + 0.368*A^2 \qquad (4.16)$$
$$+ 0.0108*D^2 - 0.00677*B*C$$

$$(WLT)_{Si} = 24.3 + 5.19*A + 8.982*B + 0.0964*C - 0.641*D - 1.161*E \qquad (4.17)$$
$$- 0.357*A*B - 0.0613*A*D - 0.01209B*C + 0.01461*D*E$$

4.3.4 Surface microhardness

Table 4.14 Surface microhardness for different powders

Run	C_p (g/l)	I_p (A)	T_{on} (μs)	τ (%)	V_g (V)	Vickers microhardness (HV)		
						Graphite	Aluminum	Silicon
1	0	6	300	75	60	1190.71	1190.71	1190.71
2	2	4	400	85	70	1477.15	1379.67	1523.86
3	2	8	200	85	70	1050.16	1082.63	1040.55
4	2	8	400	85	50	1121.05	1131.95	1127.22
5	2	4	200	85	50	1213.34	1196.15	1225.26
6	2	8	400	65	70	1162.3	1160.64	1167.48
7	2	4	400	65	50	1476.69	1379.35	1523.34
8	2	8	200	65	50	1054.47	1085.63	1045.43
9	2	4	200	65	70	1373.28	1324.19	1433.58
10	4	6	300	75	60	1222.44	1202.48	1249.32
11	4	6	100	75	60	1067.4	1094.62	1062.62
12	4	10	300	75	60	1041.9	1076.89	1031.92
13	4	6	300	75	40	1225.86	1212.64	1285.64
14	4	6	300	75	80	1228.89	1162.45	1180.02
15	4	6	300	75	60	1223.99	1203.56	1251.18
16	4	6	300	75	60	1240.38	1214.96	1270.91
17	4	6	300	55	60	1280.97	1238.95	1329.45
18	4	6	300	95	60	1227.54	1181.47	1212.95
19	4	6	300	75	60	1252.99	1223.73	1286.1
20	4	6	300	75	60	1269.25	1235.04	1305.68
21	4	6	300	75	60	1262.17	1230.12	1297.16
22	4	6	500	75	60	1302.58	1258.23	1345.81
23	4	2	300	75	60	1651.67	1570.64	1886.57
24	6	8	400	65	50	1145.13	1148.7	1168
25	6	8	400	85	70	1153.12	1154.26	1178.45

26	6	4	200	65	50	1425.09	1343.45	1534.25
27	6	4	200	85	70	1394.56	1322.21	1494.31
28	6	8	200	85	50	1119.68	1081.04	1040.76
29	6	8	200	65	70	1057.19	1087.53	1052.96
30	6	4	400	65	70	1657.08	1504.84	1837.74
31	6	4	400	85	50	1433.89	1349.58	1570.5
32	8	6	300	75	60	1345.58	1288.14	1481.9
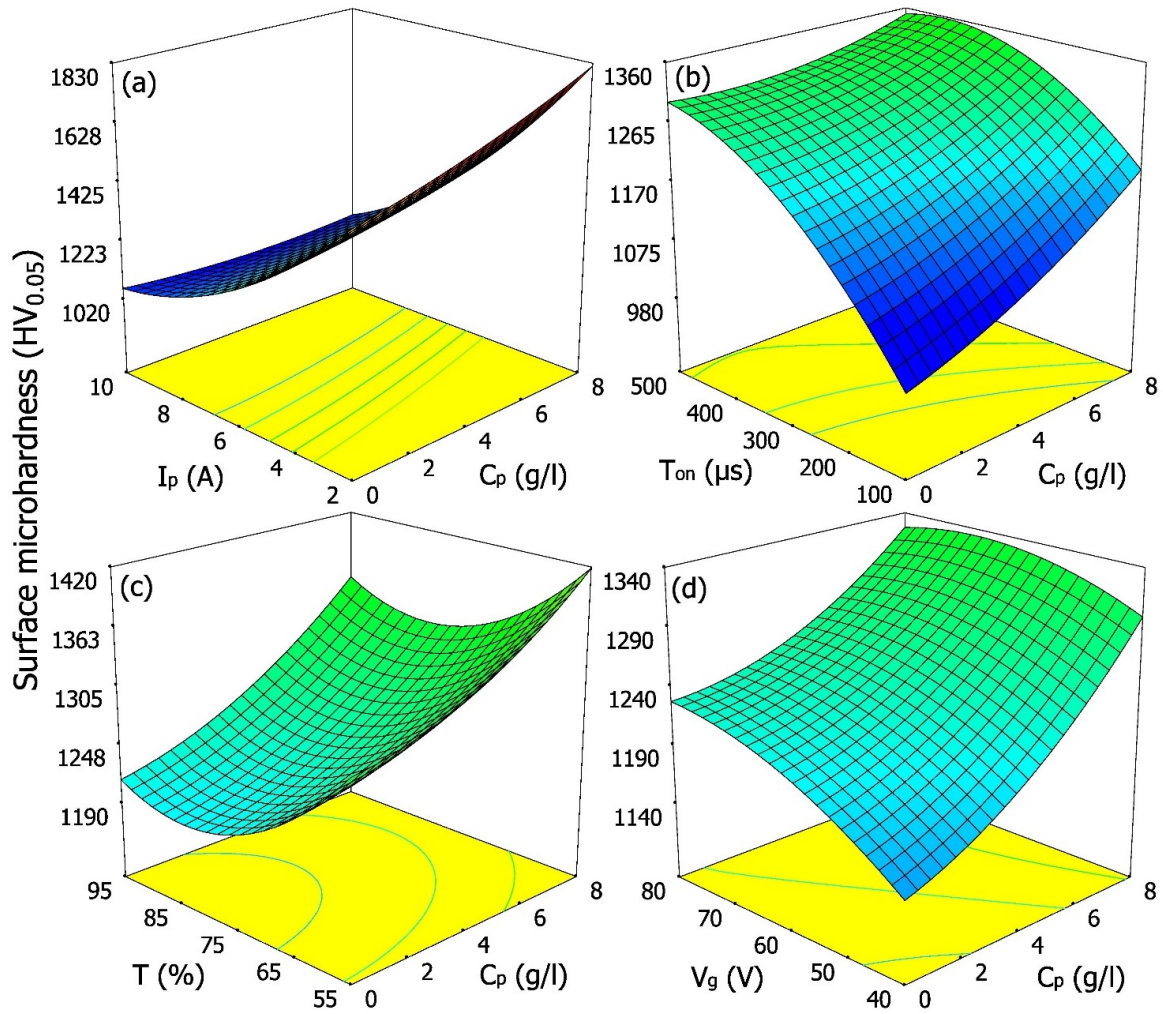
Fig. 4.48 Surface plots (a) C_p vs. I_p (b) C_p vs. T_{on} (c) C_p vs. τ and (d) C_p vs. V_g for surface microhardness using graphite powder

Conducting and semi-conducting powder particles when added to kerosene, increase the ionization in inter electrode gap. PMEDM using different powders revealed surface hardening of Inconel 625 which was clearly more than that obtained with conventional EDM (with pure dielectric). The possible mechanism behind this interesting phenomena

may be explained as fallows. The energized plasma channel causes more pyrolysis and breakage of C-H bonds. The availability of more carbon atoms leads to the formation of hard metal carbides on the machined surface. Augmentation of surface microhardness may also be explained by the promotion of cuboidal γ' phase after transfer of thermal energy to the workpiece. Rise in strength due to precipitation of γ' phase has already been discussed in section 4.4.2. The measured microhardness values for different powder-mixed dielectrics is given in Table 4.14.
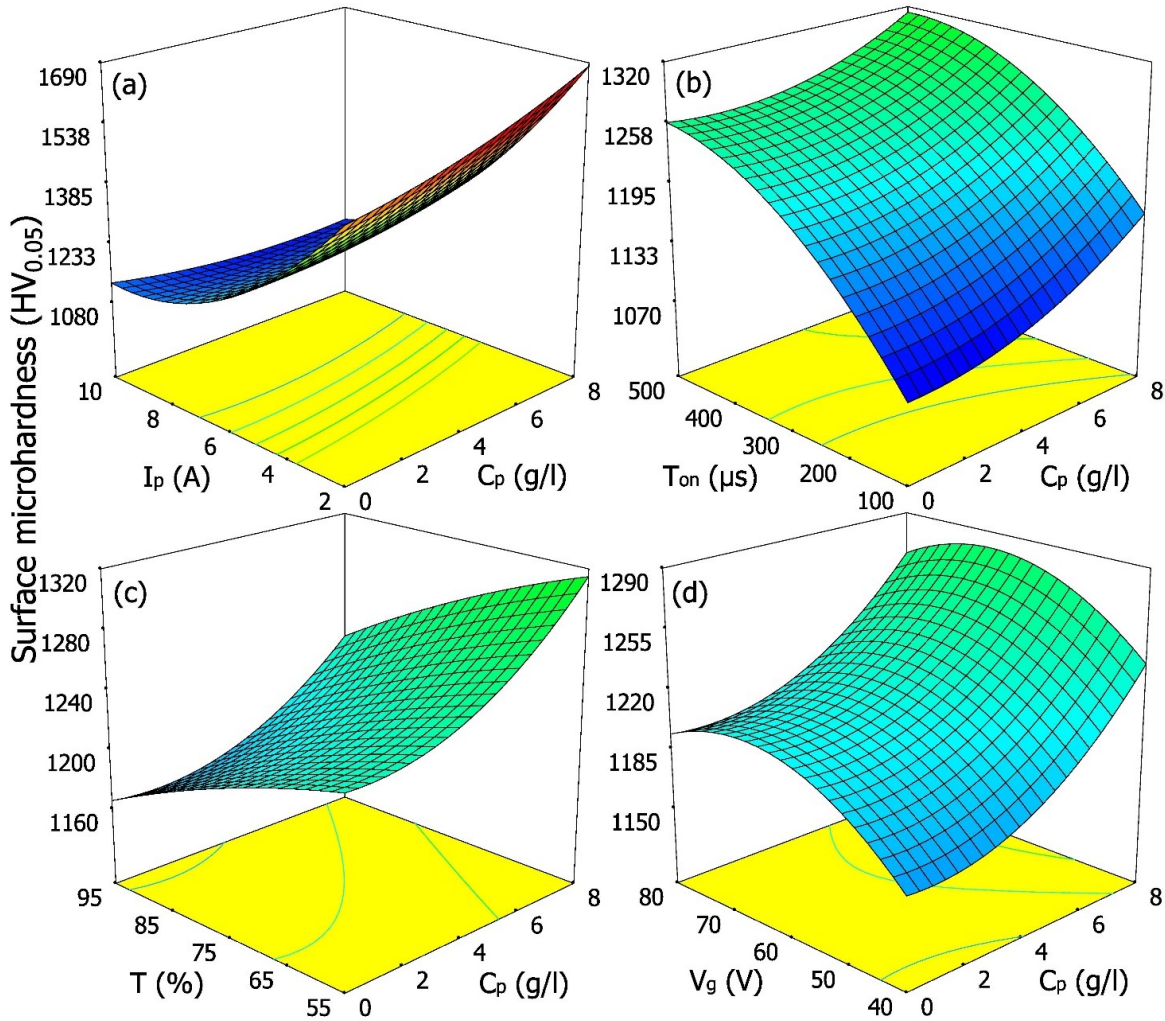
Fig. 4.49 Surface plots (a) C_p vs. I_p (b) C_p vs. T_{on} (c) C_p vs. τ and (d) C_p vs. V_g for surface microhardness using aluminum powder

Fig. 4.48, Fig. 4.49 and Fig. 4.50 show the effect of different powders and machining characteristics on microhardness. Microhardness clearly increased with peak current due to high heating and quenching effects. Microhardness increased with pulse-on time due to an increase in discharge energy.

As pulse-on time increases the energy density decreases and less deposition takes place. Hence, microhardness declines at high pulse-on time. Initial increase in duty cycle enhances microhardness due to increase in spark energy. At high percentage of duty cycle values, time available for cooling becomes very less. Hence, low microhardness values are observed. Discharge energy increases with gap voltage. At high gap voltage, the discharge gap becomes too large and heat density decreases. This causes a reduction in microhardness.
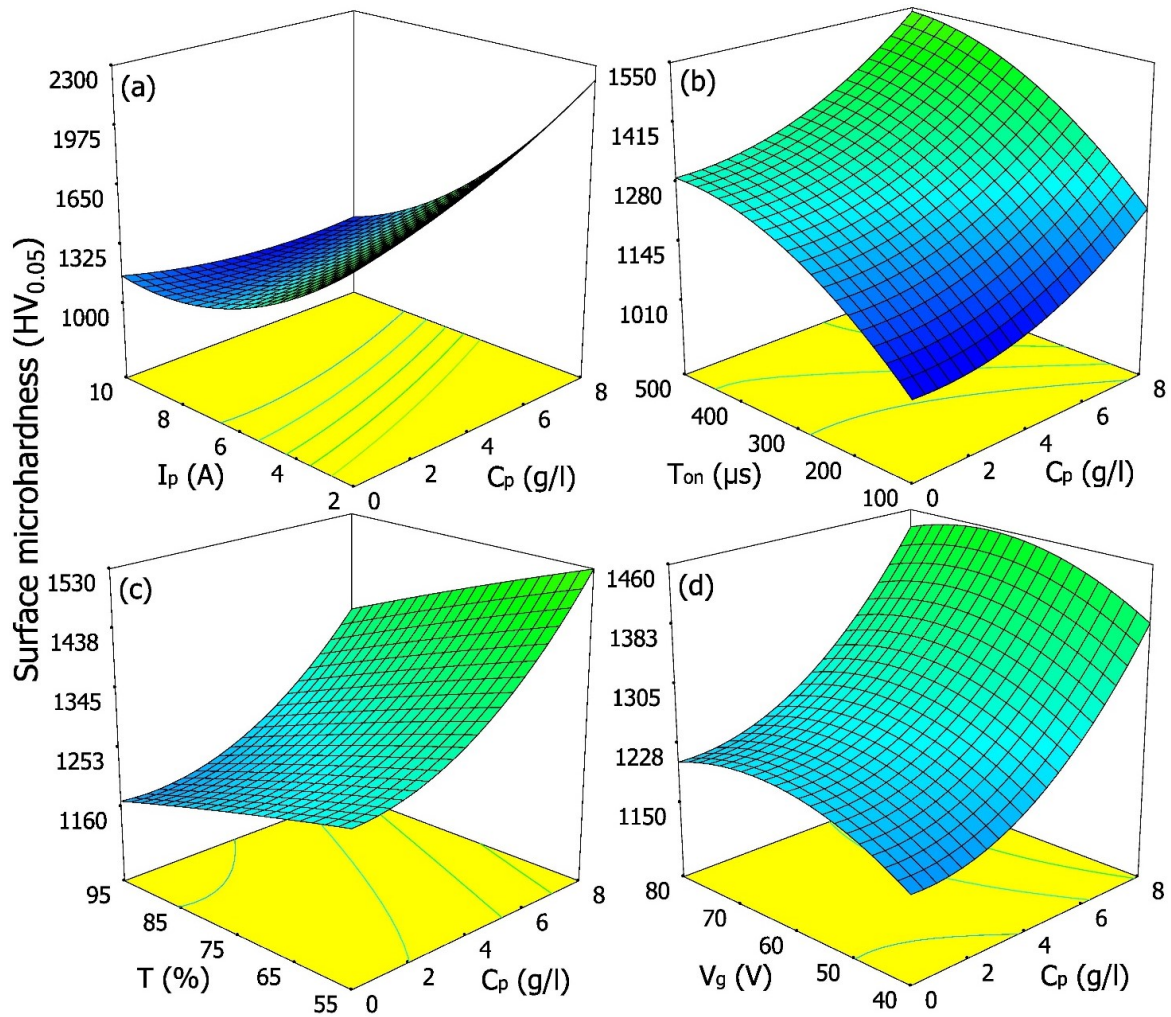
Fig. 4.50 Surface plots (a) C_p vs. I_p (b) C_p vs. T_{on} (c) C_p vs. τ and (d) C_p vs. V_g for surface microhardness using silicon powder

Among the three powders, Si particles produced the surface with the highest microhardness as less amount of heat is removed from the sparking zone owing to low thermal conductivity of Si. The presence of high amount of heat at the workpiece and quenching leads to the formation of hard surface. Formation of silicon carbide (SiC) on the machined surface also enhances the surface hardness. Interestingly, larger and distinct

plates of γ' phase has already been noted with the sample machined with Si-mixed dielectric.

Silicon is followed by Al and graphite in improving the surface hardness. Higher electrical conductivity and the formation of aluminum carbide (Al_4C_3) result in harder machined surface in case of Al compared to graphite. Microhardness improved with powder concentration as more particles enter the inter electrode gap.

Table 4.15 Abridged ANOVA for surface microhardness

Source	Graphite	Aluminum	Silicon
Model	P < 0.0001	P < 0.0001	P < 0.0001
Lack of fit	P = 0.2767	P = 0.1084	P = 0.0950
Residual	59.42	47.39	15.13
R^2	0.9867	0.9800	0.9804
Adj R^2	0.9771	0.9674	0.9680
Pred R^2	0.9549	0.9209	0.9469

$$(SMH)_{Graphite} = 1384 + 20.6*A - 108.5*B + 0.922*C - 7.71*D + 3.32*E \quad (4.18)$$
$$+1.411*A^2 + 5.098*B^2 - 0.000995*C^2 - 3.32*A*B - 0.0793*B*C$$
$$+1.027*B*D - 0.869*B*E + 0.00986*C*E$$

$$(SMH)_{Al} = 1411 + 44.1*A - 160.7*B + 1.741*C - 9.07*D + 6.2*E \quad (4.19)$$
$$+3.07*A^2 + 8.83*B^2 - 0.001248*C^2 - 7.87*A*B - 0.0719*B*C$$
$$+1.097*B*D - 0.886*B*E$$

$$(SMH)_{Si} = 1002 + 23.15*A - 98.1*B + 1.012*C - 5.23*D + 10.45*E \quad (4.20)$$
$$+4.996*B^2 - 0.000764*C^2 - 0.0556*E^2 - 2.7*A*B - 0.0395*B*C$$
$$+0.637*B*D - 0.527*B*E$$

Table 4.15 illustrates the abridged ANOVA for surface microhardness using three different powder-mixed dielectrics. P < 0.0001 for all three cases indicates that the models are significant. The insignificant lack of fit values of 0.2767, 0.1084 and 0.09850 for graphite, aluminum and silicon powders imply that the models fit well with the experimental data. The correlation coefficients for MRR using graphite, aluminum and silicon powder-mixed dielectrics are 98.67 %, 98.00 % and 98.04 % respectively. In addition, there are minor differences between Adj R^2 and Pred R^2. After deleting

insignificant process parameters, RSM-based mathematical models for MRR using three different dielectrics have been obtained and shown in equations (4.18), (4.19) and (4.20).

4.3.5 Microhardness depth profile
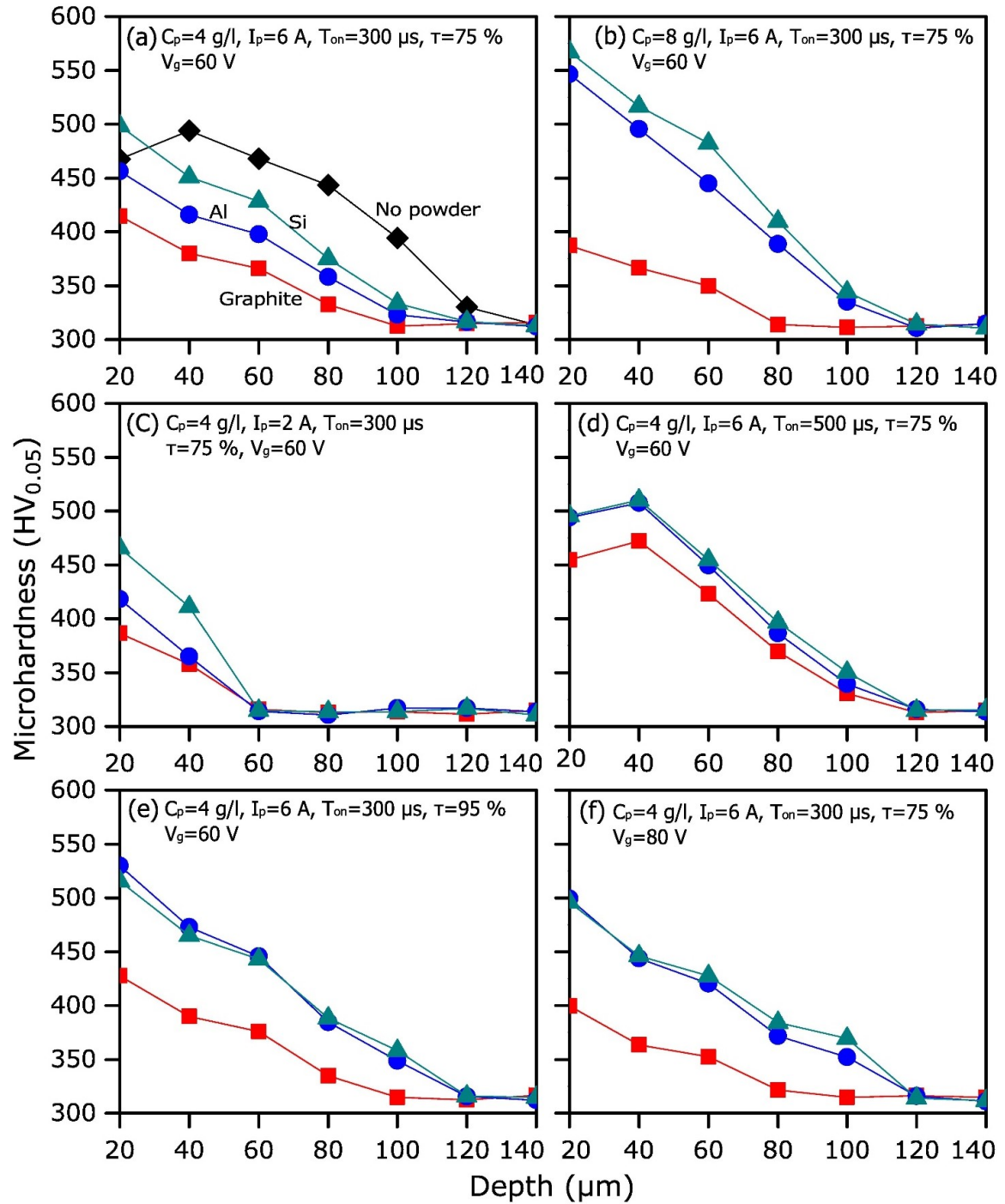
Fig. 4.51 Microhardness depth profile

Microhardness has been measured along the direction starting from the machined surface. Influences of different process parameters and powder-mixed dielectrics on hardness depth profile are presented in Fig. 4.51. It was observed that microhardness close to top surface region i.e., in recast layer was high which can be attributed to the formation of carbides and precipitation of γ'phase on the top surface [132]. Decrease in hardness beyond this zone is due to diminished effect of heating and quenching.

Compared to conventional EDM, less hardness was realized along the cross section, when powder-suspended dielectric was used due to a reduction in discharge energy density. Among the three powders, graphite resulted in the least cross-sectional microhardness due to its high thermal conductivity. It is followed by aluminum due to the combination of high thermal and electrical conductivities. Silicon produced highest cross-sectional microhardness. Therefore, similar trend between gradient and top surface hardening has been noted.

Microhardness along depth has decreased as due to the decrease in discharge energy with the powder concentration. Microhardness increased with peak current due to high heating and quenching effects at large peak current values. Microhardness increased with pulse time due to the increase in discharge energy. Also, the time available for heat transfer increases with pulse-on time resulting in larger heat effected zone. Cross-sectional microhardness was directly proportional to duty cycle due to the increase in spark energy. At high gap voltage, the discharge gap becomes larger and heat density decreases. This causes a reduction in microhardness.

## 4.3.6 Composition, phases, grain size and lattice strain

Table 4.16 Composition of machined surfaces (I_p= 6 A, T_{on}= 300 μs, τ= 75 % and V_g= 40 V)

Element	Weight %				
	As-received Inconel 625	EDM with no powder	PMEDM (C_p= 4 g/l)		
			Graphite	Aluminum	Silicon
Al	0.32	0.52	0.08	0.27	0.4
Si	0.35	-	0.74	0.26	-
P	-	0.29	0.05	0.95	0.53
S	0.01	0.26	0.35	-	1.44
Ti	0.38	0.17	-	0.16	-
Cr	22.36	24.46	24.67	22.93	21.81
Mn	0.35	0.85	0.34	-	1.22
Fe	4.58	5.08	4.78	6.29	4.1
Ni	58.74	57.03	56.24	49.66	58.91
Nb	3.87	5.35	3.15	8.52	4.3
Mo	9.04	5.99	9.6	10.96	7.29

In order to investigate the influence of different powder materials on possible alteration in chemical composition of Inconel 625, EDS analysis was carried out on the machined surface. This was followed by XRD study for identification of different phases and their modification as a result of PMEDM process.

Element	Weight %	
	Area 1	Area 2
C	-	2.03
Al	-	0.24
Ti	0.70	0.88
Cr	23.21	21.12
Fe	4.75	7.33
Ni	55.34	44.36
Nb	4.85	10.09
Mo	11.15	13.95

Fig. 4.52 SEM image and EDS results of the sample machined with graphite-mixed dielectric under the condition of C_p= 4 g/l, I_p= 6 A, T_{on}= 300 μs, τ= 75 % and V_g= 40 V

Element	Weight %
Al	0.16
Si	0.71
Ti	0.86
Cr	23.58
Fe	5.88
Ni	53.85
Nb	4.10
Mo	10.86

Fig. 4.53 SEM image and EDS results of the sample machined with aluminum-mixed dielectric under the condition of C_p= 4 g/l, I_p= 6 A, T_{on}= 300 μs, τ= 75 % and V_g= 40 V

Table 4.16 shows chemical composition of as-received Inconel 625 and that after machining the same material using with and without powder-mixed dielectric under the specified machining conditions. After carefully studying Table 4.16 it is evident that although EDM could not significantly alter chemical composition of Inconel 625, addition of powders resulted in variation in relative content of Nb and Mo at the expense of Ni and Fe. Weight % of Mo consistently increased in case of PMEDM. This might be due to the fact that redistribution of thermal energy due to PMEDM was favorable for realignment of elements like Mo to cause solution strengthening and formation of metal carbides. This

phenomenon prominently contributed to the enhancement of surface microhardness after PMEDM in comparison with conventional EDM as evident from Table 4.14. Rise in content of Nb along with Fe after aluminum-mixed EDM might have promoted formation of δ or laves phase [170,173].

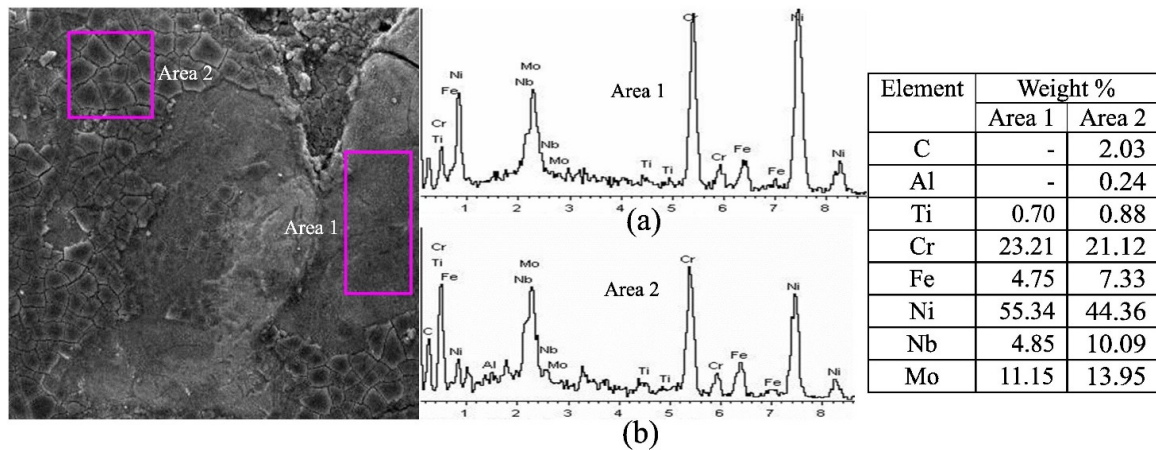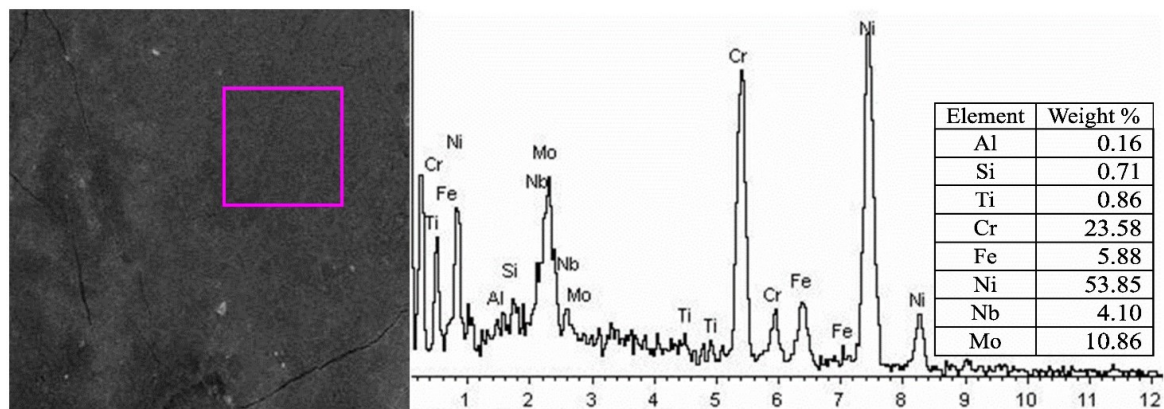| Element	Weight %
Al	0.49
Si	0.21
S	1.19
Ti	0.48
Cr	25.89
Mn	0.54
Fe	6.40
Ni	55.53
Nb	1.82
Mo	7.43
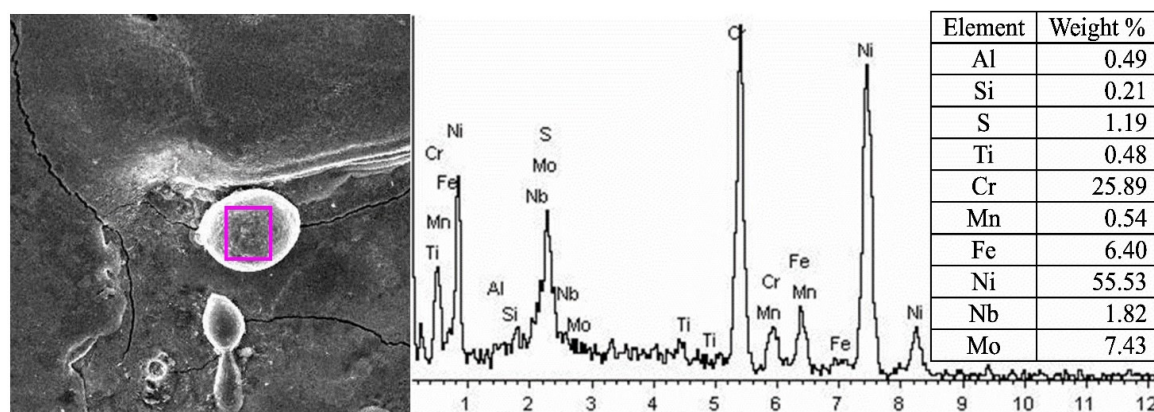
Fig. 4.54 SEM image and EDS results of the sample machined with silicon-mixed dielectric under the condition of C_p= 4 g/l, I_p= 6 A, T_{on}= 300 μs, τ= 75 % and V_g= 40 V

After revealing the bulk information of the machined surface after PMEDM, attempt was also made to reveal to extract information from the selective regions. Such results are presented in, Fig. 4.52, Fig. 4.53 and Fig. 4.54. The investigated light grey region (area 1) in Fig. 4.52 (a) apparently consists of fcc γ matrix which is solid solution strengthened by Cr and Mo according to the EDS result in Fig. 4.52 (b). Interestingly, when the region comprising mainly of γ' precipitates was probed it was revealed there was a hike in % of C, Nb, Mo, Al and Ti at the expense of Ni and Cr. Area 2, therefore, is logically assumed to consist of δ phase, metal carbides apart from γ' phase. Addition of graphite powder to the dielectric was responsible for formation of metal carbides. On the other hand, content of Nb was considerably less for the samples machined with aluminum and silicon powders at the specified locations as indicated in Fig. 4.53 and Fig. 4.54. Any trace of carbon could not also be detected. Therefore, it may be inferred that Nb-rich phase was not present in selected point for aluminum-mixed EDMed sample although it was prevalent at the bulk of the machined surface.

Influence of powder-mixed dielectric on crystallographic orientation of EDMed Inconel 625 has been studied using X-ray diffraction (XRD) technique, the spectra for which are shown in Fig. 4.55. While EDM with conventional (pure) dielectric primarily demonstrated fcc structure of γ-phase of Inconel 625 [174] along with some δ (Ni_3Nb) phase, some additional peaks have been identified when different powders were added. These peaks marked by 'χ and ω' in Fig. 4.55 indicate possible formation of carbides of Ni,

Cr and Mo along with Ni₃Nb (211) from Inconel 625 as confirmed by X'pert High score software.
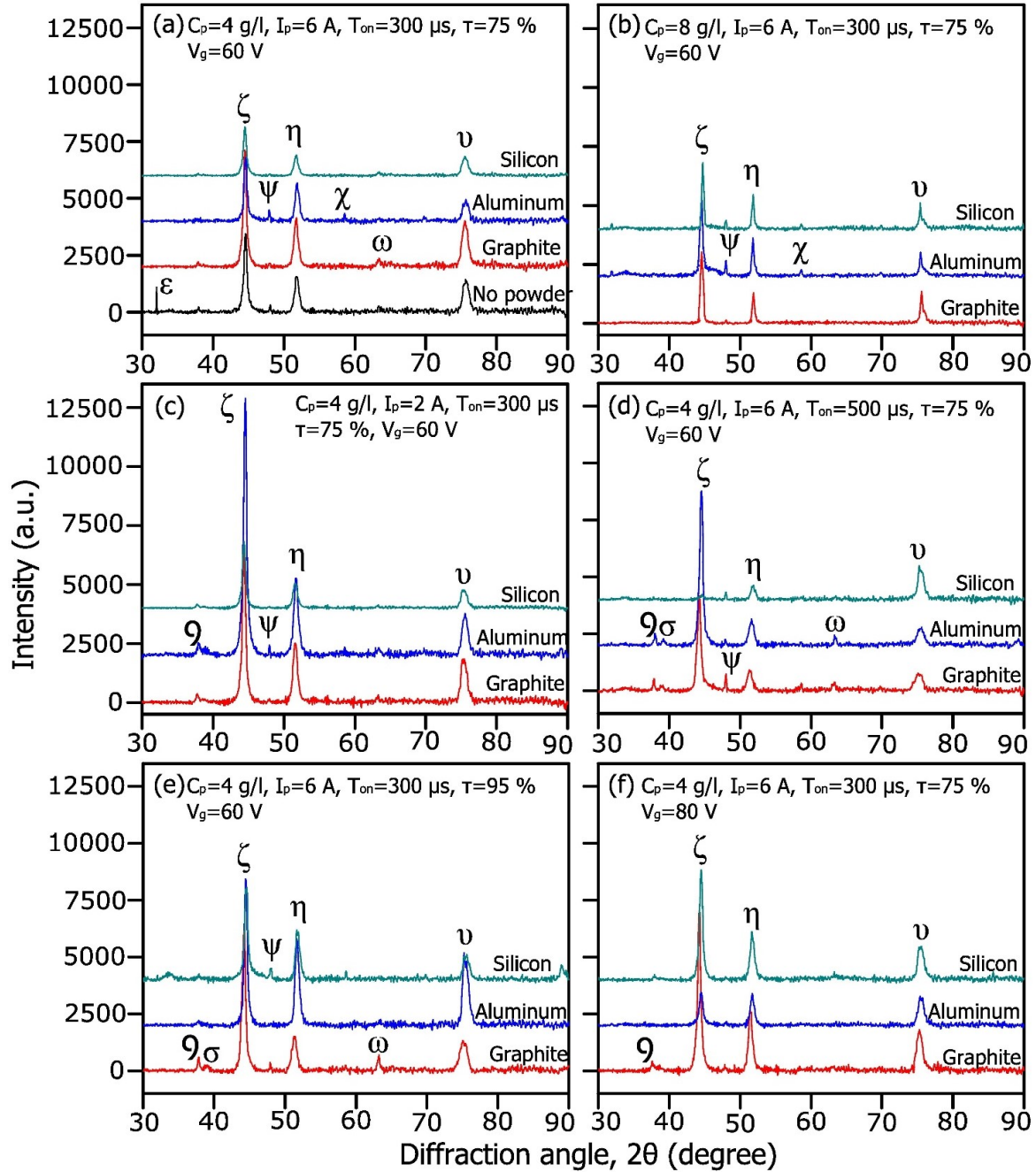
Fig. 4.55 XRD spectra of machined surfaces obtained with and without powder-mixed dielectric under different conditions

The meaning for different symbols used in Fig. 4.55 is provided in Table 4.17. Since kerosene has been used as dielectric, addition of powders caused enhanced degree of ionization as explained earlier which led to more pyrolysis which in turn might have

resulted in breakage of C-H bonds. Hence, more carbon atoms would be available close to the machined surface. These metal carbides might also be responsible for surface hardening effect as evident from Fig. 4.48 to Fig. 4.50. Moreover, addition of powder caused suppression of one of the peaks (around 32°) obtained with conventional EDM without powder. This peak corresponds to Ni_4Mo phase. It has already been observed from EDS results (Table 4.16) that relative content of nickel was reduced at the expense of Nb and Mo after addition of powders like aluminum and graphite. XRD results also corroborate the same.

Table 4.17 Different phases of machined surfaces

Symbols	Miller indices	Possible phase(s)
ζ	(1 1 1)	$AlNi$, Ni_3Fe, Ni_3Nb
η	(2 0 0)	Mo_2C, Ni_3Mo, Ni_3Nb
υ	(2 2 0)	Ni_3Mo, Ni_3Al
ε	(1 1 0)	Ni_4Mo, Cr_3Ni_2
ϱ	(1 1 1)	Mo_2C, Ti_2Ni
σ	(0 0 2)	Ni_3Nb
ψ	(2 0 0)	Ni_3Si_2, Cr_3Ni_2
χ	(3 1 0)	NiC, $Cr_{23}C_6$, Mo_2C
ω	(2 1 1)	Ni_3Nb, $Cr_{23}C_6$, Mo_2C

Two observations have been noted when powder concentration was increased from 4 to 8 g/l. For lower concentration, preferred orientation of Inconel 625 has always been ζ(111) primarily consisting of nickel and its intermetallic phases (e.g. Ni_3Nb).

PMEDM with higher concentration caused prominent increase of η(200) which consists of more content of Mo_2C. This is attributed to availability of more carbon atoms during discharge with elevation in powder concentration as explained before. Comparing Fig. 4.55(a) and (b) it is also evident that higher concentration of silicon promotes the formation of phase indicated by ψ symbol possibly comprising of Ni_3Si_2. It is also interesting to note that higher concentration of powders led to suppression of one of the nickel rich phases symbolized by ω.

Variation of peak current did not cause significant alteration except during PMEDM with aluminum powder which exhibited more prominent phase marked by ϱ consisting of Mo_2C at lower peak current. This signifies influence of aluminum powder is more prominent at lower peak current which when increased almost negated the influence of PMEDM. Increase in pulse-on time clearly facilitated the formation of phase indicated by σ consisting of Ni_3Nb. This is because of increase in relative content of niobium with prolonged pulse duration. Similar observation has also been noted when duty cycle has

been increased. However, no significant alteration in phases could be noticed with change in gap voltage.
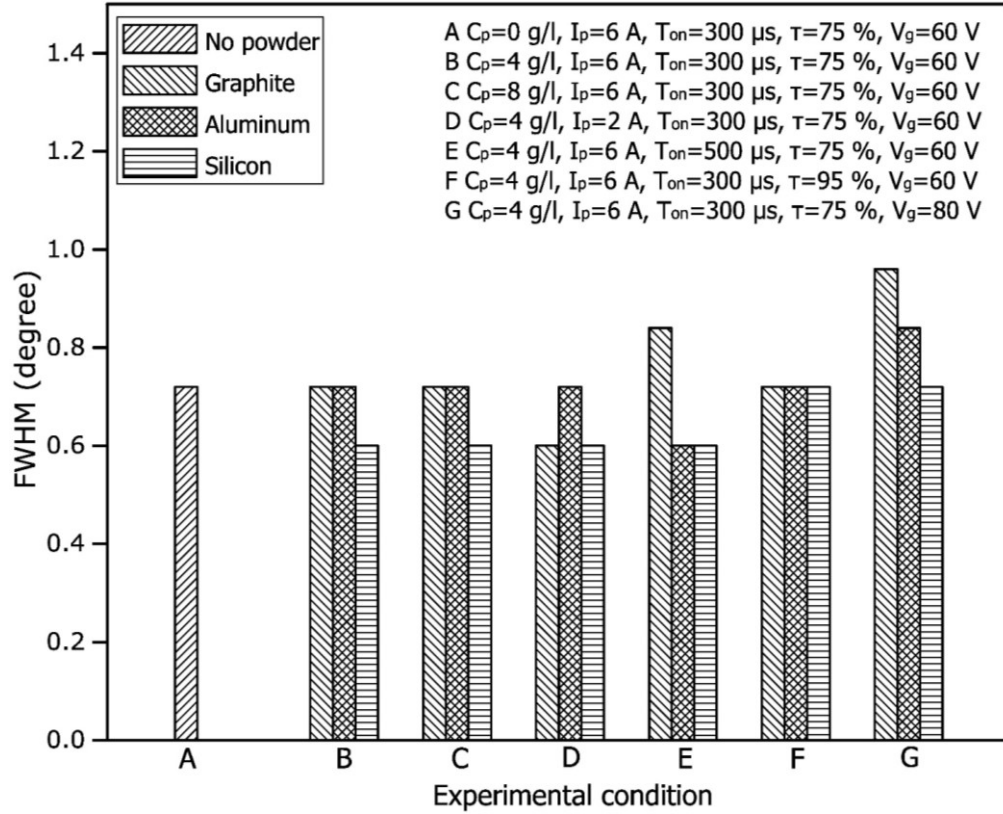
Fig. 4.56 FWHM obtained with and without powder-mixed dielectric under different conditions

XRD spectra indicate that there is hardly any significant shifting of peaks while comparing EDM and PMEDM with different powders. Fig. 4.56 shows FWHM for different samples. While PMEDM with aluminum and graphite powders could not bring in any significant modification compared to conventional EDM, slight reduction in FWHM was observed with silicon powder. This is attributed to possible increase in grain size due to addition of silicon with dielectric. Lower thermal conductivity of silicon could not effectively carry away heat from the machining zone resulting net thermal energy on the workpiece surface to increase. This phenomenon might have led to grain growth. On the other hand, parameters such as concentration, peak current and pulse-on time could not significantly alter the FWHM when silicon powder was used. Owing to its very high electrical resistivity breaking down of dielectric molecules would be hindered. As a consequence change in discharge parameters in the selected range could hardly modify FWHM. However, when duty cycle and gap voltage were increased there was hardly any change in FWHM value when silicon powder has been added. FWHM obtained from XRD

results also indicates that graphite powder is the most susceptible to alteration in PMEDM condition. Pronounced increase in FWHM has been noted when different parameters such as I_p, T_{on}, τ and V_g were increased. The rise in FWHM is indicative of refinement of grains of Inconel 625 because of the fact that graphite has the highest heat of fusion (117 kJ/mol). This property enables graphite to retain more heat energy leaving less thermal energy available on the workpiece surface. Thus possibility of grain growth would be restricted for graphite powder. Effective mixing with dielectric due to its low density also helps graphite enhance cooling ability of dielectric. As a result grain refinement takes place.

A C_p=0 g/l, I_p=6 A, T_{on}=300 μs, τ=75 %, V_g=60 V
B C_p=4 g/l, I_p=6 A, T_{on}=300 μs, τ=75 %, V_g=60 V
C C_p=8 g/l, I_p=6 A, T_{on}=300 μs, τ=75 %, V_g=60 V
D C_p=4 g/l, I_p=2 A, T_{on}=300 μs, τ=75 %, V_g=60 V
E C_p=4 g/l, I_p=6 A, T_{on}=500 μs, τ=75 %, V_g=60 V
F C_p=4 g/l, I_p=6 A, T_{on}=300 μs, τ=95 %, V_g=60 V
G C_p=4 g/l, I_p=6 A, T_{on}=300 μs, τ=75 %, V_g=80 V
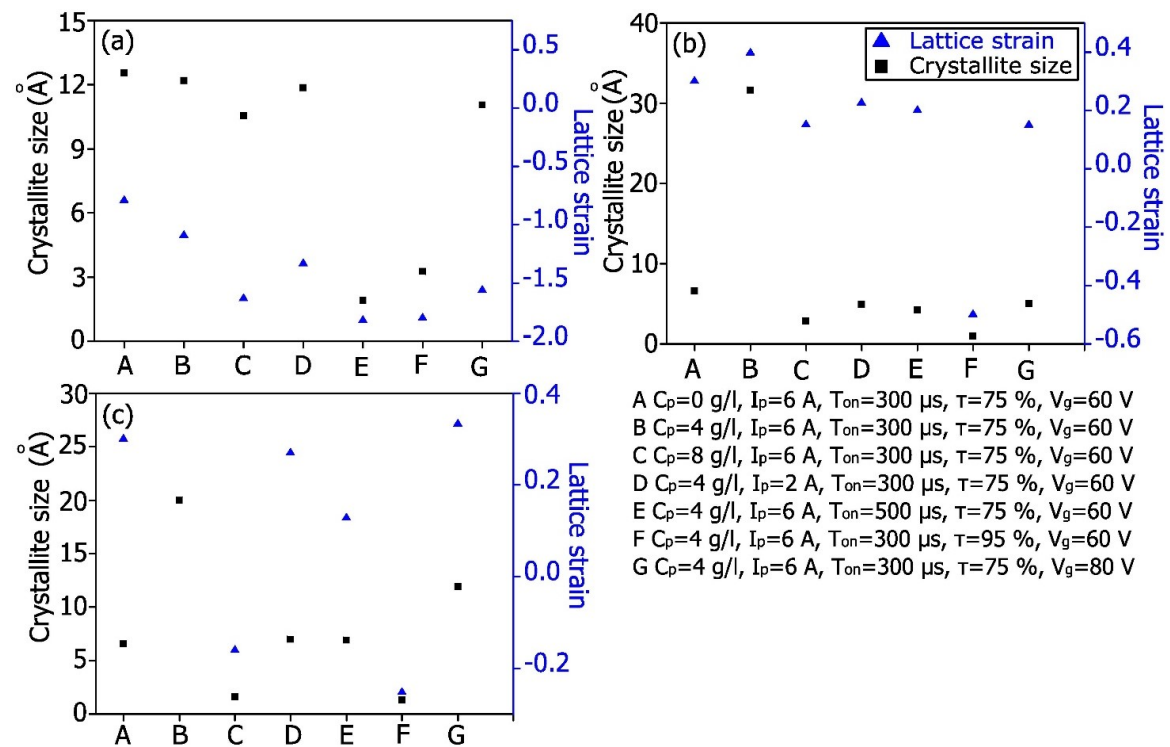
Fig. 4.57 Crystallite size and lattice strain obtained using conventional EDM and (a) graphite (b) aluminum (c) silicon powders

Crystallite size and lattice strain of Inconel 625 after EDM with and without powder have been obtained using linear Williamson-Hall plot. This technique has the capability to segregate the influence of crystallite size and lattice strain on FWHM [175]. These two characteristics have considerable impact on overall microstructure of material and hence it should be studied. Crystallite size and lattice strain for different powders under varying machining condition have been presented in Fig. 4.57.

It is evident from Fig. 4.57 that addition of powder with dielectric caused reduction in crystallite size as well as lattice strain. This may be explained by the fact that powder-mixed

dielectric ensures enlargement of crater while maintaining uniform discharge over a large area.

It is also important to note pulse duration and duty cycle have contributed significantly to decrease crystallite size for all the powders. Careful consideration of Fig. 4.57 also indicates material of powder also has some influence. Crystallite size varied in the range of around 2 to 7.5 Å. While for the other two powders crystallite size varied in the similar range, exception was found when high peak current of 6 A was considered. Sudden rise of crystallite size more than 30 Aº for aluminum powder could be ascribed to very low heat of fusion (10.79 kJ/mol) in combination with its tendency to agglomerate leading to the condition of arcing under high peak current. Similar observation has also been noted for silicon powder. But crystallite size under same condition was less compared to that for aluminum powder (~20 Å). This is due to higher heat of fusion than aluminum. Higher thermal energy under such condition caused grain growth for both these powders. Lower thermal conductivity of silicon powder is also one of the reasons. On the other hand, graphite has the highest heat of fusion among all apart from high thermal conductivity. This helps the powder retain sizable amount of heat leaving net thermal energy on the work surface. As a result grain growth could be restricted. Similar observation has also been noticed for lattice strain.

4.3.7 Residual stress

High energy sparking in EDM develops extreme temperature differences in the machined surface layers. During rapid cooling process, tensile residual stress develops on the EDMed surface [176]. Cracks are formed when this tensile residual stress exceeds the fracture strength of the material. Fig. 4.58 shows the residual stress plots of the machined surfaces under different machining conditions. High tensile residual stress (Fig. 4.58A) was observed for the sample machined with pure kerosene due to high discharge energy density. The tensile stress got reduced (Fig. 4.58B and Fig. 4.58C) with the addition of different powders to the dielectric as the added powder results in low discharge energy density due to spark gap enlargement.

Little consideration would indicate that tensile residual stress is minimum for silicon powder throughout. Silicon owing to its high heat of fusion and thermal conductivity has the capability retain heat energy and dissipates it efficiently by virtue of its high thermal conductivity. The abrasive action of silicon particles on the crater ridges also augments the reduction of tensile residual stress. As a consequence, tensile residual stress could be restricted. Although, aluminum also possesses high thermal conductivity, due to its lower heat of fusion tensile stress is more than for silicon and graphite powders in general.

109

Further, agglomeration of aluminum at higher concentration (8 g/l) led to the possibility of arcing. Similarly, under the condition of highest duty cycle (95 %), similar condition might have prevailed. Therefore, tensile stress was the highest for aluminum powder under such situations.

The tensile stress also reduced when current reduced from 6 A to 2 A (Fig. 4.58D) due to the reduction in discharge energy. At high pulse-on time of 500 μs the stress declined (Fig. 4.58E) because of the reduction in energy density due to discharge passage expansion. For the same reason low tensile residual stress (Fig. 4.58F) was realized with the increase in duty cycle. A fall in tensile stress was observed (Fig. 4.58G) with the increase in gap voltage. This is attributed to the reduction in energy density due to the enlargement of discharge column with the gap voltage.

Due to the formation of inter metallic phases like Ni_3Nb as evident in Fig. 4.55, the superior mechanical properties in the form of higher hardness and rupture strength will be achieved. As a result, the machined component would have greater resistance to indentation, crack propagation and rupture. This would be possible only when surface tensile strength reduces. Decrease in surface residual stress is also manifested in the reduction in SCD which is shown in Fig. 4.31 to Fig. 4.33.
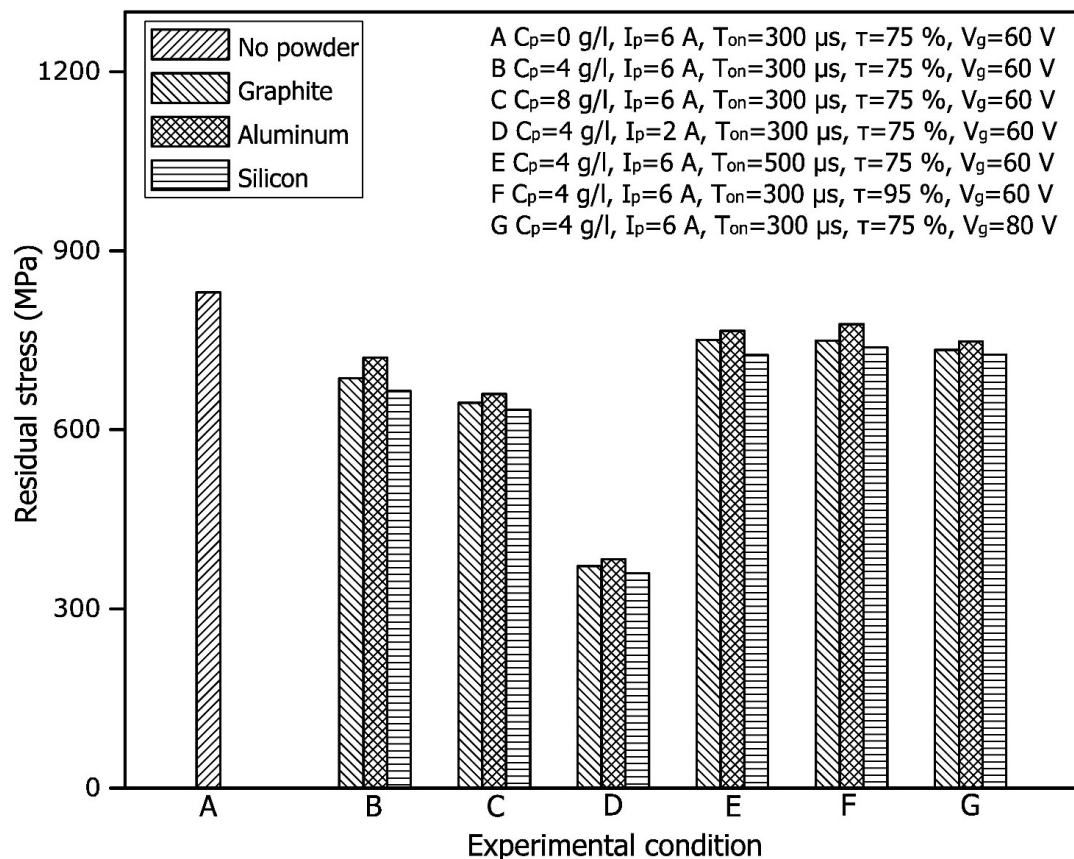
Fig. 4.58 Residual stress with and without powder-mixed dielectric under different conditions

From Table 4.18, it is observed that the experimental tensile residual stress values and predicted thermal residual stress values obtained using numerical modelling for different powder materials follow the same trend. However, the predicted values were slightly higher than the experimental values, as the mechanical aspects such as compressive pressure and abrasive action of the powder particles on craters during PMEDM process were not considered during modelling.

Table 4.18 Comparison of experimental and predicted residual stress under different machining conditions

Experimental condition	Experimental residual stress	Predicted thermal residual stress	% error
Graphite mixed-dielectric			
I_p=6 A, T_{on}=300 μs, τ=75 %, V_g=40 V	686	810	18.08
I_p=2 A, T_{on}=300 μs, τ=75 %, V_g=40 V	372	436	17.2
I_p=6 A, T_{on}=500 μs, τ=75 %, V_g=40 V	751	874	16.38
I_p=6 A, T_{on}=300 μs, τ=95 %, V_g=40 V	749	834	11.35
I_p=6 A, T_{on}=300 μs, τ=75 %, V_g=80 V	734	822	11.99
Aluminum mixed-dielectric			
I_p=6 A, T_{on}=300 μs, τ=75 %, V_g=40 V	721	782	8.46
I_p=2 A, T_{on}=300 μs, τ=75 %, V_g=40 V	383	417	8.88
I_p=6 A, T_{on}=500 μs, τ=75 %, V_g=40 V	766	842	9.92
I_p=6 A, T_{on}=300 μs, τ=95 %, V_g=40 V	777	806	3.73
I_p=6 A, T_{on}=300 μs, τ=75 %, V_g=80 V	748	790	5.61
Silicon-mixed dielectric			
I_p=6 A, T_{on}=300 μs, τ=75 %, V_g=40 V	665	743	11.73
I_p=2 A, T_{on}=300 μs, τ=75 %, V_g=40 V	360	384	6.67
I_p=6 A, T_{on}=500 μs, τ=75 %, V_g=40 V	725	829	14.34
I_p=6 A, T_{on}=300 μs, τ=95 %, V_g=40 V	738	767	3.93
I_p=6 A, T_{on}=300 μs, τ=75 %, V_g=80 V	726	756	4.13

Chapter 5
Conclusions, major contributions and future scope of work

5.1 Conclusions

In the current research work, the effect of various powder-mixed EDM (PMEDM) process parameters was first numerically modeled on temperature distribution, MRR and residual stress considering Inconel 625 as workpiece material. After gaining initial information on the influence of different powders (graphite, aluminum and silicon) on the process, experimental investigation was carried out according to RSM-based design of experiment. MRR and ROC which are the measures of productivity and dimensional accuracy respectively were first studied followed by various aspects of surface integrity. Comparative evaluation of all the process characteristics was made considering all the three powder materials. Additionally, influence of various process parameters was also investigated. Results clearly demonstrated remarkable improvement in terms of various performance measures for PMEDM compared to EDM without powder additives. However, such improvement is dependent on characteristics of powder materials and their concentration. The following major conclusions obtained from the entire work can be drawn:

(a) Modelling of PMEDM process

1. The predicted MRR values obtained for all three powder-mixed dielectrics were very close to each other. Careful observation would indicate that aluminum has produced highest MRR followed by graphite and silicon within the considered process parameter range.
2. Among, the three powders, silicon has produced least thermal residual stress followed by aluminum and graphite due to the raise in predicted temperatures.

(b) Effect of PMEDM on MRR and ROC

1. Although indicated particle size was same for all the three powders (~15 μm), detailed study utilizing SEM, particle size analysis, and XRD clearly pointed out variation in average particle size. Aluminum exhibited largest agglomeration while maximum volume % of finest particles was observed with graphite powder. Presence of small quantities of impurities such as SiO_2 and Al_2O_3 in as-received Si and Al powders was also ascertained.

2. For low levels of powder concentration (up to 6 g/l), Al powder is recommended for achieving high material removal rate. However, agglomeration of Al powder at high concentration (8 g/l) led to short-circuiting and arcing. Thus, at 8 g/l powder concentration graphite powder produced the highest material removal rate.

3. Least radial overcut was attained in conventional EDM process. Among the powder-mixed dielectrics, Si powder impregnated dielectric produced the least radial overcut followed by graphite and aluminum.

(c) Effect of PMEDM on surface integrity

1. For all the three powder-mixed dielectrics, larger and shallower craters were observed compared to coneventional EDM due to enhanced conductivity of dielectric which causes spark generation from a long distance.

2. Conventional EDM exhibited largest number of surface cracks while, PMEDM is effective in minimizing the same. Graphite is suggested for minimizing the number of surface cracks, followed by Si and Al powders.

3. Si powder is suggested for achieving good surface finish followed by Al. Smaller size and the abrasive action of Si powder on crater edges also contributed to improvement of surface finish. However, at higher powder concentrations (above 4 g/l), graphite powder produced superior surface finish compared to Al powder.

4. PMEDM has resulted in thinner altered layer compared to conventional EDM (no powder). Among the three powders, graphite resulted in the least ALT followed by aluminum and silicon.

5. Si powder is recommended for achieving high microhardness of the machined surface followed by aluminum and graphite. Crater diameter increased with the addition of powder materials. Al produced the largest crater diameter followed by graphite and Si.

6. Microhardness in sub-surface regions was higher using pure dielectric compared to powder-mixed dielectric. Among the three powders, graphite resulted in the least cross-sectional microhardness followed by aluminum and silicon.

7. Precipitation of γ' phases from matrix of γ phase is promoted due to EDM process. It is an intermetallic phase consisting mainly of $Ni_3(Al,Ti)$ which hinders dislocation movement and hence improves hardness creep resistance of the alloy.

8. Relative content of nickel was reduced at the expense of Nb and Mo after addition of powders like aluminum and graphite in dielectric during EDM.

9. While EDM with conventional dielectric primarily demonstrated fcc structure of γ-phase of Inconel 625 along with some $\delta(Ni_3Nb)$ phase, PMEDM has promoted formation of carbides of Ni, Cr and Mo along with Ni_3Nb from Inconel 625.

Overall, graphite may be recommended for achieving high material removal rate, less surface cracks, thin altered layer, less microhardness at surface and sub-surface regions whereas silicon may yield low radial overcut, low surface roughness and less residual stress. Aluminum yielded high material removal rate at low concentration range (upto 6 g/l).

5.2 Major contribution

Following studies have been carried out for the first time which are considered as major contribution of current research work.

1. Modelling and simulation of PMEDM process of nickel-based super alloy have been carried out for understanding the underlining mechanism.

2. Role of PMEDM process on a nickel-based super alloy has been clearly established.

3. Role of powder material properties, their concentration on surface integrity aspects has been ascertained. It is significant as surface integrity dictates the functional performance of the machined component.

4. Recommendation has been made on selection of powder materials, their concentration and other PMEDM parameters considering various performance characteristics.

The outcome of the present work therefore, is of considerable significance for the researchers working in the field of EDM and the pertinent industries including aerospace, marine and chemical industries.

5.3 Future scope of work

1. Modelling and simulation can be extended for different aspects of surface integrity such as surface roughness, altered layer thickness and crack formation.

2. Optimal parameter settings for achieving optimal responses can be carried out for individual powders using suitable optimization technique.

3. Influence of nano powders on the PMEDM processing of nickel-based super alloys (Inconel 625 in particular) can be investigated in comparison with PMEDM using micro powders.

References

[1]   V.K. Jain, Advanced machining processes, Allied Publishers, New Delhi, 2009.

[2]   K.H. Ho, S.T. Newman, State of the art electrical discharge machining (EDM), Int. J. Mach. Tools Manuf. 43 (2003) 1287–1300.

[3]   G. Boothroyd, A.K. Winston, Fundamentals of Machining and Machine Tools, CRC Press, Taylor & Francis Group, Boca Raton, 1989.

[4]   M. Barash, Some properties of spark eroded surfaces, Microtecnic. 13 (1959) 51–54.

[5]   F. Wang, Y. Liu, Z. Chen, R. Ji, X. Tian, Z. Liu, Design of Three-axis ED Milling Machine Based on the PMAC Motion Card, J. Comput. 7 (2012) 2496–2502.

[6]   K.P. Rajurkar, Z. Yu, 3D micro-EDM using CAD/CAM, CIRP Ann. - Manuf. Technol. 49 (2000) 127–130.

[7]   B. Mohan, A. Rajadurai, K.G. Satyanarayana, Electric discharge machining of Al–SiC metal matrix composites using rotary tube electrode, J. Mater. Process. Technol. 153-154 (2004) 978–985.

[8]   J.S. Joshi, G. Chakraverti, Performance Evaluation of Rotary EDM by Experimental design Technique, Def. Sci. J. 47 (2013) 65–73.

[9]   Z.N. Guo, T.C. Lee, T.M. Yue, W.S. Lau, A study of ultrasonic-aided wire electrical discharge machining, J. Mater. Process. Technol. 63 (1997) 823–828.

[10] J.H. Zhang, T.C. Lee, W.S. Lau, X. Ai, Spark erosion with ultrasonic frequency, J. Mater. Process. Technol. 68 (1997) 83–88.

[11] M. Ghoreishi, J. Atkinson, A comparative experimental study of machining characteristics in vibratory, rotary and vibro-rotary electro-discharge machining, J. Mater. Process. Technol. 120 (2002) 374–384.

[12] K. Egashira, T. Masuzawa, Microultrasonic Machining by the Application of Workpiece Vibration, CIRP Ann. - Manuf. Technol. 48 (1999) 131–134.

[13] C. Gao, Z. Liu, A study of ultrasonically aided micro-electrical-discharge machining by the application of workpiece vibration, J. Mater. Process. Technol. 139 (2003) 226–228.

[14] G.S. Prihandana, M. Hamdi, Y.S. Wong, K. Mitsui, Effect of vibrated electrode in electrical discharge machining, in: Proc. First Int. Conf. Seventh AUN/SEED-Net Fieldwise Semin. Manuf. Mater. Process., Kuala Lumpur, 2006: pp. 133–138.

[15] V. Ramani, M.L. Cassidenti, Inert-Gas Electrical Discharge Machining, Huntsville, AL, United States, 1985.

[16] J. Tao, A.J. Shih, J. Ni, Experimental Study of the Dry and Near-Dry Electrical Discharge Milling Processes, J. Manuf. Sci. Eng. 130 (2008) 011002.

[17] S.K. Saha, S.K. Choudhury, Experimental investigation and empirical modeling of the dry electric discharge machining process, Int. J. Mach. Tools Manuf. 49 (2009) 297–308.

[18] M. Kunieda, M. Yoshida, N. Taniguchi, Electrical Discharge Machining in Gas, CIRP Ann. - Manuf. Technol. 46 (1997) 143–146.

[19] W.S. Zhao, Q.G. Meng, Z.L. Wang, The application of research on powder mixed

EDM in rough machining, J. Mater. Process. Technol. 129 (2002) 30–33.

[20] Z.Z. Lu, F.L. Zhao, Y.Y. Yang, Research on dielectric breakdown and discharge channel in powder-mixed EDM, Dalian Ligong Daxue Xuebao/Journal Dalian Univ. Technol. 48 (2008) 373–377.

[21] G.S. Prihandana, M. Mahardika, M. Hamdi, Y.S. Wong, K. Mitsui, Accuracy improvement in nanographite powder-suspended dielectric fluid for micro-electrical discharge machining processes, Int. J. Adv. Manuf. Technol. 56 (2011) 143–149.

[22] F.L. Zhao, Z.Z. Lu, H. Wang, Z.Q. Qian, Research on effecting mechanism of particles in powder-mixed EDM, Dalian Ligong Daxue Xuebao/Journal Dalian Univ. Technol. 45 (2005) 668–671.

[23] H.M. Chow, L.D. Yang, C.T. Lin, Y.F. Chen, The use of SiC powder in water as dielectric for micro-slit EDM machining, J. Mater. Process. Technol. 195 (2008) 160–170.

[24] K.Y. Kung, J.T. Horng, K.T. Chiang, Material removal rate and electrode wear ratio study on the powder mixed electrical discharge machining of cobalt-bonded tungsten carbide, Int. J. Adv. Manuf. Technol. 40 (2009) 95–104.

[25] A. Erden, S. Bilgin, Role of Impurities in Electric Discharge Machining, in: 21st Mach. Tool Des. Res. Conf., Swansea, 1980: pp. 345–350.

[26] Silicon Powder Additives Proven Safe And Effective In EDM, Mod. Mach. Shop. (2000). http://www.mmsonline.com/articles/silicon-powder-additives-proven-safe-and-effective-in-edm.

[27] M.P. Jahan, M. Rahman, Y.S. Wong, Modelling and experimental investigation on the effect of nanopowder-mixed dielectric in micro-electrodischarge machining of tungsten carbide, Proc. Inst. Mech. Eng. Part B J. Eng. Manuf. 224 (2010) 1725–1739.

[28] A. Bhattacharya, A. Batish, N. Kumar, Surface characterization and material migration during surface modification of die steels with silicon, graphite and tungsten powder in EDM process, J. Mech. Sci. Technol. 27 (2013) 133–140.

[29] T.Y. Fong, F.C. Chen, Investigation into some surface characteristics of electrical discharge machined SKD-11 using powder-suspension dielectric oil, J. Mater. Process. Technol. 170 (2005) 385–391.

[30] B. Jabbaripour, M.H. Sadeghi, M.R. Shabgard, H. Faraji, Investigating surface roughness, material removal rate and corrosion resistance in PMEDM of r-TiAl intermetallic, J. Manuf. Process. 15 (2013) 158–166.

[31] F.Q. Hu, F.Y. Cao, B.Y. Song, P.J. Hou, Y. Zhang, K. Chen, et al., Surface properties of SiCp/Al composite by powder-mixed EDM, in: Procedia CIRP-The Seventeenth CIRP Conf. Electro Phys. Chem. Mach., 2013: pp. 101–106.

[32] Q.Y. Ming, L.Y. He, Powder-suspension dielectric fluid for EDM, J. Mater. Process. Technol. 52 (1995) 44–54.

[33] A. Kumar, S. Maheshwari, C. Sharma, N. Beri, Analysis of Machining Characteristics in Additive Mixed Electric Discharge Machining of Nickel-Based Super Alloy Inconel 718, Mater. Manuf. Process. 26 (2011) 1011–1018.

[34] S. Singh, M.F. Yeh, Optimization of Abrasive Powder Mixed EDM of Aluminum Matrix Composites with Multiple Responses Using Gray Relational Analysis, J. Mater. Eng. Perform. 21 (2012) 481–491.

[35] K.H. Syed, P. Kuppan, Studies on Recast-layer in EDM using Aluminium Powder Mixed Distilled Water Dielectric Fluid, Int. J. Eng. Technol. 5 (2013) 1775–1780.

[36] Y.F. Tzeng, C.Y. Lee, Effects of Powder Characteristics on Electrodischarge Machining Efficiency, Int. J. Adv. Manuf. Technol. 17 (2001) 586–592.

[37] Y.S. Wong, L.C. Lim, I. Rahuman, W.M. Tee, Near-mirror-finish phenomenon in EDM using powder-mixed dielectric, J. Mater. Process. Technol. 79 (1998) 30–40.

[38] H.M. Chow, B.H. Yan, F.Y. Huang, J.C. Hung, Study of added powder in kerosene for the micro-slit machining of titanium alloy using electro-discharge machining, J. Mater. Process. Technol. 101 (2000) 95–103.

[39] F. Klocke, D. Lung, G. Antonoglou, D. Thomaidis, The effects of powder suspended dielectrics on the thermal influenced zone by electrodischarge machining with small discharge energies, J. Mater. Process. Technol. 149 (2004) 191–197.

[40] K.L. Wu, B.H. Yan, F.Y. Huang, S.C. Chen, Improvement of surface finish on SKD steel using electro-discharge machining with aluminum and surfactant added dielectric, Int. J. Mach. Tools Manuf. 45 (2005) 1195–1201.

[41] Y.F. Tzeng, F.C. Chen, Multi-objective optimisation of high-speed electrical discharge machining process using a Taguchi fuzzy-based approach, Mater. Des. 28 (2007) 1159–1168.

[42] F. Hu, H. Zhang, W. Zhao, Z. Wang, D. Hu, Y. Yu, Surface properties of 3000°c high melting point material by powder mixed EDM, in: Key Eng. Mater., 2008: pp. 143–147.

[43] Y.G. Wang, F.L. Zhao, Simulation of Particles' Activity in Discharge Channel of PMEDM, Appl. Mech. Mater. 10-12 (2008) 297–302.

[44] Y.Y. Tsai, C.K. Chang, An Investigation into Surface Roughness of EDM Using Soft Particles Suspension in Silicone Oil, Key Eng. Mater. 389-390 (2009) 430–435.

[45] A. Batish, A. Bhattacharya, Mechanism of Material Deposition from Powder, Electrode and Dielectric for Surface Modification of H11 and H13 Die Steels in EDM Process, Mater. Sci. Forum. 701 (2012) 61–75.

[46] A. Bhattacharya, A. Batish, Effect of process variables on microhardness, grain size and strain during machining of various die steels with powder-mixed electric-discharge machining using dummy treated experimental design, Proc. Inst. Mech. Eng. Part B J. Eng. Manuf. 226 (2012) 1192–1204.

[47] A. Bhattacharya, A. Batish, G. Singh, V.K. Singla, Optimal parameter settings for rough and finish machining of die steels in powder-mixed EDM, Int. J. Adv. Manuf. Technol. 61 (2012) 537–548.

[48] C. Mai, H. Hocheng, S. Huang, Advantages of carbon nanotubes in electrical discharge machining, Int. J. Adv. Manuf. Technol. 59 (2012) 111–117.

[49] K.H. Syed, K. Palaniyandi, Performance of electrical discharge machining using aluminium, Turkish J. Eng. Environ. Sci. 36 (2012) 195–207.

[50] A.A. Aliyu, H. Musa, J.M. Rohani, Parametric Study of Powder Mixed Electrical Discharge Machining and Mathematical Modeling of SiSiC Using Copper Electrode, Adv. Mater. Res. 845 (2013) 878–882.

[51] K.H. Syed, G.P. Anuraag, G. Hemanth, S.A. Subahan, Studies on surface roughness of Al-SiC composites machined by powder-mixed EDM, Int. J. Appl. Eng. Res. 9 (2014) 11067–11077.

[52] G. Talla, S. Gangopadhyay, C.K. Biswas, Multi Response Optimization of Powder Mixed Electric Discharge Machining of Aluminum/Alumina Metal Matrix Composite Using Grey Relation Analysis, Procedia Mater. Sci. 5 (2014) 1633–1639.

[53] Y.Y. Tsai, C.H. Tseng, C.K. Chang, Development of a combined machining method using electrorheological fluids for EDM, J. Mater. Process. Technol. 201 (2008) 565–569.

[54] S. Assarzadeh, M. Ghoreishi, M. Shariyyat, Response surface methodology approach to process modeling and optimization of Powder Mixed Electrical Discharge Machining (PMEDM), in: 16th Int. Symp. Electromachining, ISEM 2010, Shanghai Jiaotong University Press, 2010: pp. 181–186.

[55] Y.Y. Tsai, C.K. Chang, Effects of Polymer Particles Suspending in Dielectric Fluid on Surface Roughness of EDM, Adv. Mater. Res. 97-101 (2010) 4146–4149.

[56] A.A. Khan, M.B. Ndaliman, Z.M. Zain, M.F. Jamaludin, U. Patthi, Surface Modification Using Electric Discharge Machining (EDM) with Powder Addition, Appl. Mech. Mater. 110-116 (2011) 725–733.

[57] S. Assarzadeh, M. Ghoreishi, A dual response surface-desirability approach to process modeling and optimization of Al2O3 powder-mixed electrical discharge machining (PMEDM) parameters, Int. J. Adv. Manuf. Technol. 64 (2012) 1459–1477.

[58] G. Kibria, B.R. Sarkar, B.B. Pradhan, B. Bhattacharyya, Comparative study of different dielectrics for micro-EDM performance during microhole machining of Ti-6Al-4V alloy, Int. J. Adv. Manuf. Technol. 48 (2010) 557–570.

[59] G. Kibria, B. Bhattacharyya, Investigation into micro-hole geometrical accuracy during micro-EDM of Ti-6Al-4V employing different dielectrics, Int. J. Mach. Mach. Mater. 10 (2011) 310.

[60] G. Kibria, B. Bhattacharyya, F. Chinesta, Y. Chastel, M. El Mansori, Analysis on Geometrical Accuracy of Microhole during Micro-EDM of Ti-6Al-4V using Different Dielectrics, in: AIP Conf. Proc., 2011: pp. 155–160.

[61] M. Kolli, A. Kumar, Parametric Optimization of Boron Carbide Powder Added Electrical Discharge Machining of Titanium Alloy, Appl. Mech. Mater. 592-594 (2014) 678–683.

[62] S. Prabhu, B.K. Vinayagam, Effect of graphite electrode material on EDM of AISI D2 tool steel with multiwall carbon nanotube using regression analysis, Int. J. Eng. Stud. 1 (2009) 93–104.

[63] S. Prabhu, B.K. Vinayagam, Analysis of Surface Characteristics of AISI D2 Tool Steel Material Using Electric Discharge Machining Process with Single Wall Carbon Nano Tubes, Int. J. Eng. Technol. 2 (2010) 35–41.

[64] S. Prabhu, B.K. Vinayagam, Development of empirical model for surface roughness during electrical discharge machining using single wall carbon nanotubes, Int. J. Comput. Mater. Sci. Surf. Eng. 4 (2011) 23–36.

[65] S. Prabhu, B.K. Vinayagam, AFM surface investigation of Inconel 825 with multi wall carbon nano tube in electrical discharge machining process using Taguchi analysis, Arch. Civ. Mech. Eng. 11 (2011) 149–170.

[66] S. Izman, D. Ghodsiyeh, T. Hamed, R. Rosliza, M. Rezazadeh, Effects of Adding Multiwalled Carbon Nanotube into Dielectric when EDMing Titanium Alloy, Adv.

Mater. Res. 463-464 (2012) 1445–1449.

[67] S. Prabhu, B.K. Vinayagam, Modeling the machining parameters of AISI D2 tool steel material with multi wall carbon nano tube in electrical discharge machining process using response surface methodology, Int. J. Phys. Sci. 7 (2012) 297–305.

[68] M.M. Sari, M.Y. Noordin, E. Brusa, Evaluating the electrical discharge machining (EDM) parameters with using carbon nanotubes, IOP Conf. Ser. Mater. Sci. Eng. 40 (2012) 012019.

[69] S. Prabhu, M. Uma, B.K. Vinayagam, Adaptive neuro-fuzzy interference system modelling of carbon nanotube-based electrical discharge machining process, J. Brazilian Soc. Mech. Sci. Eng. 35 (2013) 505–516.

[70] S. Prabhu, B.K. Vinayagam, AFM Nano Analysis of Inconel 825 with Single Wall Carbon Nano Tube in Die Sinking EDM Process Using Taguchi Analysis, Arab. J. Sci. Eng. 38 (2013) 1599–1613.

[71] S. Prabhu, B.K. Vinayagam, Multi objective optimisation of SWCNT - based electrical discharge machining process using grey relational and fuzzy logic analysis, Int. J. Mach. Mach. Mater. 13 (2013) 439–463.

[72] Y.F. Tzeng, F.C. Chen, A simple approach for robust design of high-speed electrical-discharge machining technology, Int. J. Mach. Tools Manuf. 43 (2003) 217–227.

[73] R.K. Garg, K. Ojha, Parametric Optimization of PMEDM Process with Chromium Powder Suspended Dielectric for Minimum Surface Roughness and Maximum MRR, Adv. Mater. Res. 383-390 (2012) 3202–3206.

[74] K. Ojha, R.K. Garg, K.K. Singh, Effect of chromium powder suspended dielectric on surface roughness in PMEDM process, Tribol. - Mater. Surfaces Interfaces. 5 (2011) 165–171.

[75] R.K. Garg, K. Ojha, Parametric Optimization of PMEDM Process with Chromium Powder Suspended Dielectric for Triangular Electrodes, Adv. Mater. Res. 816-817 (2013) 23–27.

[76] A. Bhattacharya, A. Batish, G. Singh, Surface Modification of High Carbon High Chromium, EN31 and Hot Die Steel Using Powder Mixed EDM Process, Mater. Sci. Forum. 701 (2011) 43–59.

[77] A. Bhattacharya, A. Batish, G. Singh, Optimization of powder mixed electric discharge machining using dummy treated experimental design with analytic hierarchy process, Proc. Inst. Mech. Eng. Part B J. Eng. Manuf. 226 (2012) 103–116.

[78] S.S. Sidhu, A. Batish, S. Kumar, Study of Surface Properties in Particulate-Reinforced Metal Matrix Composites (MMCs) Using Powder-Mixed Electrical Discharge Machining (EDM), Mater. Manuf. Process. 29 (2014) 46–52.

[79] M.L. Jeswani, Effect of the addition of graphite powder to kerosene used as the dielectric fluid in electrical discharge machining, Wear. 70 (1981) 133–139.

[80] H.K. Kansal, S. Singh, P. Kumar, Application of Taguchi method for optimisation of powder mixed electrical discharge machining, Int. J. Manuf. Technol. Manag. 7 (2005) 329.

[81] C. Cogun, B. Ozerkan, T. Karacay, An experimental investigation on the effect of powder mixed dielectric on machining performance in electric discharge machining, Proc. Inst. Mech. Eng. Part B J. Eng. Manuf. 220 (2006) 1035–1050.

[82] H.K. Kansal, S. Singh, P. Kumar, Numerical simulation of powder mixed electric discharge machining (PMEDM) using finite element method, Math. Comput. Model. 47 (2008) 1217–1237.

[83] M.P. Jahan, M.M. Anwar, Y.S. Wong, M. Rahman, Nanofinishing of hard materials using micro-electrodischarge machining, Proc. Inst. Mech. Eng. Part B J. Eng. Manuf. 223 (2009) 1127–1142.

[84] G. Kucukturk, C. Cogun, A New Method for Machining of Electrically Nonconductive Workpieces Using Electric Discharge Machining Technique, Mach. Sci. Technol. 14 (2010) 189–207.

[85] M.P. Jahan, M. Rahman, Y.S. Wong, Study on the nano-powder-mixed sinking and milling micro-EDM of WC-Co, Int. J. Adv. Manuf. Technol. 53 (2011) 167–180.

[86] A. Bhattacharya, A. Batish, K. Singh, Fe Simulation and Experimental Validation of Powder Mixed Edm Process for Estimating the Temperature Distribution and Volume Removed in Single Crater, Int. J. Model. Simulation, Sci. Comput. 03 (2012) 1250006 (22 pages).

[87] A. Kumar, S. Maheshwari, C. Sharma, N. Beri, Machining Efficiency Evaluation of Cryogenically Treated Copper Electrode in Additive Mixed EDM, Mater. Manuf. Process. 27 (2012) 1051–1058.

[88] G.S. Prihandana, T. Sriani, M. Mahardika, Improvement of machining time in micro-EDM with workpiece vibration and graphite powder mixed in dielectric fluid, Indian J. Eng. Mater. Sci. 19 (2012) 375–378.

[89] A. Bhattacharya, A. Batish, Predictor Equations for Estimating Crater Dimensions in PMEDM Process Using Fem Simulation and Experimental Validation, Mater. Sci. Forum. 751 (2013) 45–60.

[90] G.S. Prihandana, M. Mahardika, M. Hamdi, Y.S. Wong, N. Miki, K. Mitsui, Study of workpiece vibration in powder-suspended dielectric fluid in micro-EDM processes, Int. J. Precis. Eng. Manuf. 14 (2013) 1817–1822.

[91] X.J. Hu, L.R. Cai, M. Li, W.G. Huo, Experiment and Research of EDM Surface Modification of Titanium in Mist Medium, Appl. Mech. Mater. 538 (2014) 24–27.

[92] A.K. Singh, S. Kumar, V.P. Singh, Optimization of Parameters Using Conductive Powder in Dielectric for EDM of Super Co 605 with Multiple Quality Characteristics, Mater. Manuf. Process. 29 (2014) 267–273.

[93] A.K. Singh, S. Kumar, V.P. Singh, Effect of the addition of conductive powder in dielectric on the surface properties of superalloy Super Co 605 by EDM process, Int. J. Adv. Manuf. Technol. 77 (2014) 99–106.

[94] H. Singh, A. Bhattacharya, A. Batish, Finite element modeling and analysis of powder mixed electric discharge machining process for temperature distribution and volume removal considering multiple craters, Int. J. Model. Simulation, Sci. Comput. 5 (2014) 1450009.

[95] G.S. Prihandana, M. Mahardika, M. Hamdi, Y.S. Wong, K. Mitsui, Effect of micro-powder suspension and ultrasonic vibration of dielectric fluid in micro-EDM processes-Taguchi approach, Int. J. Mach. Tools Manuf. 49 (2009) 1035–1041.

[96] G.S. Prihandana, T. Sriani, K. Prihandana, Y. Prihandana, M. Mahardika, M. Hamdi, et al., Study on the Effect of Nano and Micro MoS2 Powder in Micro-Electrical Discharge Machining, Adv. Mater. Res. 264-265 (2011) 1450–1455.

[97] G.S. Prihandana, T. Sriani, M. Mahardika, M. Hamdi, N. Miki, Y.S. Wong, et al., Application of powder suspended in dielectric fluid for fine finish micro-EDM of Inconel 718, Int. J. Adv. Manuf. Technol. 75 (2014) 599–613.

[98] R.K. Garg, K. Ojha, Parametric optimization of PMEDM process with Nickel Micro Powder suspended dielectric and varying triangular shapes electrodes on EN-19 steel, J. Eng. Appl. Sci. 6 (2011) 152–156.

[99] K. Ojha, R.K. Garg, K.K. Singh, The effect of nickel micro powder suspended dielectric on EDM performance measures of EN-19 steel, J. Eng. Appl. Sci. 6 (2011) 27–37.

[100] K. Ojha, R.K. Garg, K.K. Singh, An investigation into the effect of nickel micro powder suspended dielectric and varying triangular shape electrodes on EDM performance measures of EN-19 steel, Int. J. Mechatronics Manuf. Syst. 5 (2012).

[101] N. Mohri, N. Saito, M. Higashi, N. Kinoshita, A New Process of Finish Machining on Free Surface by EDM Methods, CIRP Ann. - Manuf. Technol. 40 (1991) 207–210.

[102] P. Pecas, E. Henriques, Influence of silicon powder-mixed dielectric on conventional electrical discharge machining, Int. J. Mach. Tools Manuf. 43 (2003) 1465–1471.

[103] H.K. Kansal, S. Singh, P. Kumar, Parametric optimization of powder mixed electrical discharge machining by response surface methodology, J. Mater. Process. Technol. 169 (2005) 427–436.

[104] H. Wang, P. Zhao, Z. Lu, Y. Wang, Z. Qian, Influences of powder on the surface of workpiece in powder-mixed EDM, Zhongguo Jixie Gongcheng/China Mech. Eng. 16 (2005) 618–622.

[105] F.L. Zhao, Y.G. Wang, H. Wang, Application of Artificial Neural Networks Coupled with an Orthogonal Design to Simulation for Powder Mixed EDM, in: 1st Int. Symp. Syst. Control Aerosp. Astronaut., 2005: pp. 1122–1125.

[106] H.K. Kansal, S. Singh, P. Kumar, Performance parameters optimization (multi-characteristics) of powder mixed electric discharge machining (PMEDM) through Taguchi 's method and utility concept, Indian J. Eng. Mater. Sci. 13 (2006) 209–216.

[107] Y.G. Wang, F.L. Zhao, H. Wang, Experimental study on electrode wear in powder mixed EDM, in: Proc. 9th Int. Symp. Adv. Abras. Technol. ISAAT 2006, 2006: pp. 561–565.

[108] H.K. Kansal, S. Singh, P. Kumar, Effect of silicon powder mixed EDM on machining rate of AISI D2 die steel, J. Manuf. Process. 9 (2007) 13–22.

[109] P. Pecas, E. Henriques, Electrical discharge machining using simple and powder-mixed dielectric: The effect of the electrode area in the surface roughness and topography, J. Mater. Process. Technol. 200 (2008) 250–258.

[110] P. Pecas, E. Henriques, Effect of the powder concentration and dielectric flow in the surface morphology in electrical discharge machining with powder-mixed dielectric (PMD-EDM), Int. J. Adv. Manuf. Technol. 37 (2008) 1120–1132.

[111] Y.G. Wang, F.L. Zhao, Y. Liu, Behaviors of Suspended Powder in Powder Mixed EDM, Key Eng. Mater. 375-376 (2008) 36–41.

[112] D.G. Wang, Simulation of Particles Movement in Powder Mixed EDM, Adv. Mater. Res. 97-101 (2010) 4150–4153.

[113] H. Kumar, J.P. Davim, Role of Powder in the Machining of Al-10%Sicp Metal

Matrix Composites by Powder Mixed Electric Discharge Machining, J. Compos. Mater. 45 (2011) 133–151.

[114] S. Padhee, N. Nayak, S.K. Panda, P.R. Dhal, S.S. Mahapatra, Multi-objective parametric optimization of powder mixed electro-discharge machining using response surface methodology and non-dominated sorting genetic algorithm, Sadhana - Acad. Proc. Eng. Sci. 37 (2012) 223–240.

[115] X. Bai, Q.H. Zhang, T.Y. Yang, J.H. Zhang, Research on material removal rate of powder mixed near dry electrical discharge machining, Int. J. Adv. Manuf. Technol. 68 (2013) 1757–1766.

[116] X. Bai, Q.H. Zhang, J.H. Zhang, D. Kong, T.Y. Yang, Machining efficiency of powder mixed near dry electrical discharge machining based on different material combinations of tool electrode and workpiece electrode, J. Manuf. Process. 15 (2013) 474–482.

[117] Y.C. Lin, B.H. Yan, Y.S. Chang, Machining characteristics of titanium alloy (Ti-6Al-4V) using a combination process of EDM with USM, J. Mater. Process. Technol. 104 (2000) 171–177.

[118] Y.C. Lin, B.H. Yan, F.Y. Huang, Surface modification of Al-Zn-Mg aluminum alloy using the combined process of EDM with USM, J. Mater. Process. Technol. 115 (2001) 359–366.

[119] S.H. Yeo, P.C. Tan, W. Kurnia, Effects of powder additives suspended in dielectric on crater characteristics for micro electrical discharge machining, J. Micromechanics Microengineering. 17 (2007) N91–N98.

[120] M.Y. Ali, N.A.B.A. Rahman, E.B.M. Aris, Powder Mixed Micro Electro Discharge Milling of Titanium Alloy: Investigation of Material Removal Rate, Adv. Mater. Res. 383-390 (2011) 1759–1763.

[121] M.Y. Ali, N. Atiqah, Erniyati, Silicon carbide powder mixed micro electro discharge milling of titanium alloy, Int. J. Mech. Mater. Eng. 6 (2011) 338–342.

[122] M.Y. Ali, E.Y.T. Adesta, N.A.B.A. Rahman, E.B.M. Aris, Powder Mixed Micro Electro Discharge Milling of Titanium Alloy: Analysis of Surface Roughness, Adv. Mater. Res. 341-342 (2011) 142–146.

[123] P.C. Tan, S.H. Yeo, Investigation of recast layers generated by a powder-mixed dielectric micro electrical discharge machining process, Proc. Inst. Mech. Eng. Part B J. Eng. Manuf. 225 (2011) 1051–1062.

[124] M.S. Rizi, G.R. Razavi, M. Ostadmohamadi, A.R. Havaie, Optimization Electro Discharge Machining of Ti-6Al-4V Alloy with Silicon Carbide Powder Mixed, Adv. Mater. Res. 566 (2012) 466–469.

[125] H. Yasar, B. Ekmekci, Ti-6Al-4V Surfaces in SiC Powder Mixed Electrical Discharge Machining, Adv. Mater. Res. 856 (2013) 226–230.

[126] Y. Zhang, G. Sun, A. Zhang, Effect of mixed powder ultrasonic vibration on surface structure and mechanical properties of Ti-6Al-4V in Electro-Discharge Machining, Xiyou Jinshu Cailiao Yu Gongcheng/Rare Met. Mater. Eng. 43 (2014) 189–193.

[127] K. Furutani, A. Saneto, H. Takezawa, N. Mohri, H. Miyake, Accretion of titanium carbide by electrical discharge machining with powder suspended in working fluid, Precis. Eng. 25 (2001) 138–144.

[128] K. Furutani, H. Sato, M. Suzuki, Influence of electrical conditions on performance

of electrical discharge machining with powder suspended in working oil for titanium carbide deposition process, Int. J. Adv. Manuf. Technol. 40 (2009) 1093–1101.

[129] P. Janmanee, A. Muttamara, Surface modification of tungsten carbide by electrical discharge coating (EDC) using a titanium powder suspension, Appl. Surf. Sci. 258 (2012) 7255–7265.

[130] S.L. Chen, M.H. Lin, G.X. Huang, C.C. Wang, Research of the recast layer on implant surface modified by micro-current electrical discharge machining using deionized water mixed with titanium powder as dielectric solvent, Appl. Surf. Sci. 311 (2014) 47–53.

[131] H. Zhang, F.Q. Hu, W.S. Zhao, H.J. Hu, Powder mixed EDM of a special material curved surface, Harbin Gongye Daxue Xuebao/Journal Harbin Inst. Technol. 39 (2007) 1076–1079.

[132] S. Kumar, U. Batra, Surface modification of die steel materials by EDM method using tungsten powder-mixed dielectric, J. Manuf. Process. 14 (2012) 35–40.

[133] B. Singh, J. Kumar, S. Kumar, Experimental Investigation on Surface Characteristics in Powder-Mixed Electrodischarge Machining of AA6061/10%SiC Composite, Mater. Manuf. Process. 29 (2014) 287–297.

[134] B. Singh, J. Kumar, S. Kumar, Influences of Process Parameters on MRR Improvement in Simple and Powder-Mixed EDM of AA6061/10 % SiC Composite, Mater. Manuf. Process. 30 (2015) 303–312.

[135] K.L. Wu, B.H. Yan, J.W. Lee, C.G. Ding, Study on the characteristics of electrical discharge machining using dielectric with surfactant, J. Mater. Process. Technol. 209 (2009) 3783–3789.

[136] Y. Zhang, Y. Liu, Y. Shen, R. Ji, Z. Li, C. Zheng, Investigation on the influence of the dielectrics on the material removal characteristics of EDM, J. Mater. Process. Technol. 214 (2014) 1052–1061.

[137] Y. Liu, R. Ji, Y. Zhang, H. Zhang, Investigation of emulsion for die sinking EDM, Int. J. Adv. Manuf. Technol. 47 (2010) 403–409.

[138] Y.F. Chen, Y.C. Lin, Surface modifications of Al-Zn-Mg alloy using combined EDM with ultrasonic machining and addition of TiC particles into the dielectric, J. Mater. Process. Technol. 209 (2009) 4343–4350.

[139] Z.M. Zain, M.B. Ndaliman, A.A. Khan, M.Y. Ali, Improving micro-hardness of stainless steel through powder-mixed electrical discharge machining, Proc. Inst. Mech. Eng. Part C J. Mech. Eng. Sci. 228 (2014) 3374–3380.

[140] H. Wang, F.L. Zhao, Y.G. Wang, Z.Z. Lu, Study of overcut in powder mixed EDM, Dalian Ligong Daxue Xuebao/Journal Dalian Univ. Technol. 48 (2008) 63–67.

[141] Z.M. Zain, M.B. Ndaliman, A.A. Khan, M.Y. Ali, Electro-Discharge Machining of SUS 304 Stainless Steel with TaC Powder-Mixed Dielectric, Adv. Mater. Res. 576 (2012) 72–75.

[142] M.Z. Zahiruddin, E.A. Rahim, S. Hasan, L.N. Alvin, Effect of electrical parameters on the PMD-EDM performances of titanium alloy, in: ICPMT2006 - Prog. Mach. Technol. - Proc. 8th Int. Conf. Prog. Mach. Technol., 2006: pp. 245–248.

[143] J.L. Wang, H. Yang, M. Li, Study on Discharge Parameters of Surface Strengthening with Powder Mixed Near Dry EDM for H13 Steel, Appl. Mech. Mater. 602-605 (2014) 757–760.

[144] B.H. Yan, H.C. Tsai, F.Y. Huang, The effect in EDM of a dielectric of a urea solution in water on modifying the surface of titanium, Int. J. Mach. Tools Manuf. 45 (2005) 194–200.

[145] S. Kumar, R. Singh, Investigating surface properties of OHNS die steel after electrical discharge machining with manganese powder mixed in the dielectric, Int. J. Adv. Manuf. Technol. 50 (2010) 625–633.

[146] F. Klocke, S. Kamenzky, M. Schwade, Investigations on the influence of powder suspended dielectrics in μ-Wire-EDM, in: Proc. 10th Int. Conf. Eur. Soc. Precis. Eng. Nanotechnology, EUSPEN 2010, 2010: pp. 335–338.

[147] F. Klocke, J. Dieckmann, M. Garzón, Micro electro discharge machining (μ-EDM) with additivated dielectrics, in: Proc. 10th Int. Conf. Eur. Soc. Precis. Eng. Nanotechnology, EUSPEN 2010, 2010: pp. 351–354.

[148] K. Furutani, Y. Shimizu, Experimental analysis of deposition process of lubricant surface by electrical dis- charge machining with molybdenum disulfide powder suspended in working oil, in: Proc. 18th Annu. Meet Am. Soc. Precison Eng., Portland, OR, USA, 2003: pp. 547–550.

[149] S. Tripathy, D.K. Tripathy, Multi-attribute optimization of machining process parameters in powder mixed electro-discharge machining using TOPSIS and grey relational analysis, Eng. Sci. Technol. an Int. J. (2015). doi:10.1016/j.jestch.2015.07.010.

[150] P.C. Tan, S.H. Yeo, Simulation of Surface Integrity for Nanopowder-Mixed Dielectric in Micro Electrical Discharge Machining, Metall. Mater. Trans. B. 44 (2013) 711–721.

[151] U.K. Vishwakarma, A. Dvivedi, P. Kumar, Finite element modeling of material removal rate in powder mixed electric discharge machining of Al-SiC metal matrix composites, in: TMS Annu. Meet., 2013: pp. 151–158.

[152] U.K. Vishwakarma, A. Dvivedi, P. Kumar, Comparative study of powder mixed EDM and rotary tool EDM performance during machining of Al-SiC metal matrix composites, Int. J. Mach. Mach. Mater. 16 (2014) 113.

[153] Q. Gao, Experimental Study of Powder-mixed Near Dry Electrical Discharge Machining, J. Mech. Eng. 45 (2009) 169–175.

[154] Q. Gao, Q. Zhang, J. Zhang, X. Ai, Powder mixed near dry electrical discharge machining, in: 16th Int. Symp. Electromachining, ISEM 2010, 2010: pp. 79–83.

[155] Specail metals - INCONEL alloy 625, (n.d.). http://www.specialmetals.com/assets/documents/alloys/inconel/inconel-alloy-625.pdf.

[156] D.C. Montgomery, Design and Analysis of Experiments, Wiley, New York, 2001.

[157] M.K. Pradhan, Experimental investigation and modelling of surface integrity, accuracy and productivity aspects in edm of AISI D2 steel, 2010.

[158] M.K. Pradhan, Determination of optimal parameters with multi response characteristics of EDM by response surface methodology, grey relational analysis and principal component analysis, Int. J. Manuf. Technol. Manag. 26 (2012) 56–80.

[159] J. Xu, G.P. Sheng, H.W. Luo, F. Fang, W.W. Li, R.J. Zeng, et al., Evaluating the influence of process parameters on soluble microbial products formation using response surface methodology coupled with grey relational analysis., Water Res. 45

(2011) 674–680.

[160] G.K. Williamson, W.H. Hall, X-ray line broadening from filed aluminium and wolfram, Acta Metall. 1 (1953) 22.

[161] D.D. DiBitonto, P.T. Eubank, M.R. Patel, M.A. Barrufet, Theoretical models of the electrical discharge machining process. I. A simple cathode erosion model, J. Appl. Phys. 66 (1989) 4095.

[162] A. Erden, Effect of Materials on the Mechanism of Electric Discharge Machining (E.D.M.), J. Eng. Mater. Technol. 105 (1983) 132–138.

[163] P. Shankar, V.K. Jain, T. Sundararajan, Analysis of Spark Profiles During Edm Process, Mach. Sci. Technol. 1 (1997) 195–217. doi:10.1080/10940349708945647.

[164] M.R. Patel, M.A. Barrufet, P.T. Eubank, D.D. DiBitonto, Theoretical models of the electrical discharge machining process. II. The anode erosion model, J. Appl. Phys. 66 (1989) 4104.

[165] Y. Du, H. Chen, R. Chen, N. Xu, Synthesis of p-aminophenol from p-nitrophenol over nano-sized nickel catalysts, Appl. Catal. A Gen. 277 (2004) 259–264.

[166] G.I. Titelman, V. Gelman, S. Bron, R.L. Khalfin, Y. Cohen, H. Bianco-Peled, Characteristics and microstructure of aqueous colloidal dispersions of graphite oxide, Carbon N. Y. 43 (2005) 641–649.

[167] B. Ekmekci, Y. Ersöz, How Suspended Particles Affect Surface Morphology in Powder Mixed Electrical Discharge Machining (PMEDM), Metall. Mater. Trans. B. 43 (2012) 1138–1148.

[168] M.A. Arafin, M. Medraj, D.P. Turner, P. Bocher, Transient liquid phase bonding of Inconel 718 and Inconel 625 with BNi-2: Modeling and experimental investigations, Mater. Sci. Eng. A. 447 (2007) 125–133.

[169] A. Kumar, V. Shankara, T. Jayakumar, K.B.S. Rao, B. Raj, Correlation of microstructure and mechanical properties with ultrasonic velocity in the Ni-based superalloy Inconel 625, Philos. Mag. A. 82 (2002) 2529–2545.

[170] F. Xu, Y. Lv, Y. Liu, F. Shu, P. He, B. Xu, Microstructural Evolution and Mechanical Properties of Inconel 625 Alloy during Pulsed Plasma Arc Deposition Process, J. Mater. Sci. Technol. 29 (2013) 480–488.

[171] A. Mohanty, G. Talla, S. Gangopadhyay, Experimental Investigation and Analysis of EDM Characteristics of Inconel 825, Mater. Manuf. Process. 29 (2014) 540–549.

[172] H. Ramasawmy, L. Blunt, K.P. Rajurkar, Investigation of the relationship between the white layer thickness and 3D surface texture parameters in the die sinking EDM process, Precis. Eng. 29 (2005) 479–490.

[173] G.D. Smith, S.J. Patel, The Role of Niobium in Wrought Precipitation-Hardened Nickel-Base Alloys, Superalloys 718, 625, 706 Var. Deriv. (2005) 135–154.

[174] M. Shakil, M. Ahmad, N.H. Tariq, B.A. Hasan, J.I. Akhter, E. Ahmed, et al., Microstructure and hardness studies of electron beam welded Inconel 625 and stainless steel 304L, Vacuum. 110 (2014) 121–126.

[175] B. Bhattacharyya, S. Gangopadhyay, B.R. Sarkar, Modelling and analysis of EDMed job surface integrity, J. Mater. Process. Technol. 189 (2007) 169–177.

[176] M.A.E.R. Merdan, R.D. Arnell, The surface integrity of a die steel after electrodischarge machining: 2 residual stress distribution, Surf. Eng. 7 (1991) 154–158.

Dissemination

[1] G. Talla, S. Gangopadhyay, C.K. Biswas, Effect of Powder-Suspended Dielectric on the EDM Characteristics of Inconel 625, *Journal of Materials Engineering and Performance*, 2016, vol. 25(2), pp. 704-717

[2] G. Talla, S Gangopadhyay, C.K. Biswas, State of the art in powder mixed electric discharge machining: A review, *Proceedings of the Institution of Mechanical Engineers, Part B: Journal of Engineering Manufacture*, (Accepted 2016), doi: 10.1177/0954405416634265

[3] G. Talla, S. Gangopadhyay, C.K. Biswas, Influence of graphite powder mixed EDM on the surface integrity characteristics of Inconel 625, *Particulate Science and Technology: An International Journal*, (Accepted 2016), doi: 10.1080/02726351.2016.1150371